Nanofluidic Device for Active Variation of Confinement Using Pneumatically Actuated Flexible Nanoscale Membranes

Xavier Capaldi

A thesis submitted to McGill University in partial fulfillment of the requirements of the degree of **Master of Science**

Department of Physics
McGill University
Canada, Québec
2018-08-14

Contents

Abstract

A pneumatically-actuated membrane device is designed and fabricated to dynamically confine multiple DNA chains into nanoscale pit features. A nanoscale nitride membrane is used as a lid that deflects under pneumatic pressure. With this device single λ-DNA and plasmid DNA are studied in a confined environment. In addition systems are studied containing two λ-DNA chains or a single λ-DNA with a plasmid. The interactions of multiple confined macromolecules were quantified, which is relevant in the study of biological systems in which multiple DNA molecules are highly confined by cell walls and other organelles. This confinement is found to greatly impact the polymer dynamics and molecule conformation. In addition preliminary work has been done to extend the device to map unstained molecules trapped under a membrane in fluorescent buffer.

Abrégé

On a conçu et fabriqué un dispositif membranaire à actionnement pneumatique afin de confiner plusieurs chaines d'ADN en alvéoles nanométriques. Une membrane nanométrique fabriquée de nitrure sert de couvercle capable de dévier sous pression pneumatique. Ce couvercle membranaire facilite l'étude d'ADN Phage λ unique et d'ADN plasmidique unique dans un environnement confiné. En outre, on étudie des systèmes de deux ADN-λ et d'ADN-λ avec ADN-plasmidique. On quantifie les interactions de macromolécules multiples confinées, dont le confinement s'avère pertinent dans l'étude de systèmes biologiques dans lesquels l'ADN multiple est confiné par des parois cellulaires ou d'autres organites. On trouve que ce confinement exerce un impact considérable à la dynamique et à la conformation d'un polymère. On a entamé également des travaux préliminaires pour que le dispositif puisse cartographier des molécules non marquées qui seront désormais piégées sous la membrane placée au-dessus de la solution tampon fluorescente.

Acknowledgements

I am deeply grateful to my supervisor, Professor Walter Reisner, who has advised and supported me throughout my program. He has been a source of inspiration and motivation. I have learned a great deal from his genuine and direct approach to advising and he has pushed me to become a better scientist every day. In addition, he spent a great deal of time helping me to edit the content of my thesis.

I would also like to thank Professors Michael Hilke, Rob Sladek and Rodrigo Reyes-Lamothe who have advised me on matters both academic and research-related.

I would be remiss if I did not acknowledge Zezhou Liu who has been my research partner since our earliest days. We have worked in parallel for countless hours. His expertise with instrumentation has been invaluable. I am proud to share a co-authorship with him given our close collaboration over the past two years.

Lili Zeng introduced me to the methods necessary to analyze our data computationally. She has proven very insightful and always brings up valuable points when discussing our work.

Yuning Zhang is an incredible resource in our research group. His knowledge of fabrication and experimentation is extensive. I would have doubled my time in the microfab if it were not for his insight and experience.

I am also grateful for the students and postdocs who advised and helped me before their departure from McGill. Whether through direct contribution or discussions, they have assisted in the culmination of my project. I have used their design templates and read their theses. Without their guidance, I would have struggled greatly. I must thank Ahmed Khorshid, Susan Amin, Carlos Ruiz-Vargas, Martin Lee, Philip Zimny and Yue Qi.

I would also like to thank the staffs of the McGill Nanotools Microfab (MNM) and l'Institut National de la Recherche Scientifique (INRS) Énergie Matériaux Télécommunications Research

Centre (EMT) Micro and Nanofabrication Laboratory (LMN). In particular, Zhao Lu, Sasa Ristic, John Li, Peng Yang and Alireza Hajhosseini Mesgar at MNM and Boris LeDrogoff, Amine Zitouni and Fabien Dauzou at INRS-EMT-LNF. They have all contributed to my skills and knowledge in the cleanroom for which I am deeply grateful. In addition Robert Gagnon, Pascal Bourseguin and Jean-Philippe Guay, in the physics department, have been incredible resources and always willing to help.

My three close friends have been my support system in Montréal. Harrisonn Griffin, Aude Bechu and Tormund brightened my days and made this exerience so much more fun.

My family has also always been there as my bulwark. I have survived many days on the food they send from home and enjoyed the weekends I got to recouperate on the farm. I must give special thanks to my father for helping with the translation of my abstract.

I cannot thank my partner, Florainne, enough. During my roughest moments in the program, she always found a way to reassure and encourage me. She has always made an effort to understand my work and to suggest ways to improve how I go about my efforts in graduate school.

Statement of Originality and Contribution

This thesis represents the culmination of work I have done over the past two years throughout my M.Sc. It has led to the submission of a paper for publication as a co-author with my lab partner, Zezhou Liu. The paper is currently in review in the journal *Soft Matter*. Several new projects embarked using the technology developed in this time.

With input from our lab mates, Zezhou and I fabricated the experimental devices. I spent a great deal of time troubleshooting the fabrication process and ultimately solved the issue causing device failure. In particular, Yuning Zhang, was extremely helpful for this process as he is very experienced in fabrication techniques. I designed and prepared the mounting chuck while Zezhou programmed the controller for applying pneumatic pressure. We ran experiments together. I programmed the ImageJ image processing program for data pre-processing. Lili Zeng wrote the first iteration of our analysis code which Zezhou subsequently modified further. Figures throughout the paper were created by Zezhou and myself. The entire project was under the supervision and mentorship of my supervisor, Walter Reisner. Professor Rodrigo Reyes-Lamothe provided insight during the writing process into the biologically interesting aspects of our experiments.

The distinct contributions to scientific knowledge are: (1) development of a pneumatically-actuated nanofluidic device which can vary the confinement environment dynamically, (2) measurement and quantification of the interactions of multiple DNA chains in a confined environment and (3) exploratory work in a novel imaging technique to map surface features and macromolecules.

Chapter 1

Introduction

Polymer behavior is altered in a confinement environment. In particular the dynamic and equilibrium properties of a polymer will be influenced when the chain is confined below its free solution radius of gyration. This fact can be applied to the study of DNA, a biological polymer of great scientific interest. A nanochannel, effectively a 1-dimensional confinement environment, can be used to extend DNA linearly for high-throughput mapping [42, 43, 37]. This is the principle underlying nanoconfined DNA barcode mapping in which base pair sequences of interest are nicked, differentially stained and elongated in a nanochannel device for imaging [47]. Nanopores, nanoscale holes in a thin membrane, are the basis for a purely electrical sensing technique. The trans-pore current can be measured as a DNA chain translocates the pore. The presence of the molecule in the pore transiently increases the pore resistance, leading to a dip in current or 'blockade.' Emphasis in this thesis will be on 'transverse' nanofluidic structures such as nanoslits (2D), nanochannels (1D) and nanocavities (0D).

Nanoscale pit features can be embedded in a nanoslit to create local changes in entropy. This results in a free energy landscape for trapping and manipulating single chains [28]. DNA can be stretched across two or more adjacent nanopits with part of the contour confined to the feature and part stretched between features in the nanoslit. An analysis of trapped chains can reveal the difference in confinement free energy between the nanocavities and the nanoslit [28]. In addition nanochannels can be embedded in nanoslits. The confinement environment still induces DNA trapping and extension but the nanoslit provides access for buffer exchange [41]. These hybrid nanoslit environments with embedded features are an important model to understand single-molecule transport in free energy landscapes [39, 53, 11, 26].

In a static confinement environment like the nanoslit with embedded nanocavity, loading the polymer can prove challenging as they must overcome the initial free energy barrier to enter the nanoslit. In addition, only single-chain confinement can be explored as it is challenging to confine two polymers to a single feature when there is an open slit nanotopography. Active confinement technologies, such as 'Convex-lens Induced Confinement' or the 'Dimple Machine' can dynamically vary the confinement environment by adjusting the nanoslit spacing above the substrate [7, 49]. In addition, these techniques can actively drive polymers into the trapping features. Most notably, with this active loading, multiple molecules can be confined in the same cavity, allowing a study of their interaction in such highly confined environments.

We have developed a new active confinement technology that improves upon the prior-developed

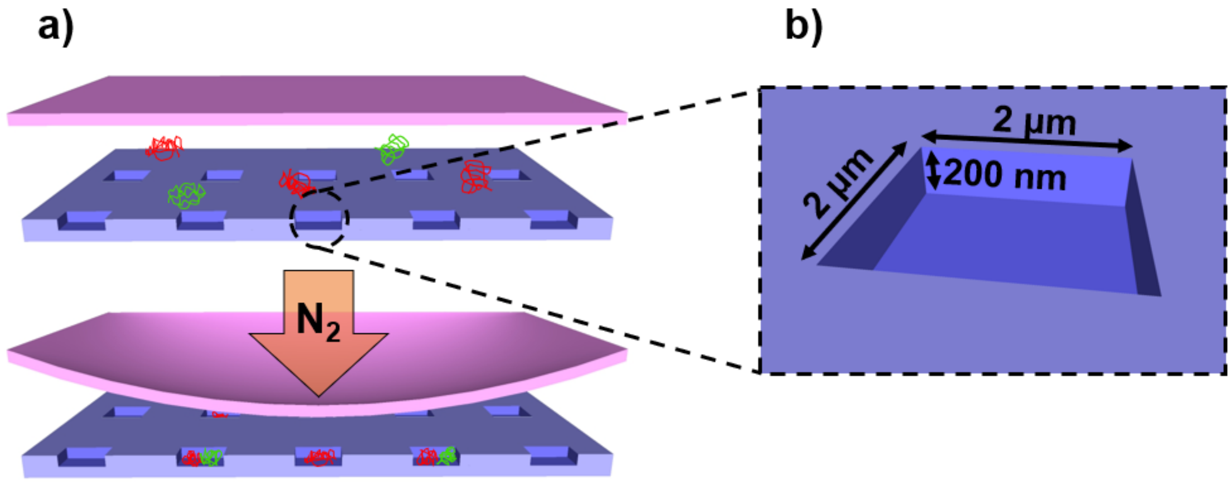

Figure 1.1: Schematic demonstrating operation of pneumatically actuated molecule trapping device. The red and green molecules represent differentially-stained λ-DNA which are initially unconfined in the channel environment. (b) Upon the application of nitrogen pressure, to deflect the membrane lid downwards, the molecules are trapped inside the embedded features.

methods. The device contains nanocavity structures embedded in a nanoslit. Pneumatic pressure is applied to a 50 nm thick silicon nitride membrane, forcing the membrane to deflect downwards into the nanoslit (figure 1.1). This top-loading approach does not require the use of a dedicated piezoactuated lens pusher, such as the ‘Convex-lens Induced Confinement’ approach which will be reviewed in section 2.3, and is more suitable for large-scale multiplexing. It is somewhat similar to the ‘Dimple Machine’ (section 2.2) but is based on direct-bonded, hard materials instead of PDMS, and uses standard nanochannel fabrication techniques. In addition, this technology can be integrated with nanopores and may be able to achieve full channel sealing by varying the fabrication parameters. Such a device can support a variety of trapping features and be expanded as a full lab-on-a-chip platform.

We work primarily with isolated and purified DNA molecules and we are very comfortable with their behavior in an unconfined, bulk environment. In biological systems however, DNA molecules are never found alone. They are always confined by other cellular organelles, structural elements of the cell and the cell wall itself. In the case of bacterial replication, the Mbp scale circular genome is simultaneously undergoing replication. Bacterial chromosomes have protein binding agents which are orders of magnitude smaller than the genome itself, yet help to keep it condensed into large domains. Before dividing, the genomes must segregate in the tight cellular environment. The virus, which can be even smaller, is simply a protein shell protecting highly confined DNA which will be injected into its target. E. coli, for example is predated on by a virus known as E. coli lambda bacteriophage. As mentioned, the E. coli genome is highly confined and bound by protein stuctures inside the prokaryotic cell. When the bacteriophage injects a linear strand of λ-DNA (which later ligates to form a large circular plasmid), this invasive genetic sequence is interacting in a highly confined environment; and yet, takes over the cellular functioning, turning E. coli into a lysogen housing many new viral capsids. In eukaryotic cells, the DNA is still organized by proteins but has a nuclear membrane as well. Throughout these systems, an understanding of polymer organization and dynamics in highly confined environments is vital to understanding basic biological principles such as cellular replication and viral infection.

A related but distinct question is the degree to which small molecules can penetrate larger polymer coils in confined systems. Many bacteria, including E. coli, carry plasmids. Plasmids are small circular DNA molecules that carry useful ancillary genes and these plasmids must also be segregated during bacterial division [40]. Recent studies suggest that plasmids may not be distributed randomly through the bacteria [44, 55], and in particular may be excluded from certain regions around the chromosome and instead concentrate at the cell poles. There is little understanding of this mechanism but quantitative experimental studies on polymer organization in confined volumes may reveal the conditions in which polymer molecules of varying size exclude each other or mutually penetrate.

In an effort to test the efficacy of our device and also begin to explore multichain confinement, we introduce two populations of DNA molecules to the nanoslit. One population is labeled with the uniform stain YOYO-1 (491/509 nm) and the other with YOYO-3(612/631 nm). The molecules are present at a high concentration to increase the probability of trapping two differentially stained molecules in a single cavity after membrane deflection. By design of our cavities, when a single chain is trapped, the chain is confined vertically but only weakly confined laterally, leading to a slightly increased gyration radius and reduced diffusion (relative to both bulk and pure slit confinement). However, when actively confining *two chains*, the lateral confinement is no longer weak and we find the conformation and dynamics of the molecules are very strongly altered due to their interaction. Specifically, identical chains with a coil size on the order of the cavity width (48.5 kbp

λ-DNA, confined in 2 µm wide, 200 nm deep cavities) undergo spatial segregation and have altered conformation due to the second chain. Dynamically, the chains undergo Brownian rotation about the cavity center and have drastically altered diffusional relaxation times. This degree of confinement with two chains is impossible in bulk or open nanofluidic systems like nanoslits and nanochannels. Only a cavity system can enforce long-time interaction of two polymers in a constricted environment and only an active confinement device is capable of trapping two polymers into this cavity. We also explore the behaviour of a small plasmid molecule trapped with a larger coil (6.9 kbp plasmid with λ-DNA in 2 µm wide, 200 nm deep cavities). While the plasmid can diffuse across the λ-DNA coil, the plasmid leads to weaker but still observable interaction effects on the organization of the λ-DNA.

In this thesis, first, the actuated/active confinement technologies developed in the past will be reviewed, beginning with valves produced with multilayer soft lithography in 2000 and ending with the CLiC active confinement technology in 2010. Following this, the fabrication methodology for our new device approach will be covered thoroughly, especially detailing the challenges faced when producing suspended nanoscale membranes. The experimental setup and process will be detailed. Preliminary results on a novel imaging technique will also be presented. The results of two-molecule confined mixing experiments will be shown. Plans for future experiments and research questions will finalize the document.

Chapter 2

Review of Previous Approaches for Actively Varying Device Confinement

Micro/nanofluidic actuation and active confinement technologies originated in 2000 with multilayer soft lithography. In the subsequent ten years, these technologies evolved in an effort to produce devices both robust and capable of controlled nanoscale confinement. The progression of active confinement technologies between 2000 and the present will be reviewed, beginning with valves developed using multilayer soft lithography techniques. Then hybrid devices, those combining soft lithography and nanolithography, will be explored. Finally, a top-down, active confinement technology (CLiC), developed ten years after the original valves, will be reviewed. Our modern, enclosed device, is produced using fabrication techniques for nanochannel devices and overcomes some of the limitations of those technologies developed prior. It is the first robust, solid-material device which relies on pneumatic actuation of a nanoscale lid to actively confine molecules. Our device draws inspiration from the soft, conforming lid used by Adam Cohen's group but instead uses top-down actuation like the CLiC technology. The benefits of this design will be detailed in section 3.1.

2.1 Multilayer Soft Lithography

2.1.1 Principle of Operation

The group of Stephen Quake used two poly(dimethyl)siloxane (PDMS) channels to create the first pneumatically actuated valves [52]. PDMS is flexible so increasing the pressure in one channel will cause it to bulge into the second, sealing it off. Figure 2.1 details the simple two-step mold and bond process to produce this type of device. These will be referred to as Quake Valves.

These simple valves are powerful tools for experiments involving microfluidics. They can be used to seal channels or isolate regions of a device. By incorporating several valves, microfluidic pumps and mixing chambers can be produced. These components can be combined to make integrated platforms capable performing complex experiments within a single device.

2.1.2 Fabrication

PDMS is a silicone material, widely used for microfluidic devices because it is particularly easy to mold and bond compared to the fabrication techniques based on hard materials (detailed in section

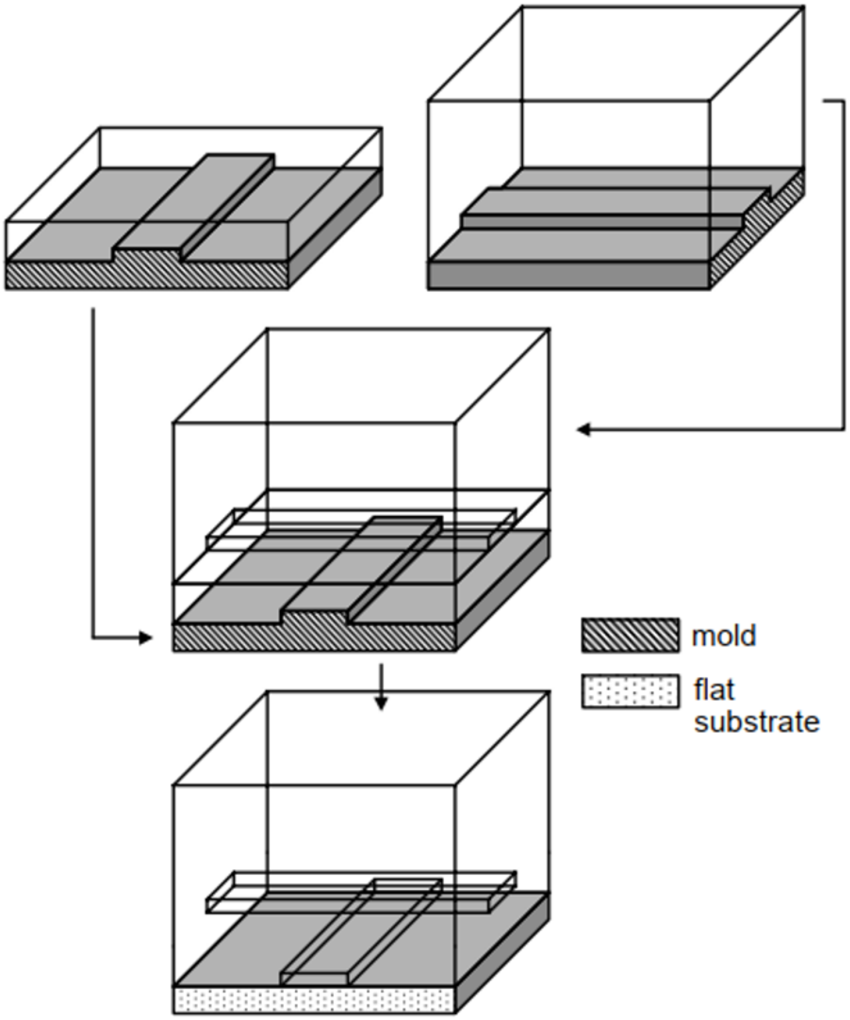

Figure 2.1: Fabrication process for classic quake valve based on multi layer soft-lithography. Two distinct PDMS channels are produced with two master molds. The molds are patterned photoresist on silicon wafers. After curing seperately, the two layers are bonded together to a glass substrate. Figure courtesy of [52].

3.1). Typically a master mold is etched in silicon or made using standard lithographic processes and thick photoresist. The PDMS is mixed with a crosslinking agent and degassed before being poured or spun over a mold. The mixture is degassed again to ensure there are no bubbles in the final structure. After curing, the PDMS can be removed from the mold easily as it has a soft rubber-like texture and is flexible. PDMS will form a contact bond with most clean surfaces. If a more permanent bond is required, it can be activated with oxygen plasma [21]. PDMS is porous which is both a positive and negative trait. This allows gasses to diffuse through the feature, providing fresh oxygen for live cells. However the device quickly becomes contaminated and this is especially problematic when working with fluorescent molecules which can stick and build up on the porous walls. In addition smaller fluidic features can dry due to evaporation through the PDMS.

If a standard lithographic process is performed to produce the master mold, the PDMS features will be square with vertical sidewalls. This geometry is unfavorable for full channel sealing because the actuated layer cannot conform to the sharp corners of the channel. To combat this, a photoresist master mold is fabricated and then baked at a high temperature to reflow the resist, creating curved features. The PDMS can conform to the gradual decline in the sidewall, making the devices easier to seal.

Isolation Region Quake valves can seal off regions of a microfluidic device. In figure 2.2 cyanobacterial cells are shown contained in a region by two quake valves. These cells are very small (1-2 µm) and reproduce slowly so long experiments are necessary. In a traditional microfluidic device they will drift due to buffer flow. In this setup, they can be contained for long period of time with no drift [57].

Mixing Chamber These valve structures were combined to produce devices with other capabilities than simple sealing. In particular, by combining several valves with a circular channel a rotary pump can be produced. This structure can be seen in figure 2.3. By alternating the actuation of each valve in the correct sequence, buffer can be pumped around the circular channel.

The rotary pumps are used as mixing chambers in microfluidic devices where lamillar flow dominates [17]. In particular, valves and pumps can be combined and multiplexed to lyse and purify genomic DNA in parallel [25]. One such device can be seen in figure 2.4. With 26 access ports, 1 waste port and 54 valves, the device is capable of running three lysis and purification

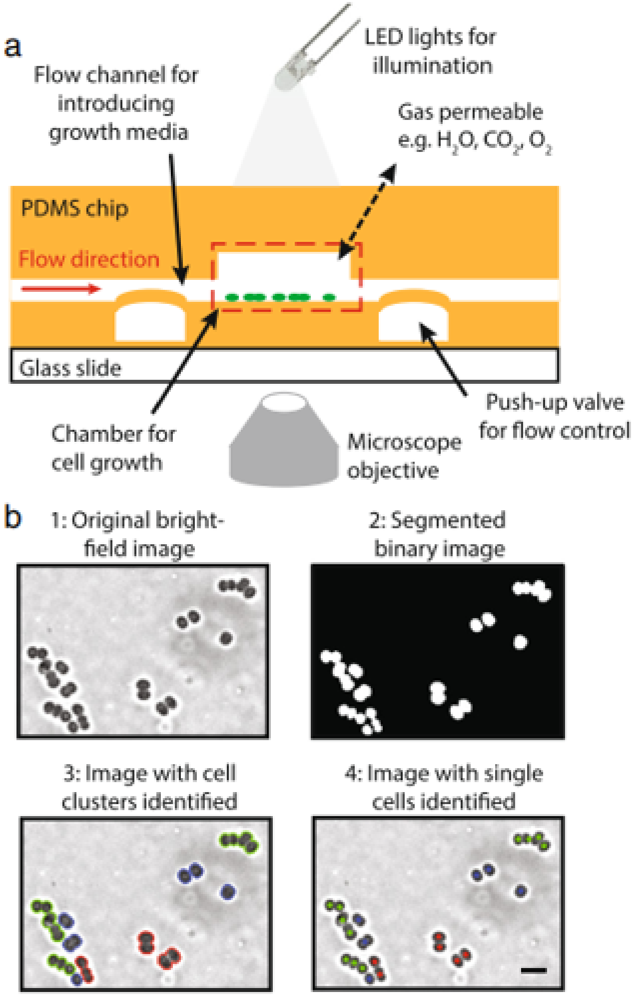

Figure 2.2: Microfluidic bacterial culture device. (a) Schematic of the cell culture chip which incorporates two quake valves to control buffer flow. (b) 1: Original image, 2: binary image, 3: cell cluster image, 4: single cell image. Figure courtesy of [57].

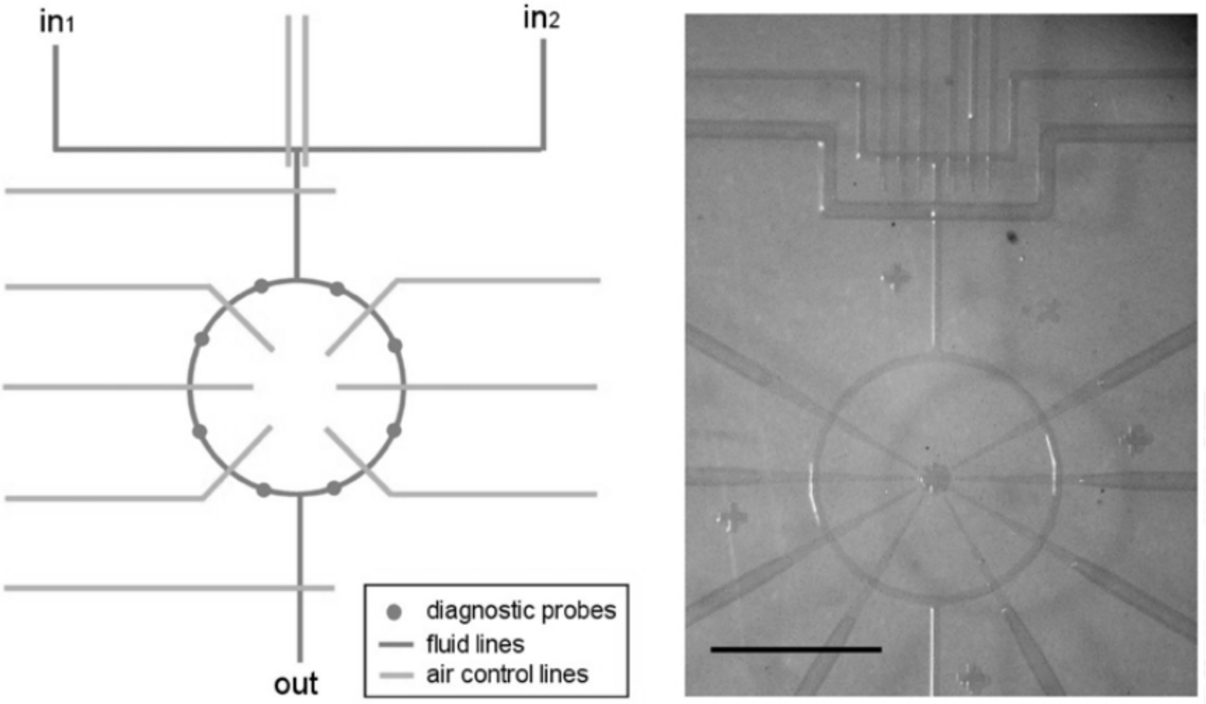

(a) (b)

Figure 2.3: (a) Schematic of rotary pump utilizing several Quake Valves in series around a circular microchannel. (b) Functional rotary pump fabricated in PDMS. Fluidic channels and valves are 100 µm wide and 10 µm deep. Figure courtesy of [17]

processes at once. The entire device is only 2 by 2 cm [25].

2.1.3 Three-layer Soft Lithography

Until 2012, most PDMS valves were limited to a minumum dimension of 100 µm. This was primarily due to the thickness of the PDMS being actuated pneumatically. The standard monolithic fabrication method consisted of only two PDMS layers, both of which were spun on a master mold. This forced the minimum feature to be larger than the mold features. To decrease the valve size, a three layer device was fabricated. A schematic can be seen in figure 2.5(a). The microchannel and inlet layers are fabricated as usual. However a very thin layer of PDMS (<1 µm) is prepared and sandwiched between the two thicker layers. This thin membrane is capable of deflecting and conforming to much smaller features as can be seen in figure 2.5(b). This improved process is capable of sealing 6 µm channels which vastly improved the multiplexing capabilites of these devices [2].

2.1.4 3D Printing

The most recent innovations with these devices have been centered around facilitating their fabrication process even further. Stereolithographic 3D printing is used to produce devices similar to the classic Quake Valve. The technique faces some serious limitations however. First, the printing resin (PEG-DA-258) is not as flexible as PDMS, so the microchannel was modified to incorporate a raised cup (figure 2.6(d-f)). This reduced the distance necessary for the actuating membrane to travel [31]. However this does block most of the flow in the microchannel and creates a deadspace around the actuation point. Also the resolution limit of 3D printing made their most shallow features 40 µm in depth.

2.1.5 Limitations

PDMS microfluidics and the classic Quake Valves were great technological innovations when they were developed. However, they have key limitations. The smallest channels successfully sealed are 6 µm, too large for any study of nanoscale confinement. In addition, PDMS itself is hard to use in fluorescence studies since the fluorophores accumulate in the material. The material also dries during experiments, either requiring a modification to the device or a limitation on the length of an

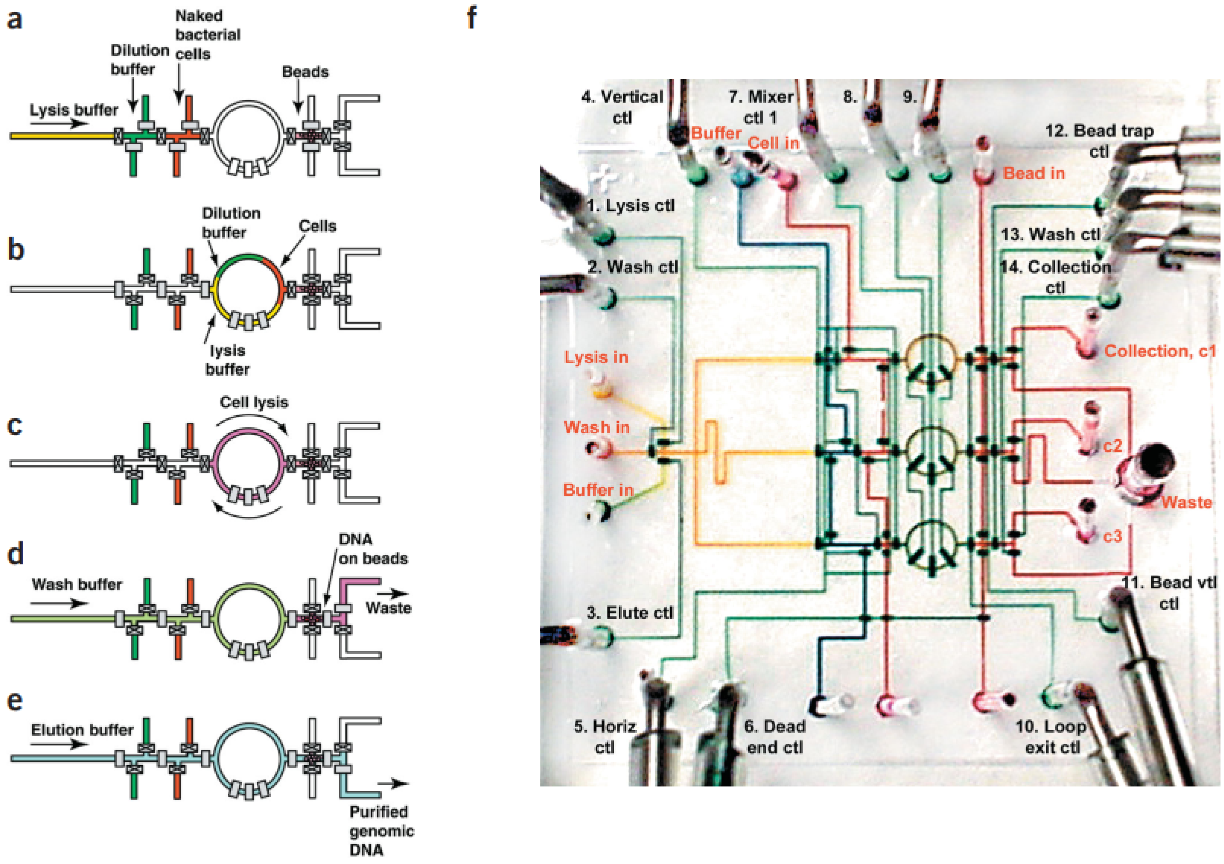

Figure 2.4: (a-e) Schematic of DNA isolation process in PDMS microfluidic device with buffer control and rotary pump operated with quake valves. (f) Functional chip designed for isolation of DNA from bacterial cells. Channels with different functions are colored for clarity. Device is designed to perform three parallel processes and contains 26 access ports, 1 waste port and 54 valves. This is all contained within 2 by 2 cm. The fluidic channels are 100 µm and the actuation channels are twice that. Figure courtesy of [25].

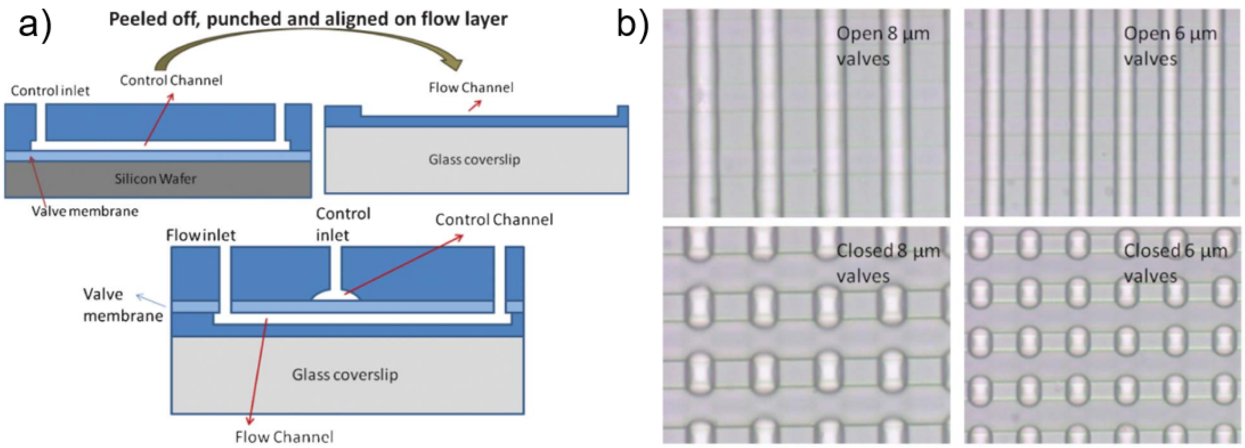

Figure 2.5: Three-layer fabrication method for small channel sealing. (a) Schematic of three-layer fabrication method. Thin valve membrane and the control layer are produced using the standard silicon master mold before being bonded. The separate flow layer is made and bonded to a glass coverslip. Finally the membrane and control channel stack is bonded to the flow channel layer. (b) Test devices with arrays of 6 and 8 µm valves. They are shown in both open and closed states. Figure courtesy of [2].

experiment. Between this and the accumulation of fluorophores, the devices always have a limited lifetime before they are too contaminated to run further experiments.

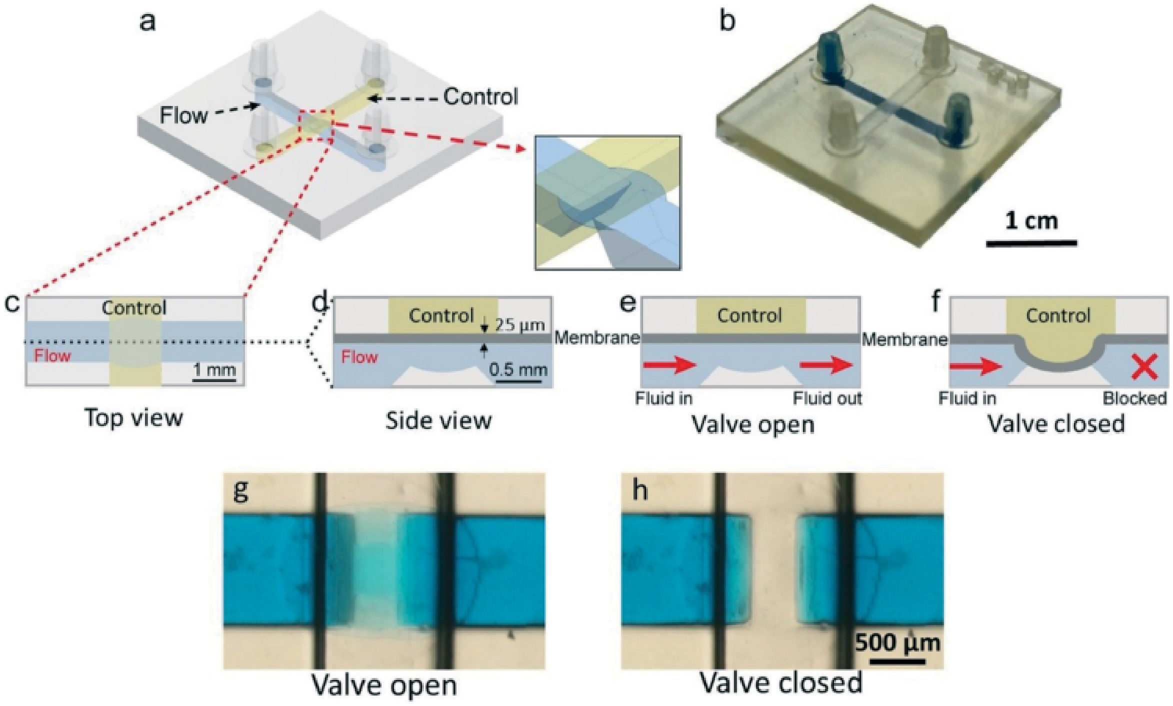

Figure 2.6: 3D printed valves inspired by quake valve geometry. (a) Schematic of test device. (b) Test device printed with stereolithography. (c) Cross-sectional top view of schematic showing the actuation region. (d) Cross-section side view of schematic showing the actuation region and the unique channel geometry. (e) Buffer flow in the channel while valve is open. (f) Buffer flow arrested by sealed valve. (g) Image of experimental device while valve is open and buffer can be seen flowing. (h) Image of exerimental device while valve is being actuated. Buffer is clearly blocked from flowing. Figure courtesy of [31].

2.2 Dimple Machine

2.2.1 Principle of Operation

The Dimple Machine utilizes a three-layer PDMS fabrication method which improved on the Quake approach. It overcomes some of the limitations on feature size by using standard lithographic techniques to produce small features in a hard substrate. It also used the actuating layer to seal molecules of interest into features, rather than just as a valve in a microfluidic system. The glass substrate contains nanoscale 'dimples' patterned by electron beam lithography. The PDMS lid consists of three layers: a channel spacer, the actual lid with nipple structures and a large block with a reservoir for buffer (figure 2.7). The device is operated by loading buffer containing analyte into the microchannel. Vacuum is applied to the loading ports which pulls the PDMS lid down. The nipples contact the nanoscale dimple array, sealing molecules of interest inside (figure 2.7(b)) [49].

2.2.2 Fabrication

The fabrication process is detailed in figure 2.8 [49]. An e-beam process is used to produce nanoscale trapping features on the fused silica substrate to which the PDMS will be bonded (2.8(a)). The PDMS lids themselves are produced using a normal molding process as can be seen in 2.8(b). They are then bonded together to the glass substrate. Because this device only uses PDMS as the actuated lid, the actual trapping features are much smaller than in previous devices.

2.2.3 Performance

Figure 2.9 shows the Forster resonance energy transfer (FRET) imaging of DNA trapped in the dimple array. The device trapping rate was characterized to be quite high showing repeated trapping over many iterations [49]. The authors noted, however, that they struggled with their dimples drying; the volume of liquid is so small and PDMS is porous. Solution is added to a reservoir above the actuation membrane to ensure there is no gas directly above the dimples. This is referred to as the deoxygenation chamber in figure 2.7. In addition, there can only ever be one actuation point since the device relies on applying vacuum at both loading ports.

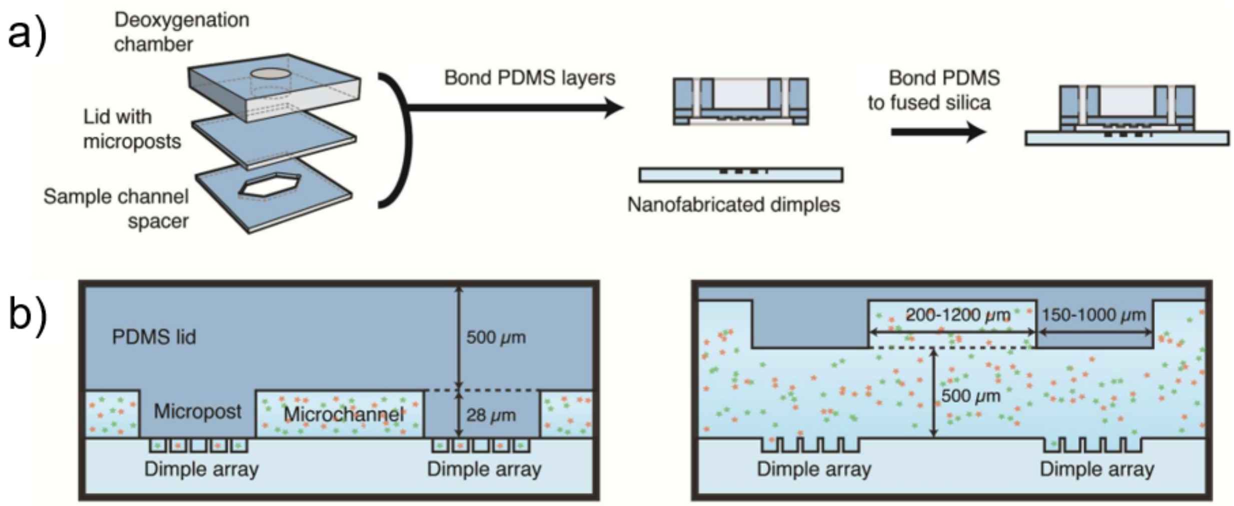

Figure 2.7: (a) Prior to operation three PDMS layers are bonded to a fused silica substrate. Each serves a distinct purpose. The bottom layer is simply a spacer to accomodate the buffer. The second layer is the actuation lid which contains nipples that will seal the dimple arrays. Finally the top layer is thick for structural stability and contains an open reservoir for liquid to avoid the dimples drying. (b) Buffer containing analyte is loaded into the microchannel. When vacuum is applied to the loading ports, the PDMS nipples are pulled down, sealing the nanoscale dimples and trapping molecules of interest. Figure courtesy of [49].

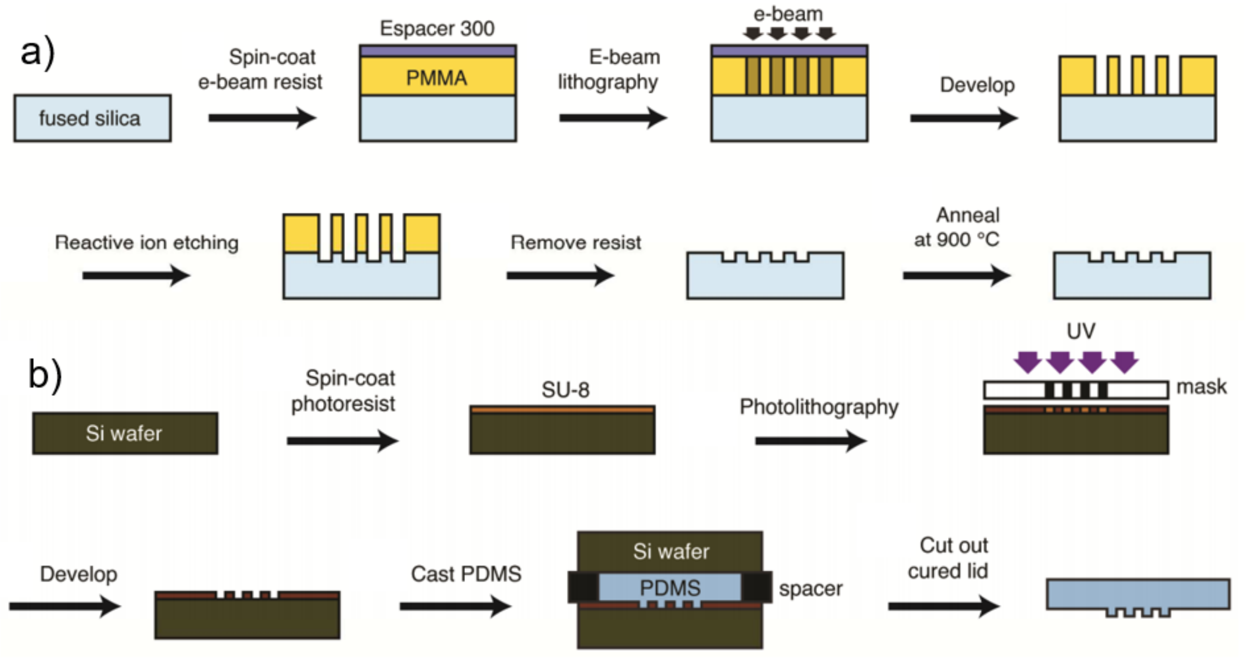

Figure 2.8: Simplified schematic of fabrication process to produce the Dimple Machine. There are two materials that used to produce separate components: (a) Fused silica substrate with nanoscale trapping features (dimples). (b) Three PDMS components which make up microchannels, nipples to seal features on fused silica wafer and deoxygenation chamber. Figure courtesy of [49].

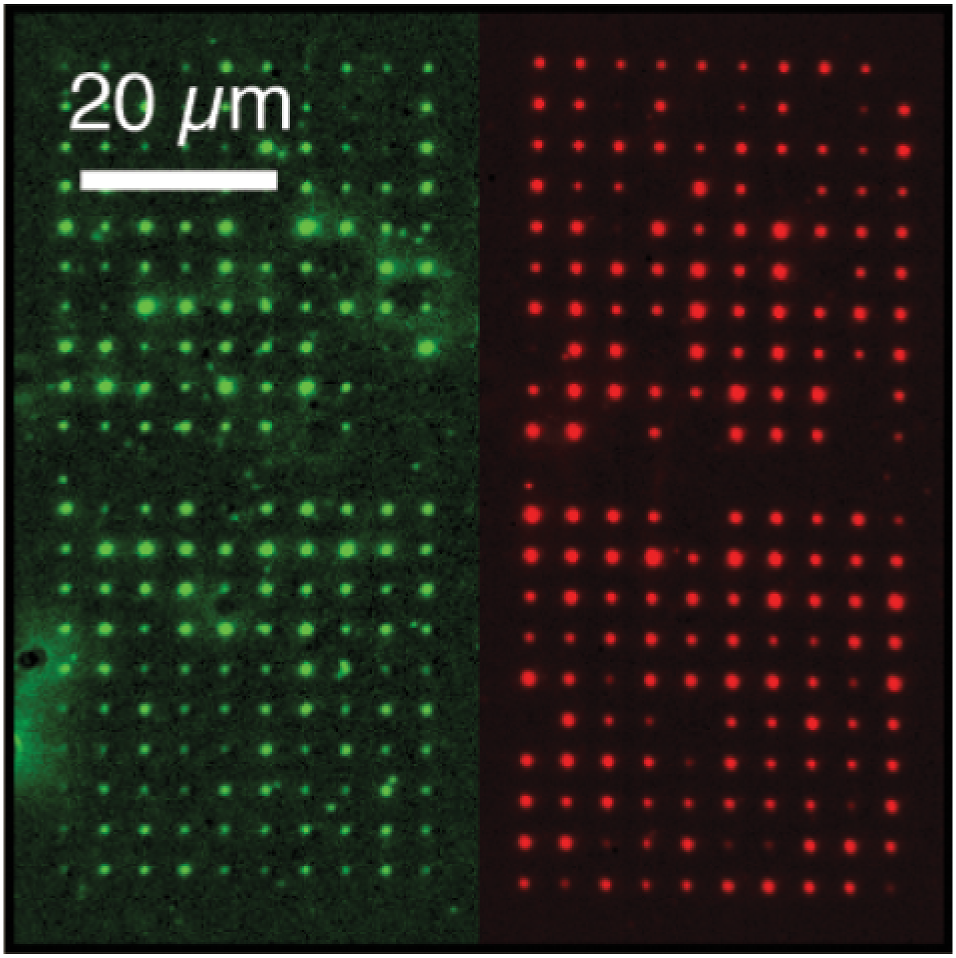

Figure 2.9: Forster resonance energy transfer (FRET) imaging of DNA trapped in the dimple array. Green represents donor fluorescence and red, acceptor fluorescence. Image was acquired with a dual-view CCD. Figure courtesy of [49].

2.3 Convex Lens Induced Confinement

2.3.1 Principle of Operation

The CLiC methodology is distinct from the previous two technologies. CLiC has a top-loading actuation mechanism, similar to the dimple machine, but relies on mechanically pressing a coverglass lid with a specialized push-lens. In its earliest iteration, the pressing was performed manually with an xyz translational stage [32]. The microfluidic device is simple; usually no more than a flow cell and some features etched in fused silica (figure 2.10). The experimental methodology is very similar to that of the Dimple Machine. Buffer containing analyte is loaded into the channel. The coverglass is depressed by the push-lens, trapping molecules in features etched in the substrate below. As can be seen in figure 2.11 the device is capable of trapping and extended λ-DNA in linear and circular nanochannels [7].

2.3.2 Fabrication

As with the dimple machine, a glass substrate is etched to produce trapping features (figure 2.10). A spacer which is typically double-sided adhesive tape creates the loading channel. Instead of a PDMS lid, coverglass is used. This lid cannot be actuated pneumatically so the entire chip is mounted in a specialized setup that can be seen in figure 2.12.

2.3.3 Lens Control

The xyz translational stage for controlling the push-lens is not precise enough for good experimental measurements. Instead the setup was upgraded with a piezo actuator. The push-lens is brought to the surface manually but the piezo controls the extension of a push-lens when it directly contacts the coverglass lid [7, 32, 9, 36]. The setup also uses an interferometer to measure the gap height (figure 2.12). This allows precise control of the confinement environment.

2.3.4 Multistage Trapping

Figure 2.13 shows the details of a device which can isolate, trap and lyse a cell using CLiC [36]. The push-lens can then be raised and move to new location to trap and extend the purified DNA. This

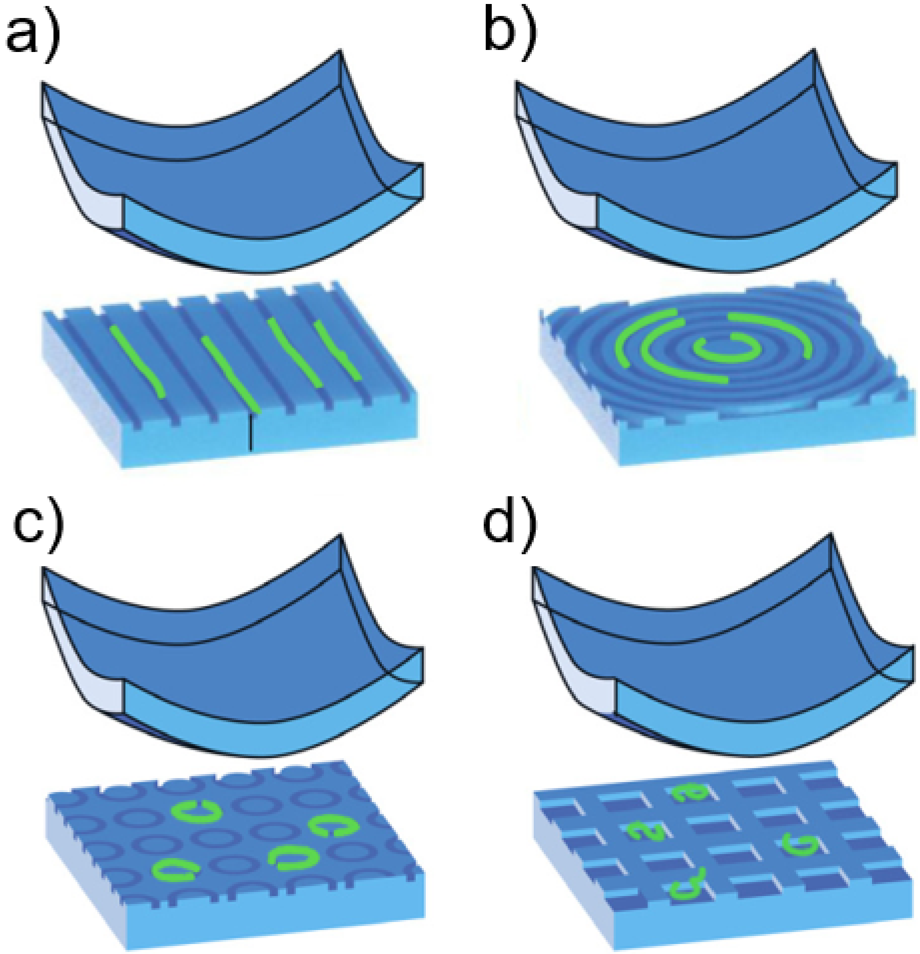

Figure 2.10: Principle of operation of CLiC technology. The push-lens deflects thin coverglass downward, inducing confinement and trapping DNA in (a) nanochannels, (b) concentric circular nanochannels, (c) independent circular nanochannels and (d) nanoscale pits. Figure courtesy of [8].

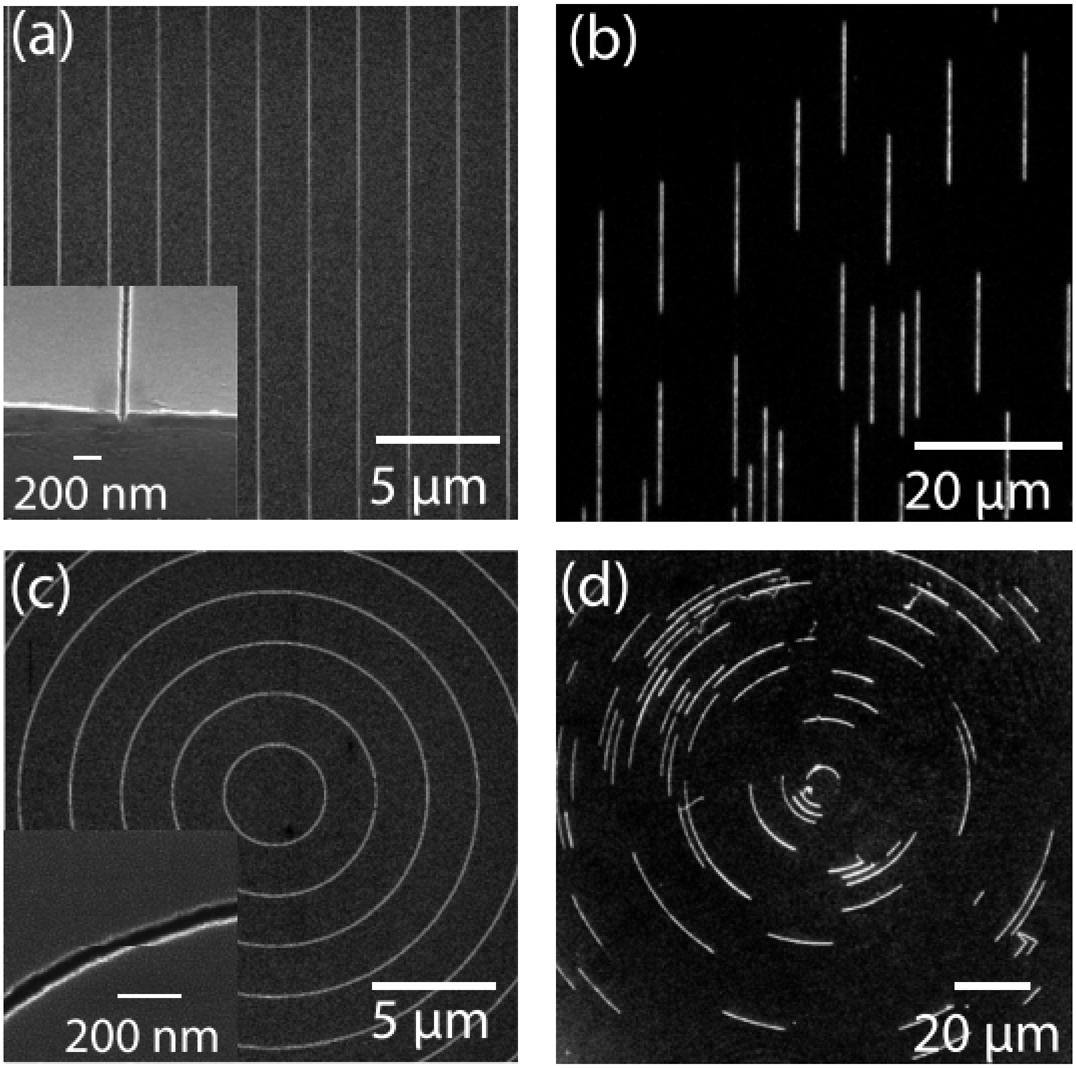

Figure 2.11: DNA confined in concentric circular and linear nanochannels. (a) SEM of linear nanochannels with inset showing a depth of approximately 65 nm and width of approximately 50 nm. (b) λ-DNA compressed into linear nanochannels. (c) SEM of concentric circular nanochannels with inset showing a depth of approximately 65 nm and width of approximately 50 nm. (d) λ-DNA compressed into concentric circular nanochannels by the CLiC lens which is positioned at the center. Figure courtesy of [8].

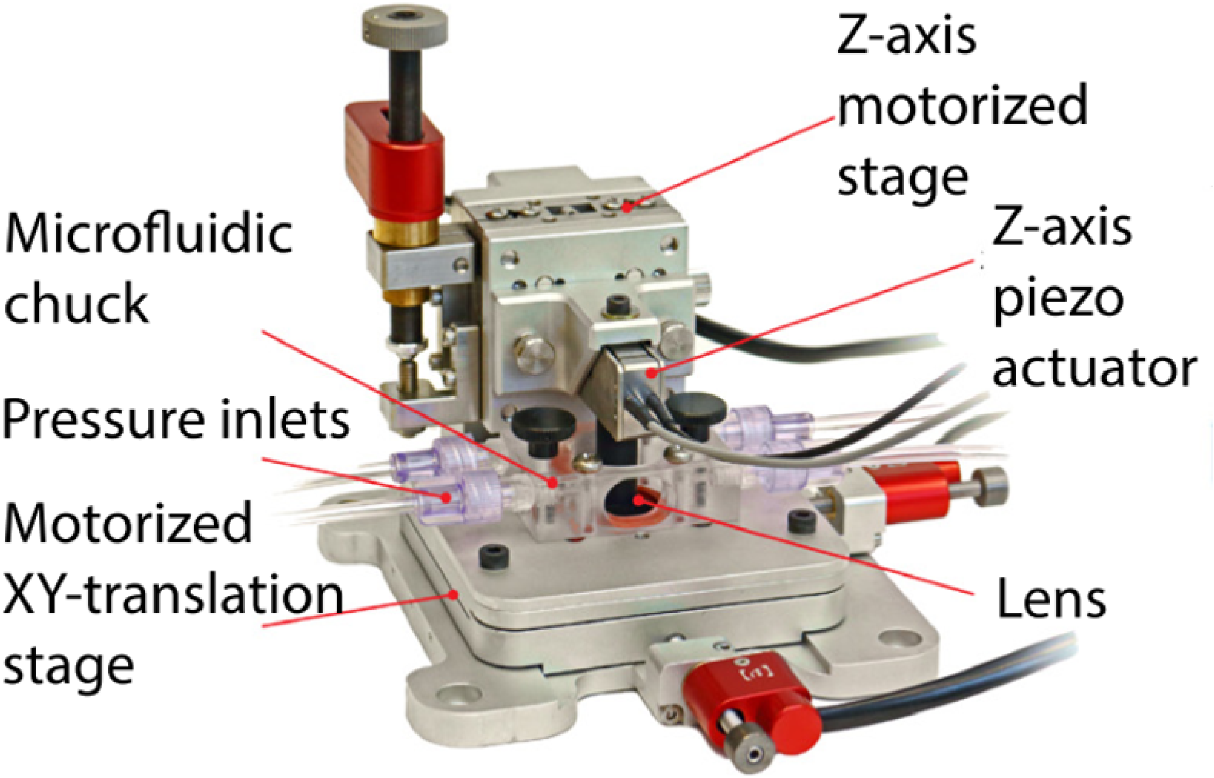

Figure 2.12: Modern CLiC setup which is mounted on an inverted optical microscope. The actual device is mounted in a microfluidic chuck which can be positioned using an zy-translational stage. The CLiC push-lens contacts the top of the device. It can be controlled vertically by a rough motorized stage or by a piezo actuator. Figure courtesy of [8].

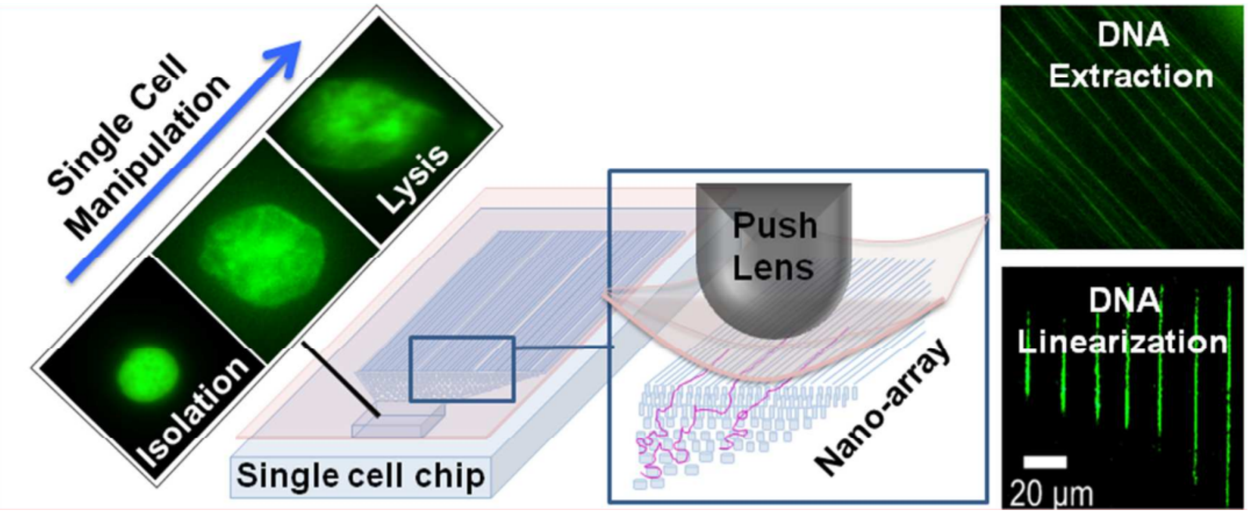

Figure 2.13: A device designed to isolate, trap, and lyse a cell before extracting the DNA and linearizing it in another region. The device is actuated in two distinct regions for lysis and extension. It consists of a chip isolation chamber, a pillar network for DNA isolation and nanochannels for linearization. Figure courtesy of [36].

mobility is an advantage over the Dimple Machine, where the actuation point was fixed. However the scale must be taken into account with this. The push-lens is simply too big to have multiple lens' interfaced with the device at once. This requires the lens to be raised and moved if multiple actuation points are required.

2.3.5 Fixed Height Slit

Despite the piezoelectric control and interferometry setup, for some devices, microfabricated structures are added to create an artificial gap when the lid is fully actuated. Posts spaced 30 μm apart and ranging from 20 to 100 nm tall were etched in the coverglass lid (figure 2.14(c)). A microchannel for buffer exchange was etched in close proximity to an array of nanochannels. As the push-lens descended and the gap spacing approached the persistence length of the chains, they were forced into the nanochannels. Stain was added and diffused from the microchannel, staining the trapped DNA [23]. This staining can be seen in figure 2.15. The purple is Cy5 stain added to the buffer to show the gap is present. The dark regions are the supporting posts.

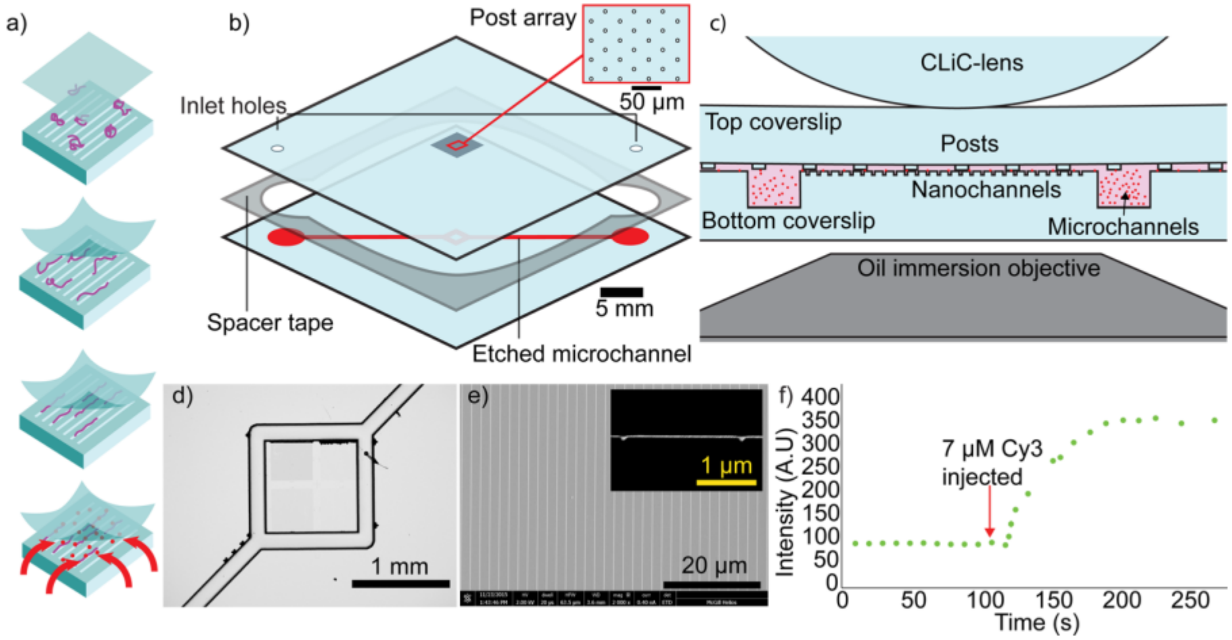

Figure 2.14: Fixed gap device. (a) Schematic of DNA trapping. Lid is actuated by push-lens. When gap height approaches the 50 nm persistence length of DNA, the chains enter the 50 nm channel and extend. Due to the fixed gap, new buffer can be introduced. (b) Exploded schematic of nanofluidic device. The bottom is glass substrate with micro- and nanochannels etched in the surface. The microchannel is positioned close to the nanochannel region. 10 μm double-sided tape is used as a spacer and the lid is another glass substrate with a post array etched to ensure that when fully actuated, there is a 20 to 100 nm gap for buffer exchange. (c) Cross-sectional schematic of device with lid fully actuated. (d) Optical microscopy image of microchannel surrounding nanochannel array. (e) SEM image of nanochannel array with the inset showing the cross-section. (f) Plot of fluorescent intensity in nanochannels. Cy3 fluorescent dye is added to stain DNA trapped in nanochannels. Figure courtesy of [23].

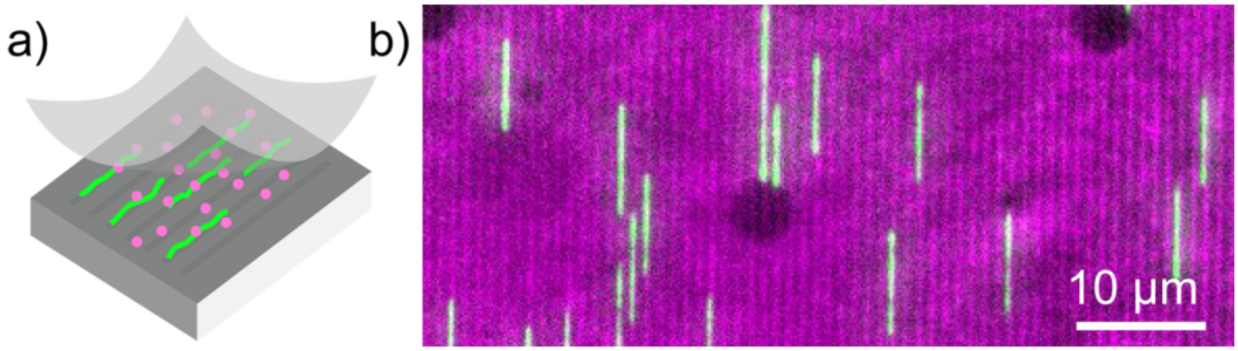

Figure 2.15: (a) Schematic of device with experimental buffer. Stained DNA chains (green) are extended in nanochannels with Cy5 dye (purple) in the surrounding buffer (b) Fluorescent microscopy image of DNA (green) extended in nanochannels and Cy5 stained buffer (purple). Note the dark circles which are the posts that offset the lid from the nanochannels. Figure courtesy of [23].

2.3.6 Electrophoretically-enhanced Trapping

One of the challenges addressed by CLiC is DNA loading into highly confined environments. The Dimple Machine also addressed this when loading DNA into the nanopit arrays. The CLiC technology was taken further. In figure 2.16(b), one can see that DNA does not easily pass from a largely unconfined environment to a nanoslit. The DNA is mostly caught against the interface between the two environements. Active confinement, as shown in figure 2.16(e), already vastly improves the trapping rate as the transition between the two environements is very gradual. However, with the application of an electric field, which induces an electrophoretic force on DNA, the loading efficiency can increase five-fold [1]. The electrophoretic force actively moves DNA toward the confined environment as the trapping lid is actuated (figure 2.16(h)). As can be seen in figure 2.17(c), increasing the voltage improves the trapping efficiency even further.

2.3.7 Limitations

CLiC is a powerful active confinement technique but it has some key drawbacks. As shown in figure 2.12, the technique requires a highly specialized and bulky setup. An xzy translational stage, push-lens and piezoelectric actuator are all required. This makes the technology expensive for other researchers to adopt. The lid is coverglass which is too thick to conform well to surface

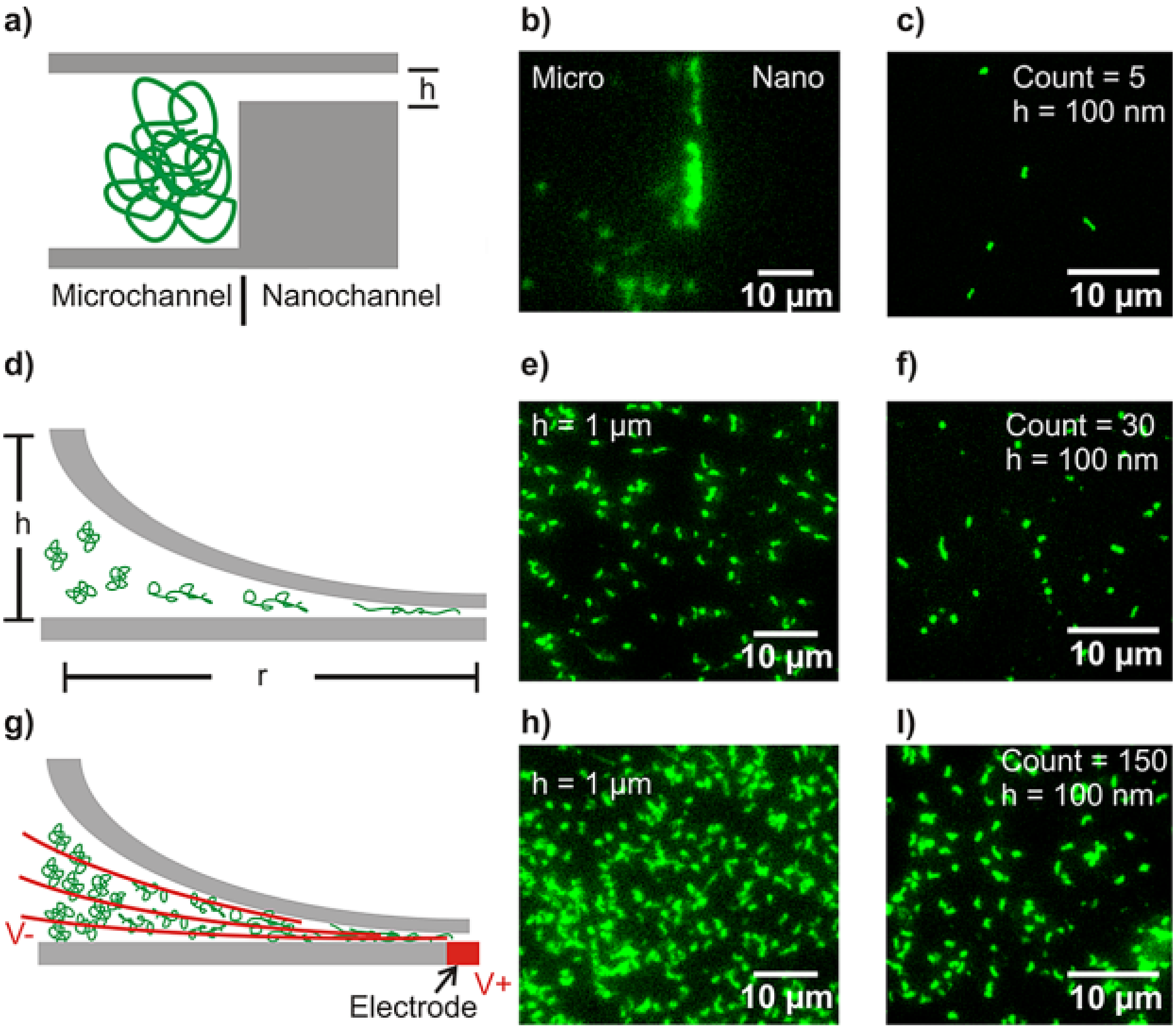

Figure 2.16: Loading DNA in nanoscale features using different techniques. (a) Schematic of DNA at the interface between micro- and nanochannel. (b) Interface of between micro- (1 µm) and nanoslit (100 nm). It is clear the DNA does not pass easily into the nanoslit. (c) DNA chain concentration is low in the nanoslit. (d) Schematic of confinement induced by CLiC technology. (e) DNA are smoothly spread over the gradually increasing confinement environment and (f) loading is greatly improved. (g) Schematic of CLiC induced confinement combined with the electrophoretic force. (h-i) DNA concentration is many times higher than the other loading methods. Figure courtesy of [1].

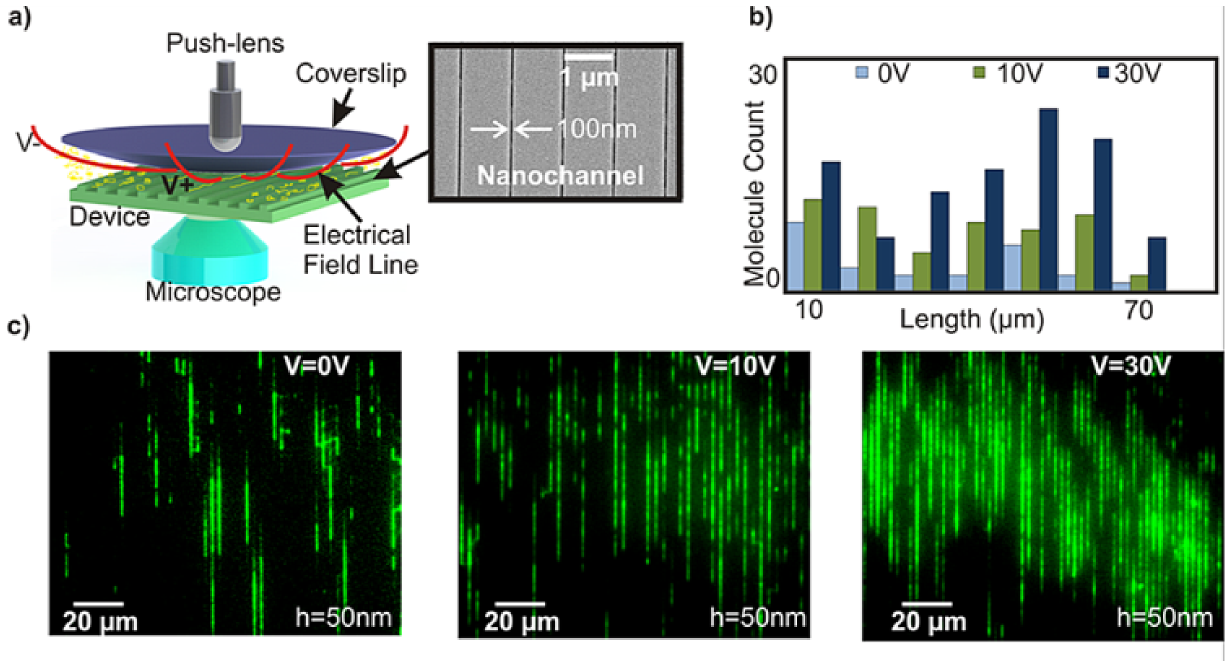

Figure 2.17: (a) Schematic of nanoscale enhanced-capture device. Standard push-lens is used to induce confinement by actuating a coverslip. The device has 100 nm nanochannels (SEM inset) etched in the substrate. The applied electric field improves the trapping rate. (b) Histogram of DNA extension length for varying electric fields. (c) T4 DNA extended in nanochannels. It is clear that increasing voltage improves the trapping rate. Figure courtesy of [1].

features. Buffer will always flow around the trapping zone because their are large open regions at the edge of cell where the coverglass is being deflected. In addition, the gap between substrate and lid is made by tape which does not have a well known height unlike features produced in a cleanroom. The devices must be disassembled between experiments because the tape does not survive in buffer for an extended period of time. Also due to the size of the CLiC setup, only one actuation point is possible in a standard microfluidic device. This removes the possibility of multiplexing or producing complex devices involving multiple trapping sites (without manually repositioning the push-lens).

Chapter 3

Fabrication and Operation of Device with Pneumatically Actuated Nanoscale Membranes

3.1 Device Fabrication

Our pneumatically actuated trapping device is fabricated using lithographic processes standard to the nanofluidics field (e.g. fabrication of nanochannel and nanopore devices). However it incorporates thin (50 nm) nitride membranes. The finished devices, as shown in figure 3.1, consist of a loading channel, trapping features and a depressable membrane lid. When applying nitrogen pressure to the lid, it conforms to the the substrate below and induces confinement in any trapping features. The thin nitride is better able to conform and more robust than PDMS. In addition, because it is actuated from above, it can be multiplexed. However, unlike CLiC, the actuation mechanism is easy to operate and has a small footprint on the whole setup. In the future, this could be expanded further with an interfacial PDMS layer, allowing a dense network of actuation regions across a small device. If the channel etch process is modified to produce a curved surface, the nitride lid can fully seal channels in addition to trapping molecules of interest. This is a natural extension in the capabilities of previous actuation devices, allowing the incorporation of nanoscale trapping features and nanopores in the thin membrane. In addition, it is the first device of its nature that is entirely self-contained and made of solid materials. It does not share the challenges of PDMS and does not rely on a temporary tape spacer. It expands the applicability of the technology and makes it more economically viable for lab-on-a-chip experiments.

Fabricating these membrane features is nontrivial. In particular, the anodic bonding process (section 3.1.5) seals the enclosed channel under vacuum. In the subsequent membrane release step (section 3.1.6), the membranes deflect and break, introducing a viscous residue and rendering the devices inoperable. A variety of potential solutions were explored (sections 3.1.5 and 3.1.6) before an acceptable protocol was developed. The devices can now be fabricated with a good yield and the resulting product is robust and reusable.

A simplified depiction of the fabrication process can be seen in figures 3.2 and 3.3. Photoresist is spun on a cleaned borosilicate substrate. Microchannels are exposed by UV photolithography and developed. The channels are etched with reactive ion etching. The substrate is then cleaned thoroughly. E-beam resist is spun on the surface followed by a chromium deposition. The trapping features are exposed with e-beam lithography. The chromium is etched before developing the resist. The trapping features are etched with reactive ion etching as well. The substrate is cleaned thoroughly before being anodically bonded to a double-side polished silicon wafer with a 50 nm

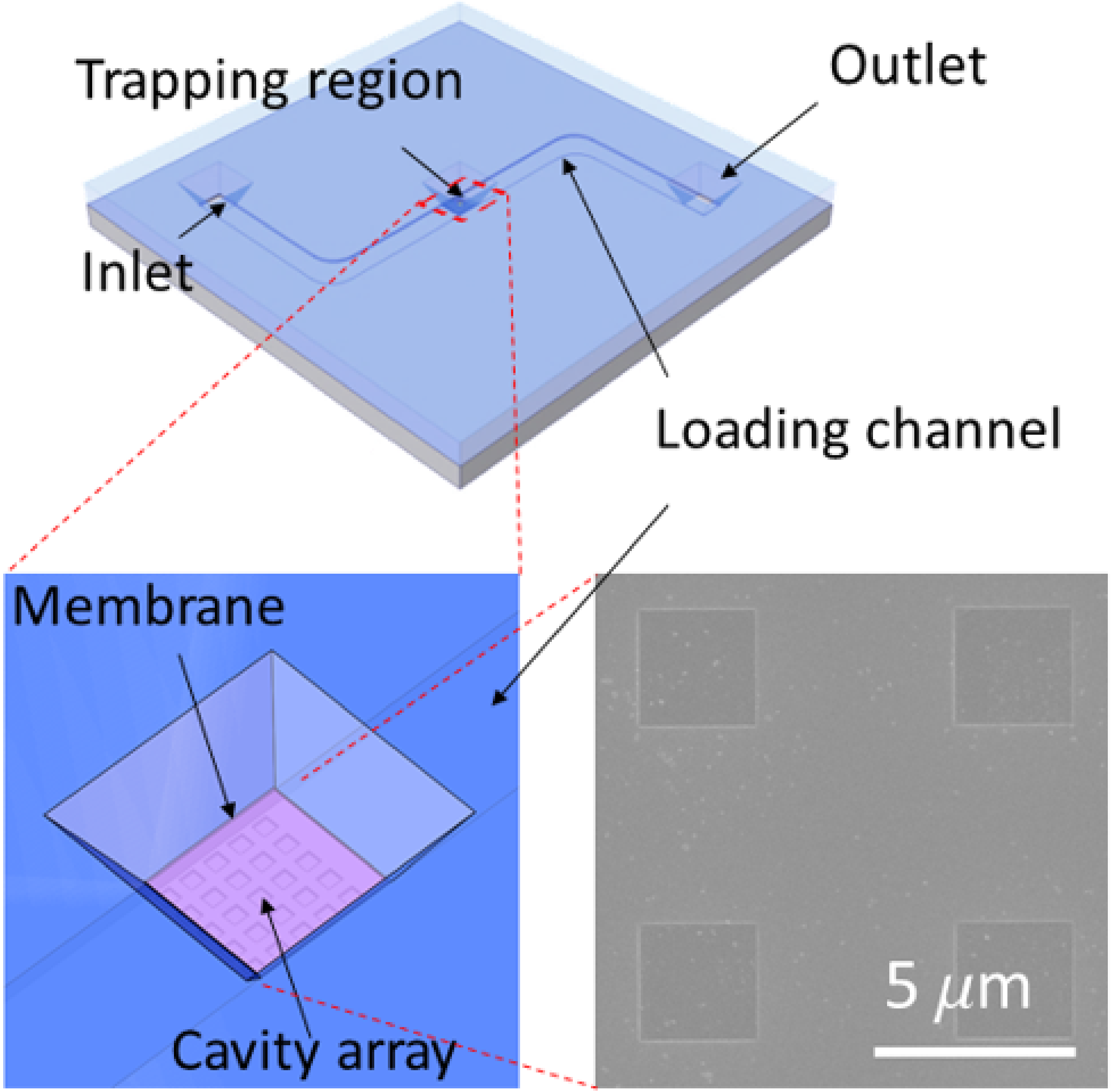

Figure 3.1: Design of the fluidic chip for active pneumatic loading. (a) The trapping region is located at the center of chip, interfaced to a thin nitride membrane (drawn semi-transparent in purple so that cavities underneath can be viewed). An SEM image shows the cavity features etched in the borosilicate glass. Note that this SEM was taken *through* the 50 nm membrane following device bonding.

nitride layer. Photoresist is spun on the exposed nitride surface and access windows are exposed with UV photolithography. After development, the nitride windows are etched, leaving exposed silicon. The wafer is cleaned again. Finally the exposed silicon is etched with a potassium hydroxide solution, leaving suspended membranes over the loading reservoirs and the trapping region. Specialized release steps to avoid membrane failure and residue formation are detailed in sections 3.1.5 and 3.1.6.

3.1.1 Substrate

The starting substrate is a is 200 µm borosilicate glass wafer (Schott BOROFLOAT® 33 with the following composition: 81% SiO_2, 13% B_2O_3, 4% Na_2O/K_2O and 2% Al_2O_3). The glass is produced using the float production process wherein the molten material is floated on a bath of liquid tin before being annealed. This gives a smooth surface finish [13]. While the material was originally designed as a cheap alternative to fused silica, boasting a low coefficient of thermal expansion, high transparency, chemical resistance and good mechanical strength [14], it is used for this fabrication process due to its ion composition which is vital for anodic bonding (described in section 3.1.5). An alternative to BOROFLOAT® 33 is Corning Pyrex® 7740 which has a similar composition and properties.

The second wafer is a 400 µm double-side polished silicon wafer with 50 nm silicon nitride deposited by low-pressure chemical vapor deposition (LPCVD) at the Cornell NanoScale Science & Technology Facility (CNF). Chemical vapor deposition is a process whereby gaseous reactants are pumped into the deposition chamber and diffuse to the substrate surface where they adsorb and react to form a solid film. The gaseous byproducts desorb and are pumped away. The particular reaction for growing silicon nitride is $3\,SiH_2Cl_2(g) + 4\,NH_3(g) \longrightarrow Si_3N_4(s) + 6\,H_2(g) + 6\,HCl(g)$. The rate is temperature and pressure dependent but by using low pressure, the quality of the thin film is improved [21].

We must comment regarding membrane thickness which is extremely important for device function. The membrane must be sufficiently robust to survive experiments while being flexible enough to deform the full channel height and seal features etched on the bottom. We can estimate the maximum center deflection of the membrane using the formula for 4-side clamped membranes

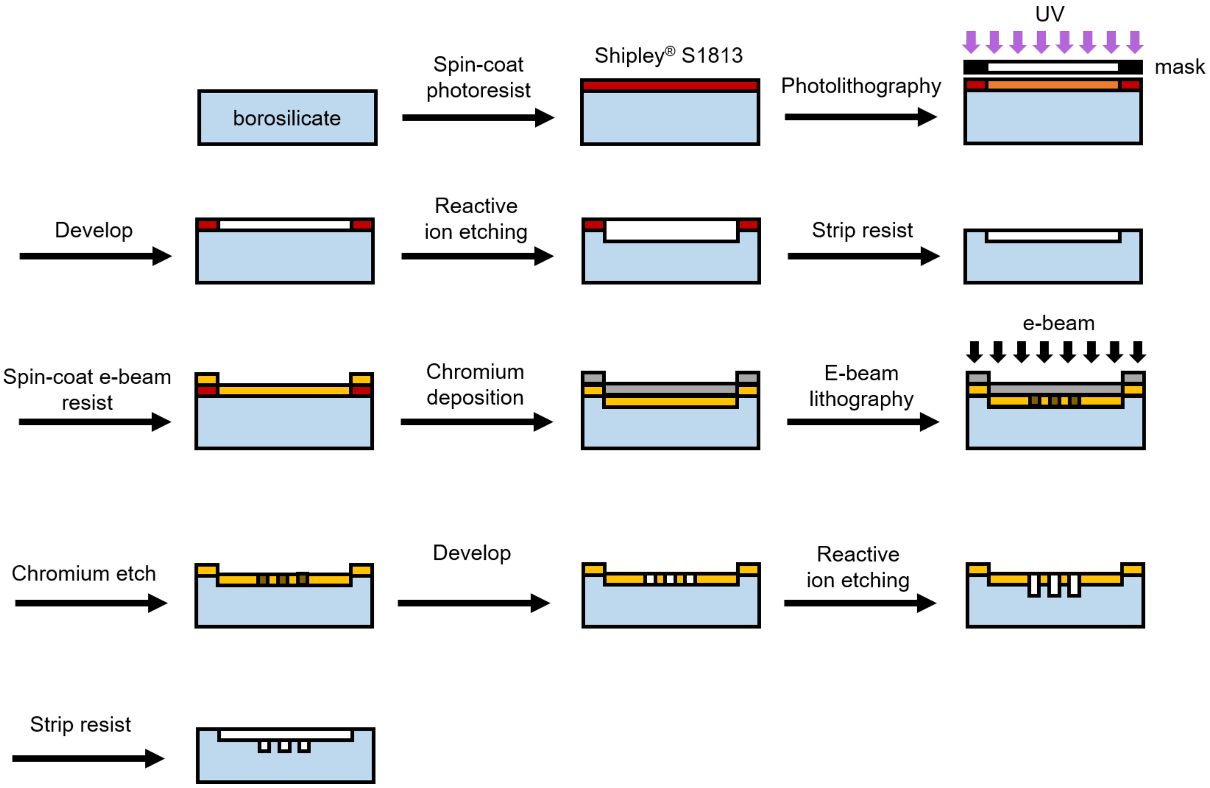

Figure 3.2: Simplified schematic of fabrication process to produce loading channels and trapping features in borosilicate glass. Photoresist is spun on a cleaned borosilicate substrate. Microchannels are exposed by UV photolithography and developed. The channels are etched with reactive ion etching. The substrate is then cleaned thoroughly. E-beam resist is spun on the surface followed by a chromium deposition. The trapping features are exposed with e-beam lithography. The chromium is etched before developing the resist. The trapping features are etched with reactive ion etching as well. The substrate is cleaned thoroughly.

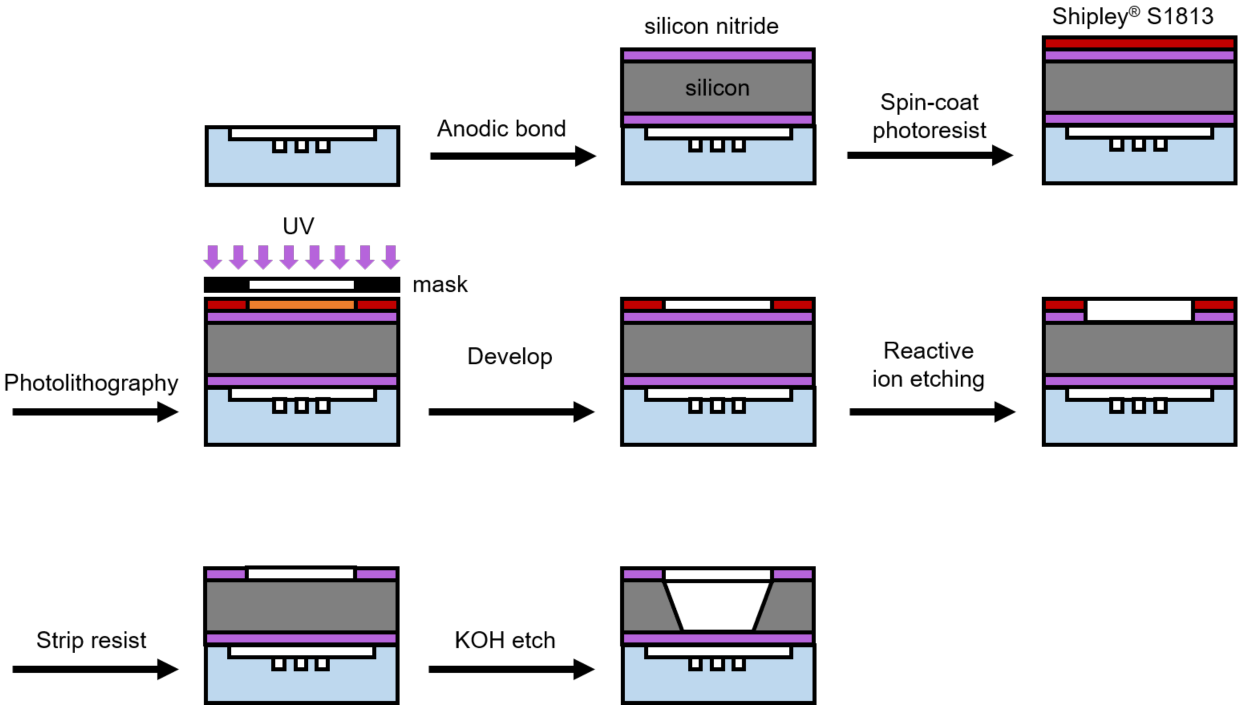

Figure 3.3: Simplified schematic of fabrication process including the anodic bond and all following processes. The cleaned substrate from figure 3.2 is anodically bonded to a double-side polished silicon/silicon nitride wafer. The nitride is 50 nm thick. Photoresist is spun on the exposed nitride surface and access windows are exposed with UV photolithography. After development, the nitride windows are etched, leaving exposed silicon. The wafer is cleaned again. Finally the exposed silicon is etched with a potassium hydroxide solution, leaving suspended membranes over the loading reservoirs and the trapping region. Specialized release steps are detailed in section 3.1.6.

under pressure [10]:

$$w_0 = 0.318 l^3 \sqrt{\frac{ql}{Eh}} \tag{3.1}$$

where w_0 is the maximum deflection, l is the membrane width, q is the applied pressure, E is the Young's modulus and h membrane thickness. By inputting the standard material constants for silicon nitride, the maximum deflection at various pressures for membranes of different dimensions and thicknesses can be predicted (figure 3.4).

As can be seen in figure 3.4(a), 50 nm nitride membranes in standard dimensions ranging from 25 by 25 µm to 100 by 100 µm can easily deflect the full range of the 200 to 400 nm channels used in the trapping devices here.

3.1.2 Photolithography

For features larger than 2 µm, standard optical photolithography techniques are used. It is a robust and reusable technique which can produce good results if some care is taken. UV light is used to transfer a pattern from a hard mask to a photoresist layer which subsequently masks the surface during the etching process.

Substrate Preparation The BOROFLOAT® 33 and silicon/silicon nitride wafers must be carefully prepared before beginnning the lithography process. Surface contaminants, particles and adsorbed water can affect the quality of the transferred pattern. First, the wafer is sonicated in acetone and isopropanol (IPA) before drying. If there is some concern of contamination, it is stripped with an O_2 plasma asher. Following cleaning, surface dehydration may be achieved by baking at 100-200 °C [21]. This step is combined with wafer priming: low pressure hexamethyldisilazane (HMDS), with chemical formula $[(CH_3)_3Si]_2NH$, is used to improve adhesion, especially on surfaces like glass and silicon nitride. The silicon atoms bond with oxygen in a hydroxyl group on the surface releasing $NH_3(g)$. With a single silane layer, the surface is slightly hydrophobic which prevents readsorption of water, improves the spreading of photoresist and protects against humidity [21]. An HMDS priming oven is used which bakes the wafers at 150 °C under vacuum. The entire process of pumping and venting takes around 20 min and involves a 2 min low-pressure HMDS prime. Certain facilities do not have an HMDS oven. In this case, the wafer must be prebaked

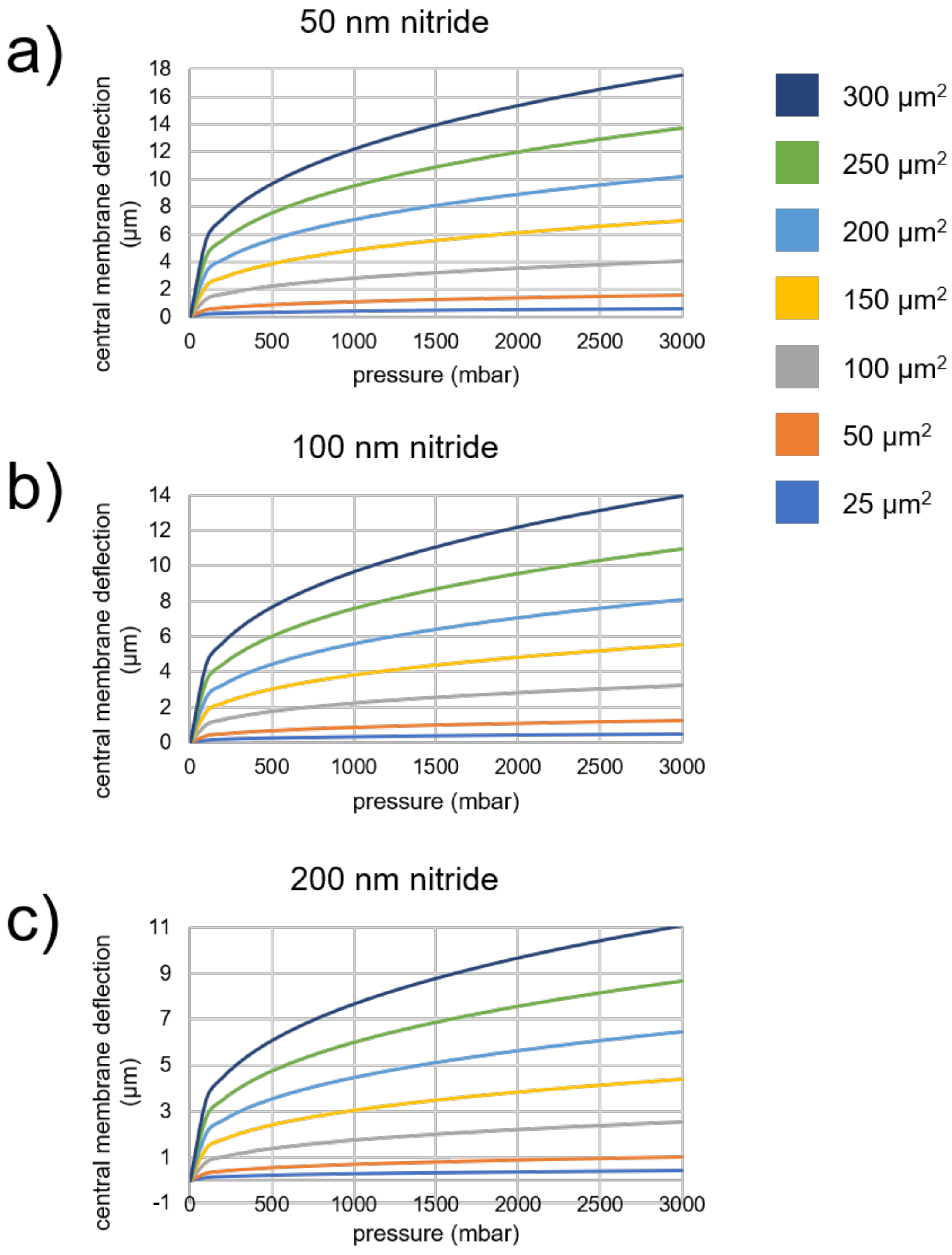

Figure 3.4: Estimated maximal membrane deflection at center due to applied pressure. Plots for silicon nitride membranes with thicknesses of (a) 50 nm, (b) 100 nm and (c) 200 nm.

before spinning a diluted solution on the surface. The ammonia fumes will offgas for some time, so ideally the resist should be spun in a different area to avoid becoming crosslinked by the fumes.

Photoresists Positive photoresists consist of a cross-linked resin, a photoactive compound and solvent. When exposed to UV light, the photoactive compound reacts, forming carboxylic acid and making the resin soluble in a developer. This reaction requires water which is provided by humidity in the cleanroom environment. The unexposed resist is stable and can subsequently act as an etch mask. The solvent lowers the viscosity sufficiently to allow spinning of the resist across the wafer surface. Since resists are sensitive below 450 nm, yellow light is used in the lithography portion of the cleanroom [21]. Shipley Microposit® S1800® series photoresist, which comes in several dilutions to achieve different resist thicknesses, is used primarily for this process. S1813® or S1818® [48] is standard. For special cases, an alternative is the AZ® 9200 series which is much thicker for subsequent deep etches or better resistance against hydrofluoric acid [5].

Spin Coating Photoresist is applied to the center of the stationary wafer (7 to 10 mL), being careful to avoid dripping or introducing bubbles which will negatively affect the uniformity after spinning. First the wafer is accelerated to a low rpm to coat the surface before being accelerated to between 2000 and 6000 rpm which leaves a thin, uniform layer and partially evaporates the solvent. The thickness depends upon the dilution and spinning recipe. A 1.5 to 2 μm layer is desired for this process. Surface contaminants and previously etched structures can effect the spin quality. These features cause streaks of lower thickness resist and in extreme cases, uncoated regions. The former defect is acceptable given that the remaining resist is still sufficient to protect the surface during the etch. In the latter case, the entire lithography process must be redone, starting by cleaning the substrate again.

Soft Bake After spinning, there is still solvent which must be removed before exposure. This is achieved by baking in an oven or on a hotplate. The baking parameters have been optimized to ensure solvent evaporation without affecting the photoactive compound [21]. For the S1800® baking is performed at 115 °C for 1-2 min [48].

Alignment and Exposure The pattern to be transferred is written to a hardmask of chromium coated soda lime glass by a laser writing system. These device masks are written by Front Range Photo Mask in Arizona. For the first lithography step, no alignment is necessary. Each subsequent lithography step needs to be aligned to the first to ensure there is no x, y or rotational offset in the patterns. The mask aligner doubles as an exposure tool which includes a UV light source and a mechanical system to bring the wafer and mask into contact, ensuring the two are parallel [21]. The resolution is limited by contact between the substrate and the mask. The most fine features can be produced by a hard contact between the two but this can introduce contaminants on the wafer surface and resist on the mask surface. Introducing separation between the two surfaces can result in strongly sloped sidewalls and incomplete exposure. Even with ideal contact, there will be a positive slope due to diffraction of light around the chromium mask edges [21]. The masks are cleaned after use to ensure contamination does not affect subsequent exposures on other wafers. The correct UV dose is vital to ensure a good resist sidewall profile. Overexposure will expand features and degrade the edge while underexposure will caused sloped sidewalls and sometimes fail to expose the entire resist layer. A dose of 200 $\mathrm{mJ/cm^2}$ is sufficient to expose 2 µm of S1818®.

Development The exposed regions of photoresist, which are now carboxylic acid, are etched by an alkaline developer. MF®-319 is used for the S1800® series [48] and AZ® 400K for the AZ® 9200 series [5]. Again, care must be taken to optimize the development time. Overdevelopment can cause loss of adhesion while underdevelopment won't form the pattern or leave residue in the feature. Underdevelopment is not as dangerous because the wafer can be submerged in the developer again [21]. In addition some care must be taken removing the wafer from the developer beaker. The etched resist is suspended in solution and can be redeposited on the surface if it is not agitated when removing. The wafer is immediately rinsed in DI water and dried before inspection. For this process the wafers are developed in MF®-319 for 1 min followed by 1 min in DI water.

Hard Bake Following development, another bake step can harden the resist which increases its resistance to reactive ion etching and improves adhesion. The temperature must be below the glass transition temperature of the resist to avoid reflowing into the developed features [21]. In some cases, as was mentioned in section 2.1, this is actually desired.

Descum Finally if very smooth etched surfaces are required, the surface can be descummed using an O_2 plasma asher at room temperature. The plasma will etch a small amount of resist across the whole wafer but this loss is acceptable as the features to be etched are cleaned from any residual resist. This tool can also be used (with heat) to strip resist after etching.

3.1.3 Electron Beam Lithography

For smaller features, optical lithography cannot be employed. The standard is a direct-writing electron beam lithography process which is substantially more involved but allows, in principle, features down to 10 nm.

Metal Alignment Marks To align with an e-beam system, metal alignment marks are standard. 50 nm of gold is typically used with a few nanometers of chromium to help adhesion to the glass.

Substrate Preparation The substrate is prepared similarly as in section 3.1.2 except HMDS is omitted. Only the O_2 plasma asher is used to prepare the surface before spinning.

Electron Beam Resist E-beam resists operate similarly to photoresists but are typically more sensitive and have a higher resolution. ZEP 520A (Zeon Corporation) is spun on the wafer surface [58]. Thickness is typically 200 to 400 nm depending upon the desired etch depth. We use a resist thickness equal to twice the desire etch depth. It is challenging to spin thicker than 400 nm which limits the etched features to 200 nm maximum. Potentially one could spin multiple layers to overcome this limitation but that process has not been characterized yet. It is also challenging to spin over etched features since the ZEP 520A layer is so thin. Usually the ebeam features are etched first to avoid spinning aberrations in subsequent steps. However for the two-chain mixing project a resist layer was successfully spun over microchannel features etched 200 and 400 nm deep. The wafers are then baked at 180 °C for 5 min.

Dissipation Layer A 10 to 15 nm conductive chromium layer is sputtered on the resist surface. This serves as a dissipation layer to avoid charging which would deflect the incoming electron beam, distorting the desired write pattern.

Alignment and Exposure The actual exposure process is performed by a technician at INRS. The wafers have both automatic alignment marks as well as global crosses for manual alignment. Typically manual alignment is requested because the automatic system can fail, resulting in misaligned features. The dose is highly dependent upon the resist thickness and the features being exposed. The resist is primarily exposed by secondary electrons which are produced by the incident beam in the substrate below the resist. As the process is highly technical, the staff at INRS are consulted to select a dose.

Development Following exposure, the chromium layer is etched and the exposed resist is developed. ZED-N50 is used for 65 s, followed by a rinse in IPA and drying with nitrogen. The development time is slightly higher than recommended to ensure the resist is removed [58]. Due to the feature size, it may be impossible to check the quality of the features optically.

3.1.4 Reactive Ion Etching

The nanofluidic features are all etched using reactive ion etching because the features exposed and developed in photoresist can be translated accurately to the substrate. The generic process is seems simple but involves many parameters which must be tuned for a given process. Gases are ionized in an RF field and brought to the substrate surface where they adsorb, react and desorb. The volatile products are removed. Only exposed regions without resist are etched so after stripping the remaining resist, the desired features will be etched [21]. This process is even more complex when etching borosilicate glass. The composition of the glass that allows anodic bonding also results in nonvolatile reaction products that are hard to etch and redeposit on the surface. This results in a rough etch profile which should be minimized in nanofluidics.

Carrier Wafer Most etching chambers are designed to carry six inch wafers. The four inch wafers used for these designs are mounted on larger silicon carrier wafers for loading into the vacuum chamber. Exposed silicon will be slightly etched by the plasma and increase the roughness of the glass etch. To mitigate this, the surfaces of the carrier wafers are covered. At MNM the wafers are spun and baked with a thick layer of photoresist which must be replaced after a few etch processes. At INRS the wafers have been sputtered with 100 nm of chromium. The method of adhesion between the sample and carrier differs between facility as well. MNM uses a water soluble wax which is melted and then solidifies between the two wafers. It is very challenging to avoid some bubbles between the two. At INRS, an oil is used which spreads into a very thin layer between the two surfaces when they are loaded under vacuum. Since thermal contact between the substrate and carrier is vital for uniform etching, the oil is preferable, ensuring a thin layer across the entire wafer area.

Chamber Preparation Contaminants from previous etch processes can affect the quality of the current etch. To mediate this the etch chamber should be cleaned. At MNM a plain silicon wafer is loaded into the chamber for 300 s of O_2 cleaning. INRS does not allow O_2 cleaning so an alumina wafer is loaded and 10 min of the desired etch process is run to seed the chamber. If SF_6:Ar etching will be performed, only 5 min of seeding is run because the etch process is very physical and will attack the alumina surface.

Surface Roughness It is ideal to produce very smooth features as unintended surface roughness can influence experimental measurements. The most common measure for surface roughtness is R_a which is the mean deviation of the surface profile as measured by a profilometer:

$$R_a = \frac{1}{n}\sum_{i=1}^{n}|y_i| = 1 \tag{3.2}$$

where n is the number of sampled points and y_i is the height at each point [18]. An example profile can be seen in figure 3.5. Note the etched surface is not uniform and dips substantially (50 nm) at the edges of the feature. This is representative of a poor etch process.

The roughness can also be estimated optically or with scanning electron microscopy (SEM). Smooth features should appear completely transparent to the eye while roughened features have a gray or foggy appearance. In SEM defects can be visualized directly. An excellent R_a for these devices would be below 10 nm.

SF_6:Ar At MNM a CHF_3:CF_4 etch chemistry was used which resulted in an R_a between 15 and 25 nm. This was sufficiently low for experimental work. INRS however does not have the same source gasses available for RIE. The most promising borosilicate etch processes use SF_6:Ar

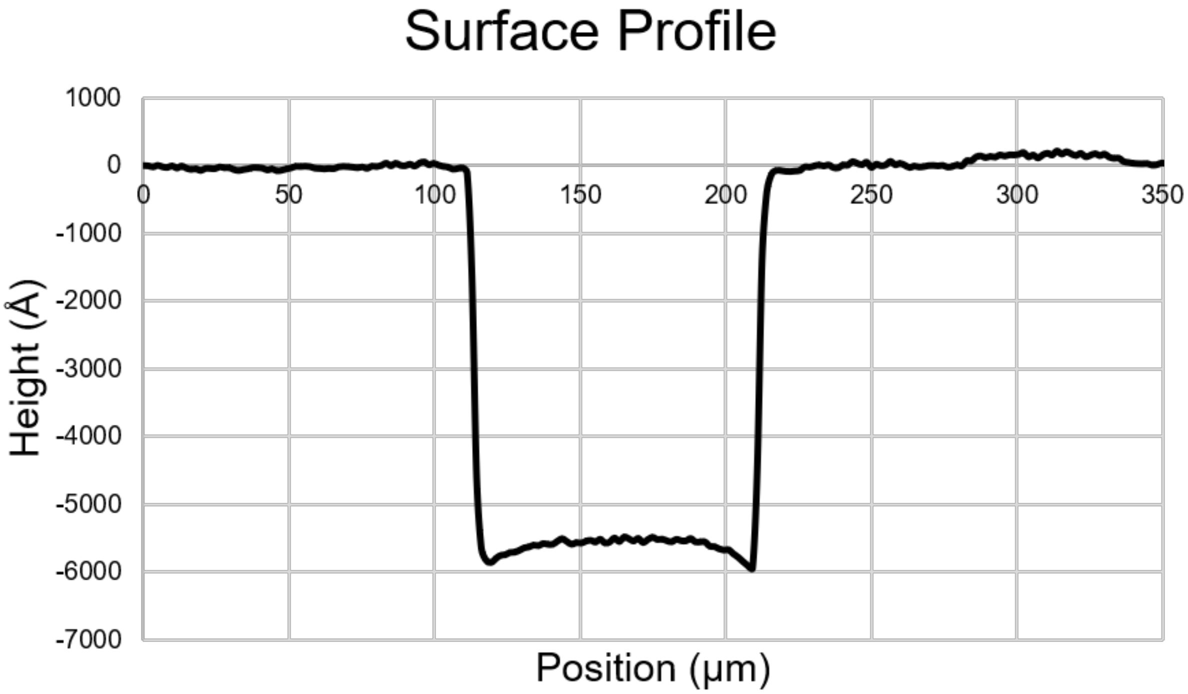

Figure 3.5: Surface profile of 100 µm wide channel, etched approximately 550 nm deep using CHF_3:CF_4 etch chemistry. Curvature at the bottom of the feature is represenative of poor etch process. Data was captured using Ambios® XP200 Profiler at MNM.

in an inductively coupled plasma (ICP) RIE. Normally the substrate and RF plasma power are coupled but with an ICP RIE each can be tuned individually. Thus the plasma density can be controlled independently from the energy with which ions bombard the surface. This allows for low-pressure etching which is ideal for removing etching products and particles from the surface [22, 33, 59]. SF_6 provides the chemical etching component as the fluoride reacts with silicon to form a volatile product. The argon serves as a physical sputtering agent, dicouraging redeposition and aggressively clearing the surface of nonvolatile agents. In particular, the aluminum, sodium and potassium compounds are not volatile and must be physically sputtered. Goyal, Hood and Tadigadapa achieved the best results with these gases, reaching $R_a = 1.97$nm [22]. A recipe was developed for use at INRS, resulting in $R_a = 4.3$nm which is several times lower than the old CHF_3:CF_4 etch chemistry. This uses the Oxford Instruments® Plasmalab 100® system at INRS with the following parameters: 2000 W ICP power, 150 W substrate power, 50 sccm Ar, 5 sccm SF_6, 2 mtorr operating pressure and 20 °C. As can be seen in figure 3.6, this process is competitive with other smooth borosilicate etch processes from literature. Also the quality of the etches can be compared in figure 3.7 where there is a significant reduction in surface defects in the SF_6:Ar etched features. The etch selectivity is 2:1 with a 2 µm S1818® photoresist mask. The etch rate is approximately 165 $\mathrm{nm\,min^{-1}}$.

3.1.5 Anodic Bonding

Anodic bonding is an important technique used in MEMS packaging to permanently bond silicon and glass wafers, usually hermetically sealing open cavities. All the nanofluidic devices described in this thesis are bonded using this technique in the EVG® 501 Wafer Bonding System at MNM.

Substrate Preparation At high bonding temperatures, the borofloat will seal around irregularities and particles up to 50 nm. However the surfaces are thoroughly cleaned immediately prior to bonding to ensure good contact between the surfaces. In figure 3.8(c) the substrates were not well cleaned and large unbonded regions can be seen surrounding particles trapped between the two surfaces. To clean, a piranha solution is used which consists of 3 parts H_2SO_4 and 1 part 30% H_2O_2. The solution heats rapidly when mixed and will aggressively remove organic matter from the surface. The wafers are cleaned for twenty minutes before being rinsed thoroughly with DI

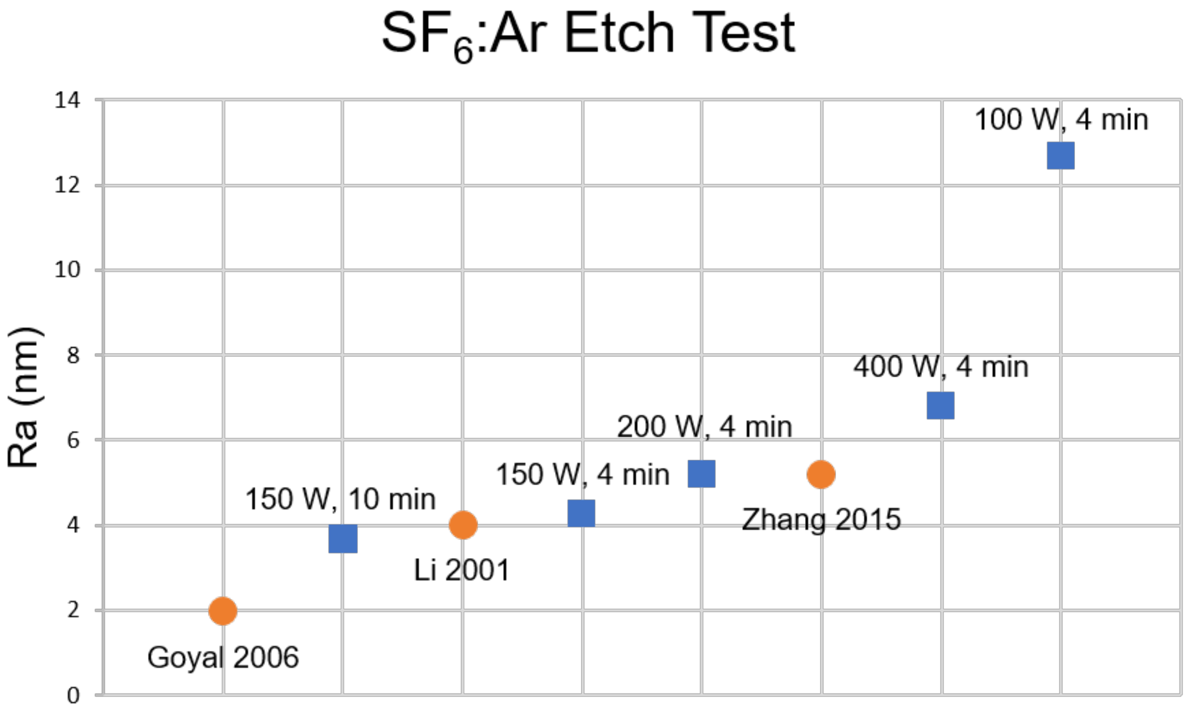

Figure 3.6: Comparison of surface roughness, R_a, as measured by profilometer between SF_6:Ar etch processes at various power and time parameters and competitive borosilicate etch processes in literature. The blue squares indicate SF_6:Ar etch processes developed at INRS for this purpose while the orange circles indicate processes from literature.

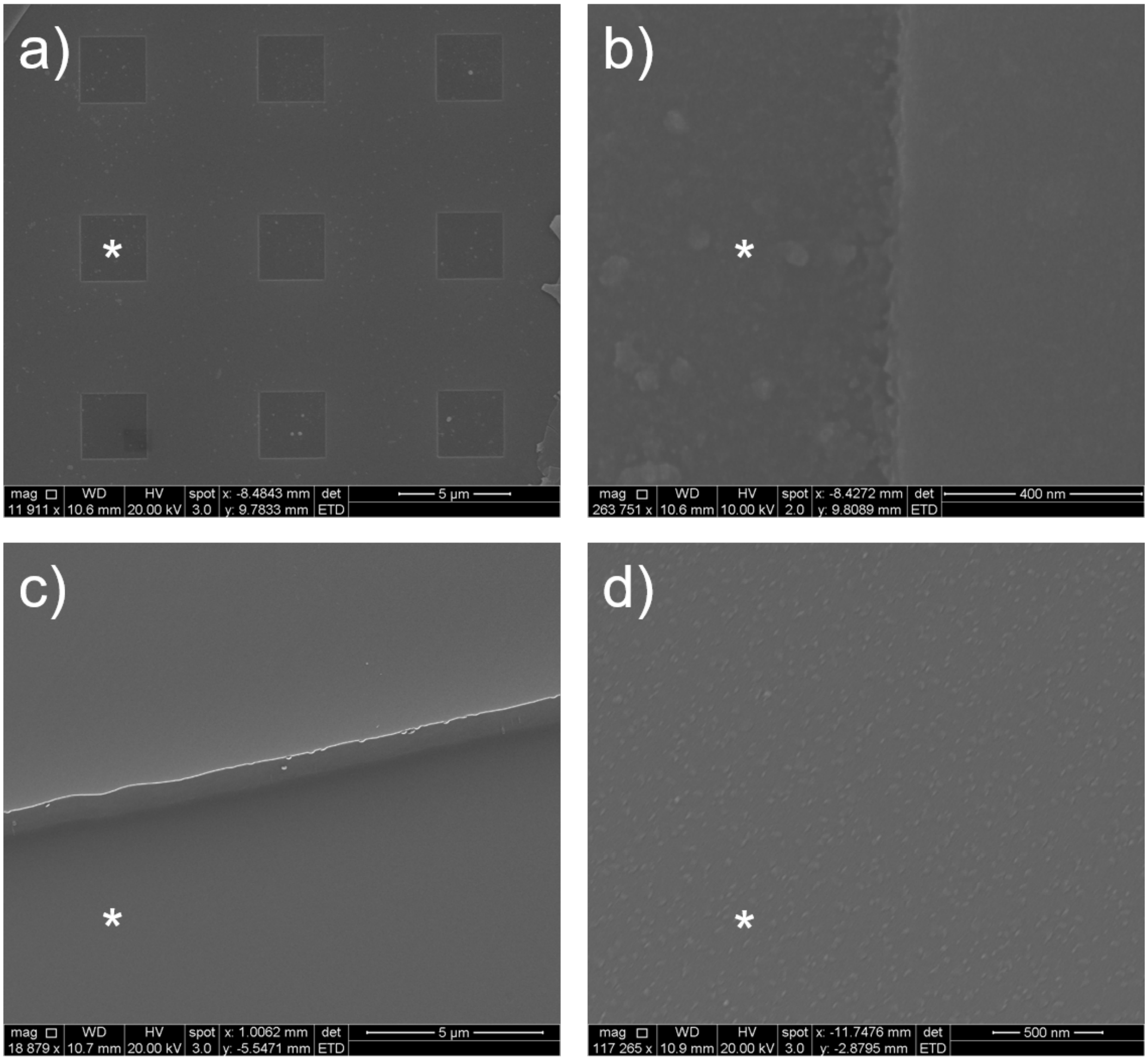

Figure 3.7: SEM images of features etched at MNM using CHF_3:CF_4 etch chemistry and test etches at INRS using SF_6:Ar etch chemistry. In all images the asterisk represents etched regions of interest. (a) Square pit features etched 700 nm using CHF_3:CF_4 etch chemistry. The surrounding region is the channel which has been etched to a depth of only 500 nm. Scale bar is 1 µm. (b) Edge of square pit feature shown in (a). Scale bar is 400 nm. Note the large surface defects which are a result of nonvolatile masking agents. (c) Edge of channel etched 660 nm using SF_6:Ar etch chemistry. The neighboring region is the untouched wafer surface. Scale bar is 1 µm. (d) Etched channel shown in (c). Scale bar is 500 nm.

water and dried. The two surfaces are then pressed together and loaded into the bonder. An alternative to piranha solution is Cyantek® Nano-Strip 2X®. The solution is buffered for safer handling but must be heated between 60 and 80°C to accelerate the cleaning process. In addition it is much more viscous than piranha solution so the wafers should be rinsed in hot DI water or there will be residue left from the Nano-Strip 2X®.

Coefficient of Thermal Expansion The silicon and borosilicate wafers are heated together to 350°C. When the bond process is completed, they will be allowed to cool to room temperature over many hours. The thermal mismatch between the two materials can cause cracking and a poor bond. This is partially why Schott BOROFLOAT® 33 is used as it has a coefficient of thermal expansion (CTE) sufficiently close to silicon to avoid cracking.

Bond Process The bonder applies slight pressure to the center of the wafer to encourage the bond to propegate from the center outwards. This pressure application along with vacuum ensures bubbles are not trapped between the substrates. Once the wafers have stabilized at the bonding temperature the borosilicate will be partially ionized into Na^+ and O^{2-}. Then a voltage of 400 V or higher will pull O^{2-} to the bond interface and push Na^+ to the top surface where they are neutralized. There is a resulting depletion zone which is several micrometers thick about the bond interface (depending upon the applied voltage). The electrostatic force pulls the two wafers together tightly where the oxygen ions react with silicon to form SiO_2, binding the two wafers permanently [21]. A schematic of this principle can be seen in figure 3.9. Typically 1000 V are applied in three, 10 min intervals. The current drops lower and lower for each subsequent bond process, indicating more of the Na^+ has been neutralized and the bond quality is good. A constantly high current is indicative of a short between the two electrodes.

Membrane Bending An important design consideration is the possibility of structural collapse during the bonding process. The two surfaces become very strongly attracted to each other, so shallow features can deflect and bond. Mao and Han bonded silicon-glass wafers with channels in varying dimensions to characterize the minimum aspect ratio. They found this was 0.004 for long channel structures [38]. An aspect ration of 0.002 was achieved here with similar bond parameters. The survival of the structures may be due to the silicon nitride layer between the two bond surfaces.

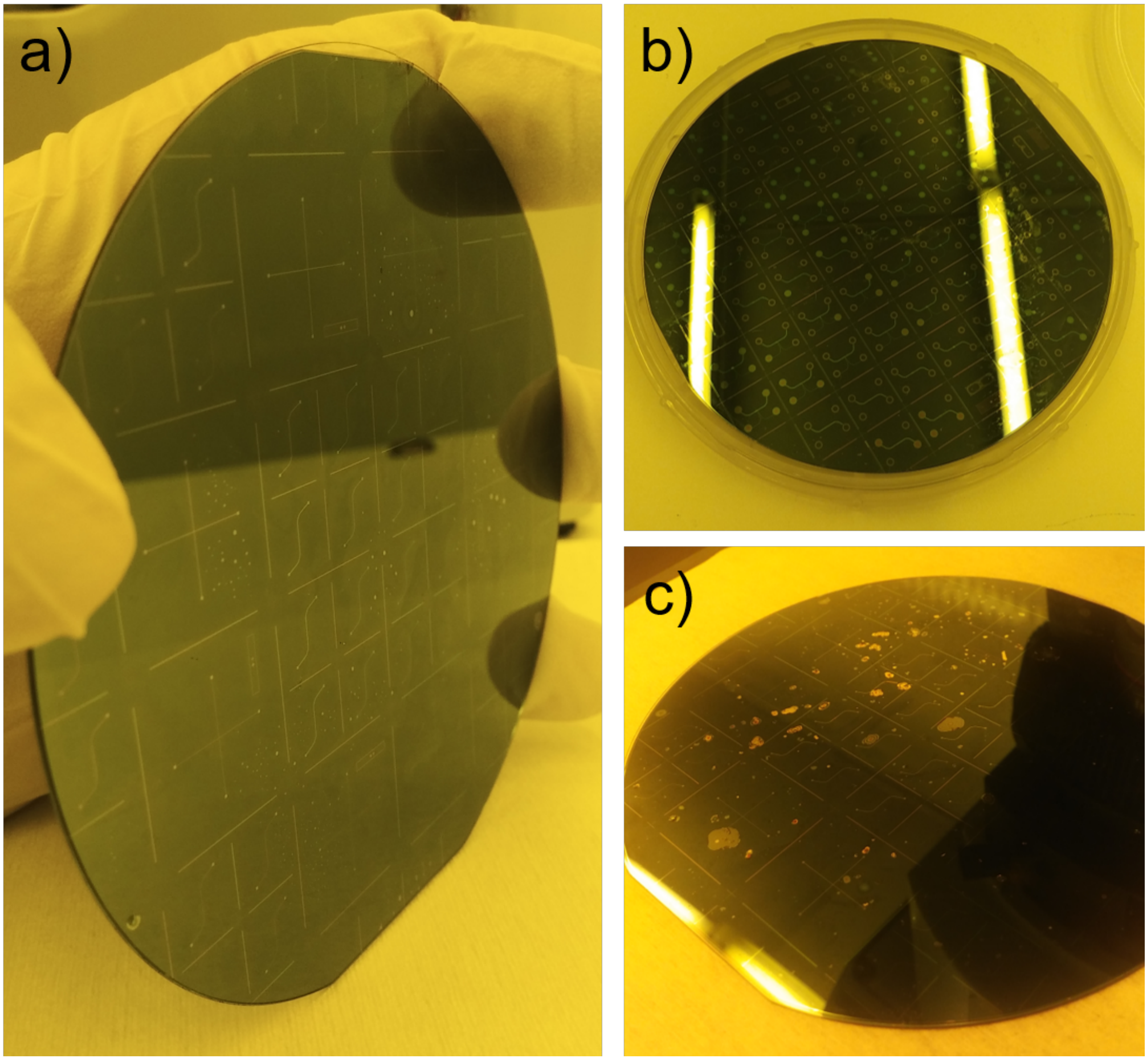

Figure 3.8: Results of anodic bonding process between silicon/silicon nitride wafers and borosilicate wafer with etched features. (a) Acceptable anodic bond quality which was achieved at atmospheric pressure. Small bubbles are from gas trapped between the two surfaces. (b) Traditional anodic bond highlighting membrane collapse. Note the circles in the etched features. The dark circles are regions where the silicon nitride membrane has deflected during the bonding process and bonded to the glass surface. In the light regions, the membrane is still secured to the silicon wafer. (c) Traditional anodic bond highlighting insufficient surface preparation. Note the large unbonded regions which surround particles that were not removed during cleaning.

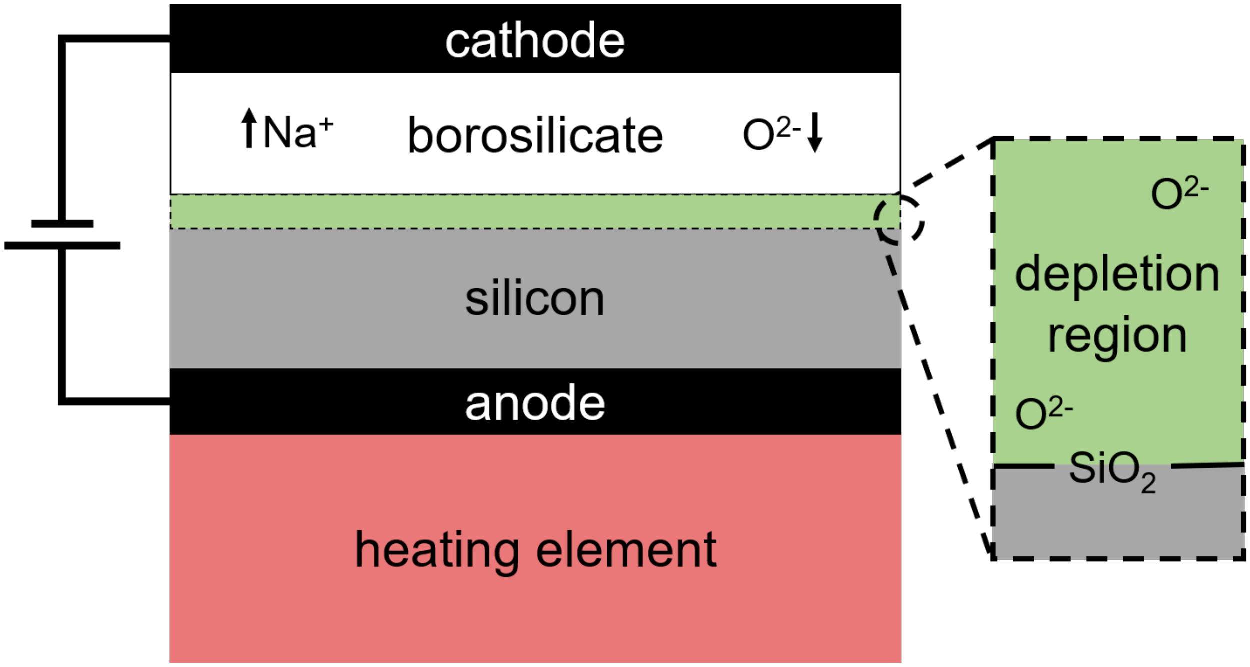

Figure 3.9: Schematic of anodic bonding process highlighting the depletion region and the SiO_2 interfacial bond.

In addition the features used by Mao and Han were etched in the silicon substrate instead of the borosilicate glass. Thicker substrates will also be less prone to deflect and create contact regions [21]. In figure 3.8(b) many nitride membranes have deflected and visibly bonded to the glass surface.

Internal Pressure The bonding process is performed under vacuum which is ideal for many MEMS devices. However after bonding, windows are opened in the nitride to etch the silicon from the top. The nitride membranes are released and this internal vacuum causes them to deflect inward and, in most cases, one membrane will break, equilibrating the pressure. This membrane deflection is illustrated in figure 3.10. Bonding was attempted at atmospheric pressure which resulted in a reduction in bond quality and because the devices are sealed at high temperature there is still a pressure difference across the membranes when cooled. Other methods were adopted to solve this problem during the wet etch process.

3.1.6 Silicon Anisotropic Etching

As can be seen in figure 3.11(a), before the final fabrication step, the devices consist of microfluidic loading channels and nanofluidic trapping features etched in glass and sealed hermetically during the anodic bond process. The last step is also the most challenging. Standard top-side photolithography is performed (figure 3.11(b)) followed by an RIE etch of the nitride (figure 3.11(c)). Finally, potassium hydroxide (KOH) is used to etch the supporting silicon leaving a suspended 50 nm membrane (figure 3.11(d)). This process is very sensitive as there are three membranes for each device (one for actuation, two for loading reservoirs) and if any of the three fail, the device will not function.

Potassium Hydroxide Potassium hydroxide or KOH is used as an alkaline etch solution to anisotropically etch silicon. It etches the (100) crystal plane 200 times faster than the (111) plane which results in a highly anisotropic etch with sidewalls sloped at an angle 54.7° from the wafer flat (figure 3.11(d)) [21]. Etching occurs through the following reaction: $\mathrm{Si} + 2\,\mathrm{OH}^- + 2\,\mathrm{H_2O} \longrightarrow \mathrm{SiO_2(OH)_2}^{2-} + 2\,\mathrm{H_2}$. Etch rate is determined by the concentration of KOH and the temperature. Industry standard is between 20 and 30% KOH in DI water. Temperature has a huge influence. At

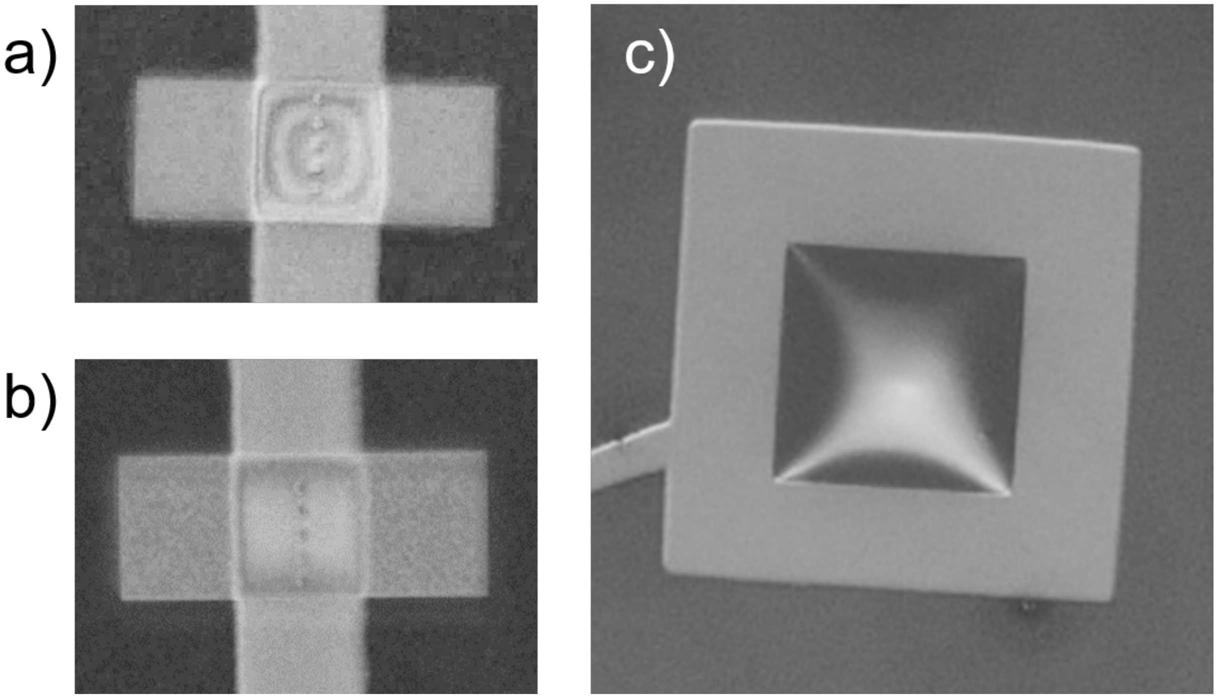

Figure 3.10: Membrane deflection due to vacuum in microchannels sealed by anodic bond. (a) Actuation membrane deflected by internal vacuum. (b) Identical feature after pressure has been released showing the relaxation of the membrane. (c) Loading membrane deflected when channel is still sealed under vacuum.

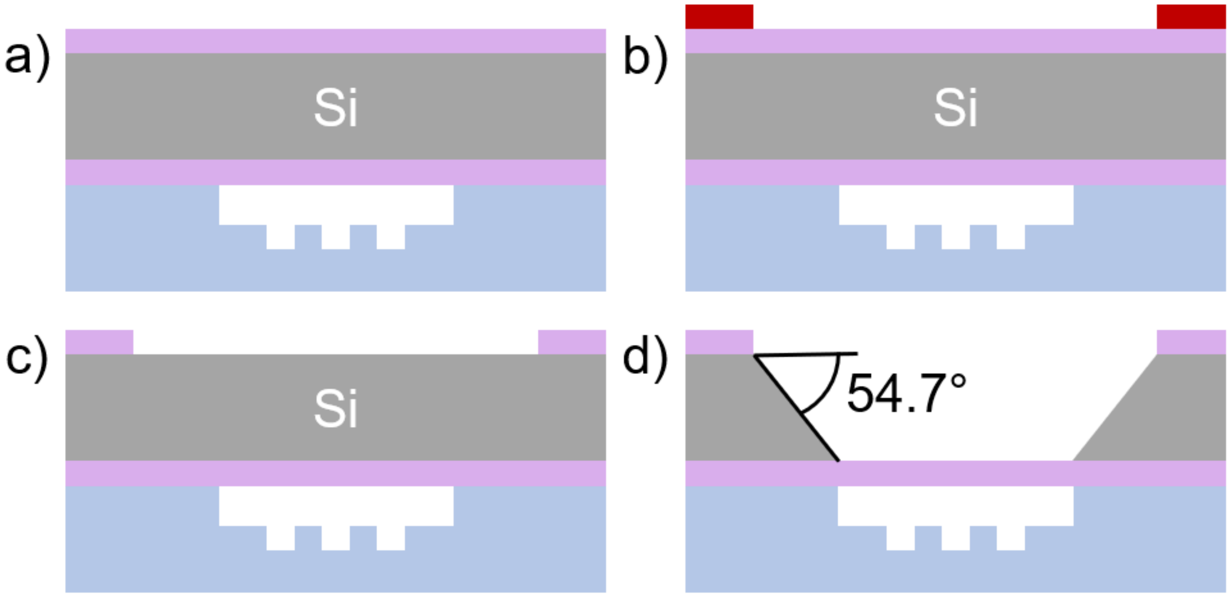

Figure 3.11: Schematic of KOH release process. Gray is silicon wafer with purple silicon nitride. Blue is borosilicate wafer with etched features. Red is photoresist. (a) Wafer after anodic bonding. Features are sealed (usually hermetically). (b) Photolithography process exposes and develops regions to etch top-side reservoirs. (c) RIE etch opening in silicon nitride layer. (d) KOH etch to release thin nitride membrane above features in borosilicate glass.

30% KOH, increasing the temperature from 60°C to 80°C can increase the etch rate by approximately 50 $\mu m\,h^{-1}$.

Residue Formation When the reaction products become oversaturated, the following reaction occurs: $Si(OH)_6 \longrightarrow Si(OH)_4 + 2\,(OH)^- \longrightarrow SiO_2 + 2\,H_2O + 2\,(OH)^-$ where the SiO_2 is an extremely viscous product which diffuses slowly in solution, especially when etching narrow, deep features like the reservoirs in these devices [56]. It can condense into an amorphous silicon dioxide residue (called "waterglass"). The waterglass inhibits the etch rate as it accumulates in features and limits the diffusion of KOH to the silicon surface. In principle this can be mediated by limiting the etch rate to balance the formation of the etch products with the diffusion rate. This would avoid the oversaturation limit. However as will be shown later, this is not feasible in these devices with such small etch windows as the diffusion out of such narrow features is much lower than larger flat surfaces [56]. Sometimes intermediary rinsing steps are used to counter the build up of reaction products.

As mentioned in section 3.1.5 the nitride membrane will deflect and break due to the vacuum in the loading microchannels. The viscous waterglass is pulled into the device features where it condenses into a solid residue, blocking device channels and rendering them useless. This can be seen in figure 3.12(c). This has been the most challenging problem in the fabrication process for which many potential solutions were tested.

Varying Etch Compositions The first, obvious, parameter to vary is the etch composition. The KOH etch rate is both temperature and concentration dependent. A high etch rate gives the reaction products less time to diffuse from the etch front and increases the rate of hydrogen bubbling. Typically the etch is done in two stages. Approximately 350 μm of silicon are etched at a fast rate before dropping the temperature for a slow final release. Isopropanol is frequently added to KOH etch solutions to reduce roughness on the final etched surface but this is irrelevant in these devices which etch completely through to the silicon nitride. Acetic acid was even tested as a buffering agent to reduce the etch rate significantly but it was not only very dangerous to mix but roughened the silicon sidewalls. None of these variations significantly improve the yield.

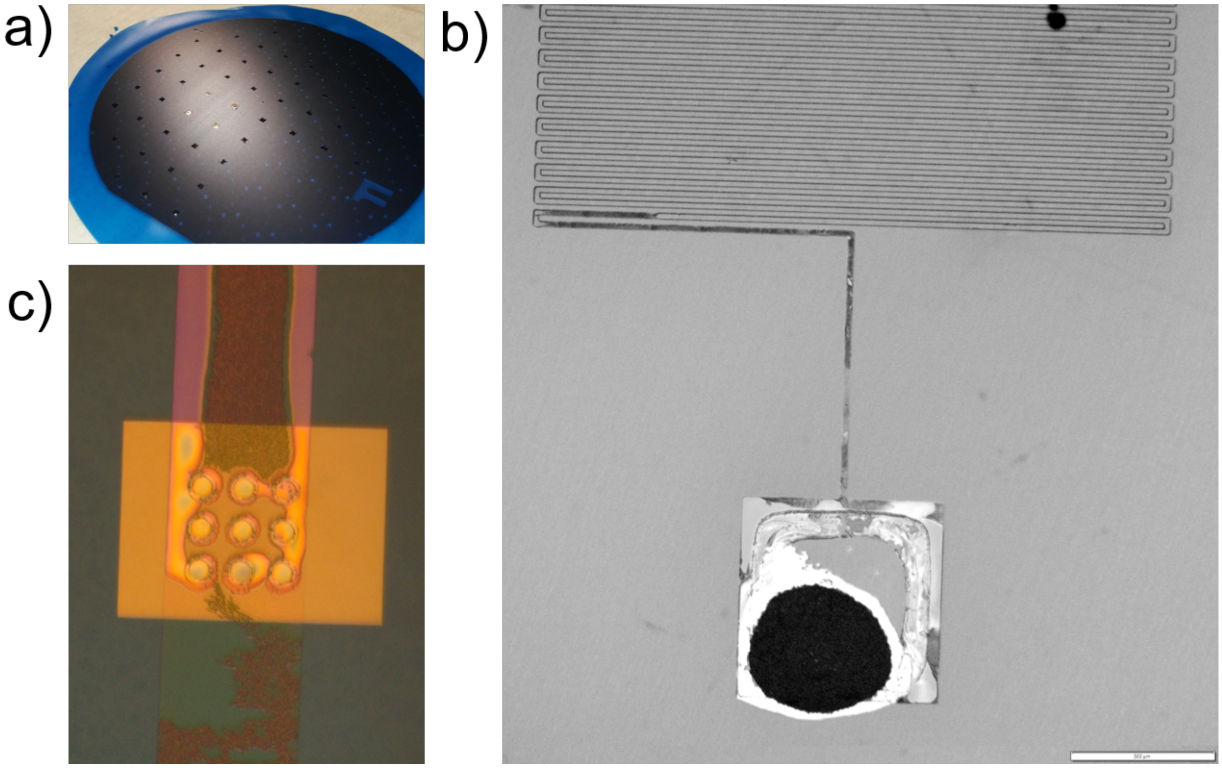

Figure 3.12: (a) Wafer masked with blue dicing saw tape prior to sandblasting. (b) Residue trap after membrane release. The sacrifical membrane was released prior to the final KOH etch and then sealed again with ProTEK® PSB. Waterglass that entered the trap condensed in the narrow channel, leaving the device operational. (c) Device with residue blocking the microchannel and filling the cavity features. Scale bar is 500 μm.

Residue Trap It became obvious that varying the etch composition was not sufficient to solve the membrane breakage and residue formation issues. It seemed that no matter the parameters, one membrane would always fail (usually a membrane from a large loading region). In a new iteration of designs a sacrifical membrane was added with a much larger area than the other membranes. It was unsupported and connected to a narrow channel which passed back and forth many times before joining with the loading channel. The hypothesis was that the sacrificial membrane would break upon release, and relieve the pressure differential. Waterglass pulled into the device would condense in the narrow channel trapping region before reaching the loading channel. Unfortunately the larger membrane was not always the first to fail so the yield remained quite low.

Sandblasting The internal channel pressure remains the primary challenge with membrane release. Devices with the aforementioned residue trap were still more successful than the standard version, so to relieve internal pressure, a sandblasting unit is used to release the sacrificial membrane in air and equilibriate the channel pressure. The face of the wafer is masked with dicing saw tape to protect the surrounding silicon nitride which masks the silicon from being etched by KOH outside the membrane regions (figure 3.12(a)). The opening is then sealed with Brewer Science® ProTEK® PSB, an alkaline-etch resistant photoresist, to inhibit residue formation [15]. The membranes are released with a low temperature KOH etch. The ProTEK PSB is not sufficient to seal the trap but residue is halted in the narrow trap channel as can be seen in figure 3.12(b). This leaves the device completely operational and has high yield.

Etch Chuck A chuck was designed as an alternative to the ProTEK® PSB. The chuck can be seen in figure 3.13. The bulk material is polytetrafluoroethylene (PTFE) which is resistant to KOH. 316 stainless steel, which is also resistant, is used for the nuts and bolts. The o-rings are chemically-resistant viton. They can survive only a single etch as they are still damaged by the KOH solution. While the chuck serves its purpose, many devices crack due to the stress placed on the edges by sealing tighly. Also each chuck is hand-machined and devices must be loaded individually which makes it impractical for a full 64-die wafer.

Cleaning To remove the KOH and etch products, the devices are carefully dipped in a series of DI water baths before being dried and stored.

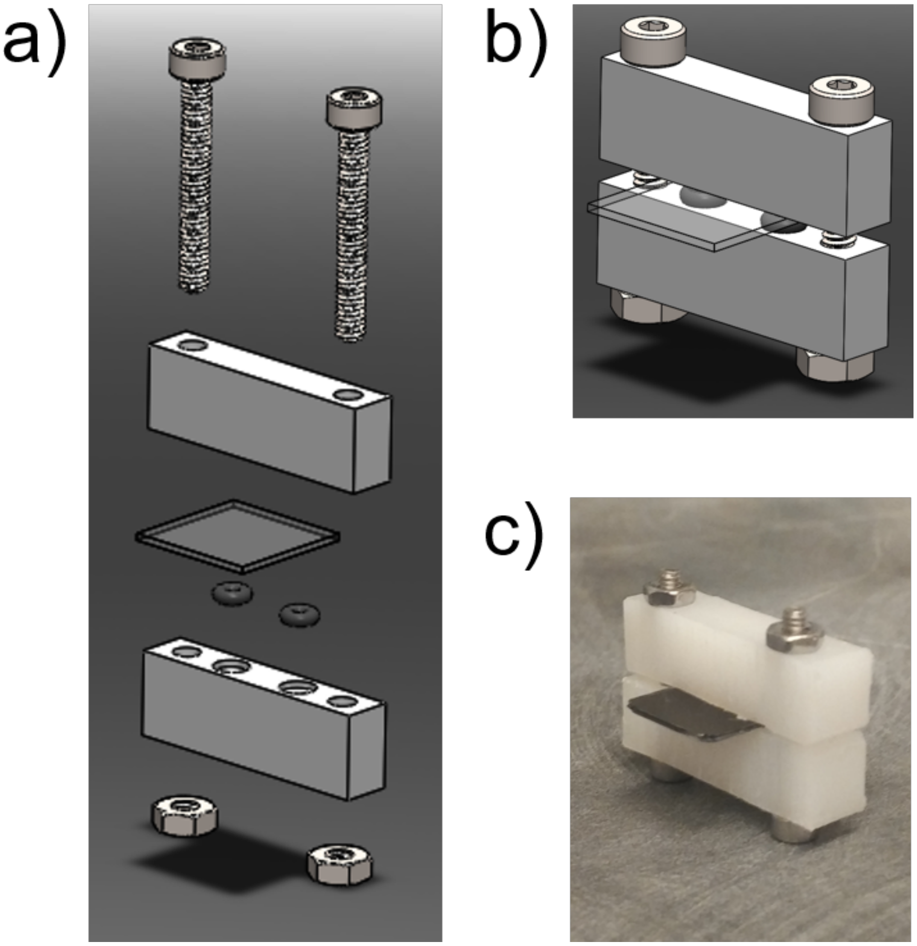

Figure 3.13: Polytetrafluoroethylene (PTFE) chuck designed to seal sandblasted opening in device for final KOH release. (a) Magnified schematic of etch chuck showing assembly. (b) Schematic showing fully assembled chuck. (c) Machined etch chuck with 1 by 1 cm device mounted and ready to enter KOH solution.

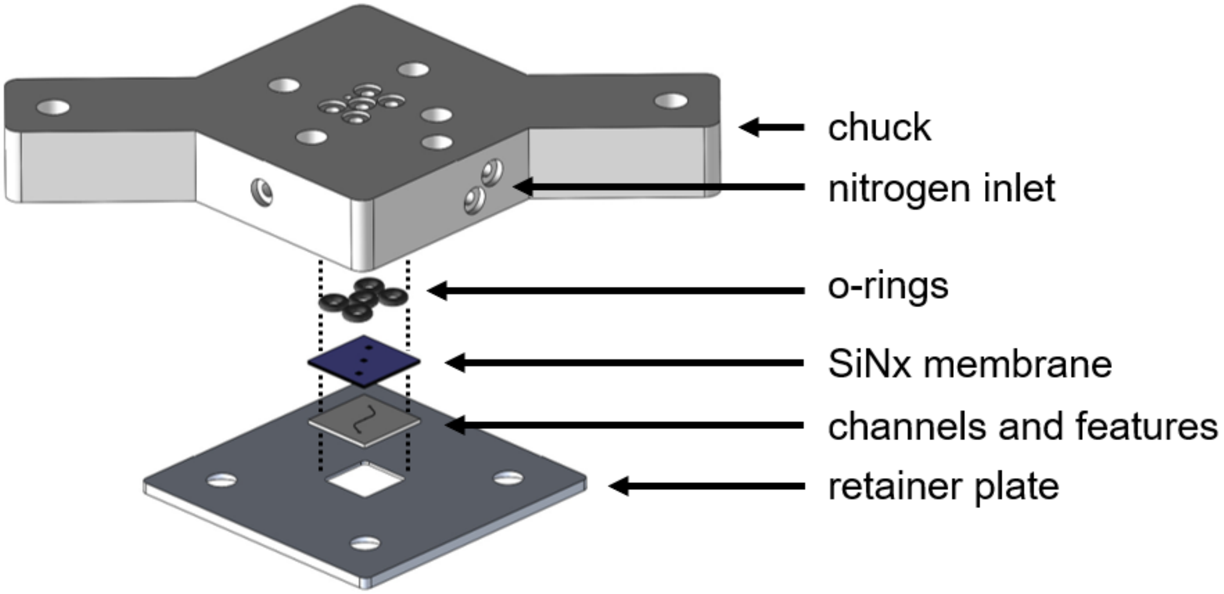

Figure 3.14: The 3D-printed chuck used to mount nanofluidic devices for microscopic imaging. Luer lines can be interfaced to apply nitrogen pressure to drive DNA down the loading channel. Additional pressure lines deflect the silicon nitride membrane lid over the trapping region.

3.2 Device Mounting Chuck

To run experiments, the 1cm^2 device must be interfaced with pneumatic tubing, fully sealed against leakage and mounted on the microscope stage for imaging. Plastic mounting chucks are used for this purpose (see figure 3.14). The chucks were previously machined which is time-intensive and challenging as plastics can easily melt and destroy drill bits during the machining process. In addition it is hard to create chucks with intersecting channels for combined fluidic delivery and pneumatic actuation. With improvements in technology, 3D printing is now a viable alternative. In particular stereolithography allows suffiently fine features to produce high quality mounting chucks.

3.2.1 Stereolithography

Stereolithography is a 3D printing method that involves exposing regions layer-by-layer in a bath of photosensitive polymer. This results in very high-resolution prints as it is primarily limited by the optics and the ability to remove excess liquid polymer from the condensed features [4]. Our chucks are manufactured by Proto Labs® who claim a minimum resolution of approximately 70 µm. This technology has been used to fabricate fully functional microfluidic devices with channels as narrow as 10 µm in SU-8 [4]. Proto Labs® prints the chucks in Watershed® XC 11122 by DSM Somos®. It is the recommended plastic for microfluidic 3D printing as it boasts excellent clarity and fluid resistance [20].

3.2.2 Design Considerations

Gaskets The screws that seal the loading ports on the chuck are outfitted with chemically resistant viton o-rings. The interface between the nanofluidic device and the chuck uses soft polydimethylsiloxane (PDMS) o-rings that are custom cut for this purpose. They are softer and thicker than the commerical viton o-rings which results in a better seal.

Tubing Connections Pneumatic tubing is attached to the chuck using a barbed tube fitting that is screwed to the chuck with a Buna-N o-ring. This is the most common leakage point so the o-rings are replaced frequently.

Retainer Plate An aluminum plate is used to tightly secure the device against the PDMS o-rings. This is the only component that must still be machined. It is thin and has a beveled opening for the objective while still securing the entire outer edge of the device. The whole plate is secured with four screws. Great care must be taken when securing the device with the retainer plate. Each screw must be tighened evenly to ensure the device rests flat. Because these screws are secured tightly, plastic threads in the chuck would inevitably accumulate damage and fail. To avoid this, metal thread-locking inserts are used which allows tightening without inhibition.

3.2.3 Testing

Once the entire chuck has been secured. It will be submerged in DI water and nitrogen pressure will be released in each pneumatic line to ensure there is no leaking around gaskets or the retainer plate. Once successful, the entire setup can be mounted in the microscope.

3.3 Experimental Procedure

3.3.1 Buffers

DNA Double-stranded λ-DNA is isolated from an E. coli lysogen which was infected by lambda bacteriophage. The molecule, which is 48,502 base pairs in length, is extracted and dialyzed against 10 mM tris(hydroxymethyl)aminomethane (Tris)-HCl (pH 8.0) and 1 mM ethylenediaminetetraacetic acid (EDTA). The DNA is frozen before being shipped to our facility (from New England Biosciences). pCMV-CLuc 2 control plasmid DNA which is circular with 6900 base pairs is also shipped frozen in a 10 mM Tris-HCl (pH 8.0) and 1 mM EDTA solution.

Staining λ-DNA has twelve unpaired nucleotides at each end of the molecule. Normally they serve to circularize the chain after being injected into the target bacteria. The DNA is heated to 60°C and cooled rapidly to damage these unpaired binding site and avoid cicularization. The molecules are then stained with either YOYO-1 iodide ($C_{49}H_{58}I_4N_6O_2$)or YOYO-3 iodide ($C_{53}H_{62}I_4N_6O_2$). Both are stained with a 10:1 ratio (DNA base pairs to die molecules). This ratio is used because the persistence length does not deviate from unstained DNA **??**. The DNA, which arrives at a concentration of $500 \mu g\, mL^{-1}$ is diluted to $50 \mu g\, mL^{-1}$ in a TE buffer which consists of 10 mM Tris which has been buffered with hydrochloric acid to an 8.0 pH and 1 mM EDTA. The stains are diluted from their stock concentrations of 1 M to 100 µM. The solutions are allowed to set for an hour before checking quality of the staining.

Antioxidant β-mercaptoethanol (BME) is used as an antioxidant to help preserve DNA against photobleaching and photonicking during the experiments (chemical formula $HOCH_2CH_2SH$). BME at 2% (vol/vol) is added to the dilution buffer and mixed thoroughly (due to its viscosity) immediately before adding the concentrated DNA and beginning the experiment.

3.3.2 Device Mounting

The device is always prepared in advance with an O_2 plasma for 2 min followed by degassing in the experimental buffer (usually 10 mM Tris which has been buffered with hydrochloric acid to an 8.0 pH). The device is then mounted on the chuck described in section 3.2. The reservoir above the flexible membrane for pressure-actuation is filled with buffer to avoid introducting index contrast during imaging. One of the loading reservoirs is filled with the DNA solution. The chuck is completely sealed with luer connections to the nitrogen control.

3.3.3 Pneumatic Control

The loading reservoir has a luer connection to a manual nitrogen control for DNA loading. The DNA solution is pushed to the center of the device, beneath the actuation membrane for trapping. Fresh DNA can be pushed into the field of view by manually operating the nitrogen control for this reservoir. The actuation membrane is operated with a Parker® VSO-BT Electronic Benchtop pressure controller run with a custom NI LabVIEW program. The controller is calibrated before each use with a manometer. The combination of manual and programmable pressure control makes it easy to run many trapping experiments quickly. Fresh DNA can be pushed under the trapping lid, trapped, imaged, released and repeated in only a few minutes.

3.3.4 Acquisition

Imaging is performed by a Nikon® Eclipse Ti inverted microscope with a Nikon® Plan Apo VC 100x oil-immersion objective and an Andor® iXon X3 EMCCD camera. The illumination source is an Excelitas® X-Cite metal-halide lamp. The camera is cooled to -70°C for imaging. For two-color imaging, a mechanical filter turret rotates between two filters for each frame.

3.3.5 DNA Trapping

In figure 3.15 many λ-DNA chains are trapped in microscale features. A highly concentrated solution of λ-DNA ($10\ \mu\mathrm{g\,mL^{-1}}$) is loaded into a side reservoir. A pneumatic valve is opened and the DNA is pushed to trapping region. The valve is closed, leaving many molecules in the channel above the trapping features (figure 3.15(a)). There is still some small capillary flow. The pressure controller is used to apply 3000 mbar nitrogen pressure to the trapping lid ramped over 100 ms. Immediately following trapping, some chains are extended between two features or trapped between the substrate surface and lid. They can be seen extended in figure 3.15(b). They quickly fall into the features and, over 12 min, spread to reveal the trapping geometry (concentric circles)

(3.15(c-d)). Images can be recorded until DNA begins to photonick. At that point the actuation pressure is released, allowing molecules to escape the trapping features. By applying pressure from the loading reservoir again, the old DNA is flushed down the channel and fresh chains are brought into the field of view.

3.3.6 Fluoresence Mapping of Device Topography Following Complete Membrane Deflection

During experiments with fine features (300 nm pits) it was not possible to fully confine a λ-DNA coil in the etched volume at 3000 mbar. The nitride membranes used in our pneumatic actuation devices are compressed completely against the substrate at this pressure so that λ-DNA was trapped between the flat substrate and the lid. Refer to figure 3.16(a) and (d). As was noted in section 3.1.4 (figure 3.7(b)), pillar-like defects are present on the surface due to nonvolatile agents masking the RIE etch process. When the lid is depressed, it will be 'tented' with small pockets of buffer around the raised features. λ-DNA can be trapped in this volume as shown in figure 3.16(b).

Instead of imaging fluorescently labelled molecules, a fluorescent buffer can be used directly. The fully depressed lid will stretch over surface defects, as mentioned previously, leaving a small volume of fluorescent buffer (figure 3.17(a)). The surface roughness can be mapped, giving us a 3D surface plot highlighting defects for a fully enclosed device. This effect is shown in figure 3.18. The uniform array of features is a nanoscale pit array (300 nm, 5 µm spacing) that would be very hard to image normally. This device was particularly rough because it was etched using the CHF_3:CF_4 etch chemistry at MNM. Using this technique, the features can be observed clearly. In addition, because the system is stable, it can be imaged for extended periods of time to improve the mapping quality.

The fluorescent buffer used in these experiments is 0.001% fluorescein ($C_{20}H_{12}O_5$) in DI water. It is a nontoxic fluorescent tracer used widely in medicine and microscopy. The 0.001% concentration is used because at this concentration, for thin volumes, the intensity scales linearly with thickness of buffer layer [45]. The 50 nm nitride lid is depressed with 3000 mbar pneumatic pressure. Video is recorded for several minutes and an image is produced by averaging over all frames. Finally a 3D plot is generated in ImageJ with height scaling with pixel intensity.

Several future directions will be explored using this technique. After calibration of dye fluo-

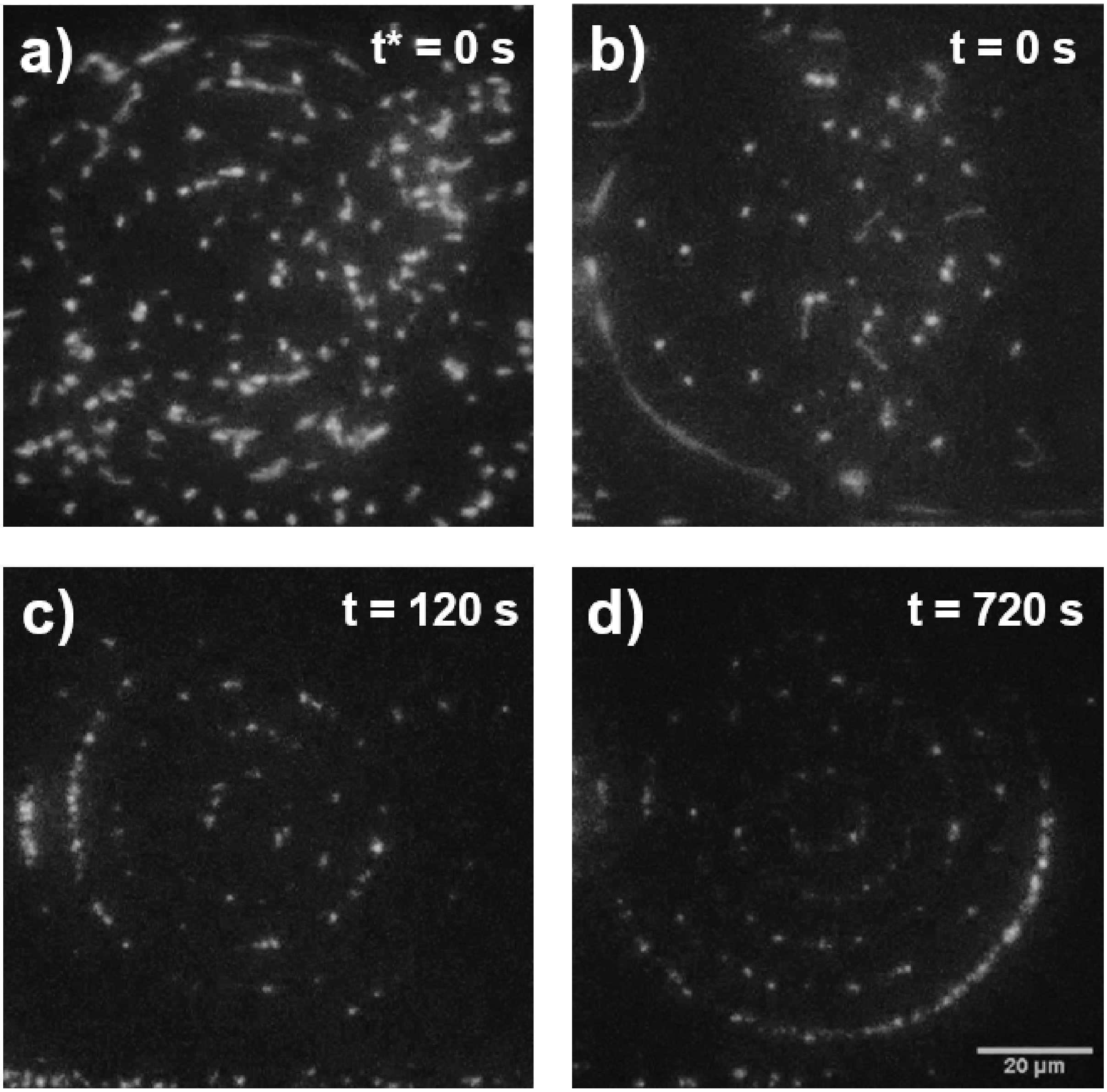

Figure 3.15: Demonstration of trapping capabilities of the devices. (a) Concentrated solution of λ-DNA (10 µg mL^{-1}) loading into microchannel by applying pressure in loading reservoir. (b) Membrane is actuated pneumatically (3000 mbar ramped over 100 ms) to trap DNA in pattern of concentric rings. (c-d) DNA is allowed to relax in rings, spreading to fill the circumferance and revealing the trap geometry. Scale bar is 20 µm.

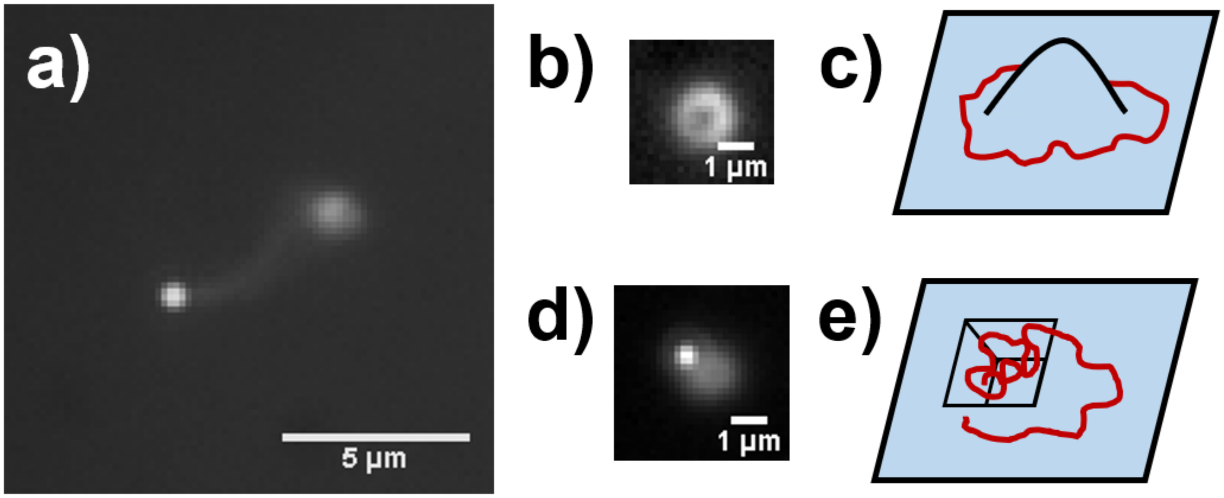

Figure 3.16: DNA trapping in small features and surface defects (3000 mbar. (a) λ-DNA trapped in 300 nm pit feature. Pit volume is occupied and the excess chain length is trapped directly between the substrate surface and the lid. Scale bar is 5 µm. (b) Surface has a pillar resulting from masking during the RIE etch. λ-DNA is trapped around the feature. Scale bar is 1 µm. (c) Schematic of λ-DNA in (b) trapped around a pillar on the substrate. (d) λ-DNA trapped in 300 nm pit feature. Pit volume is occupied and the excess chain length is trapped directly between the substrate surface and the lid. Scale bar is 1 µm. (e) Schematic of λ-DNA in (d) trapped in 300 nm pit feature with excess coil length trapped directly between substrate and lid.

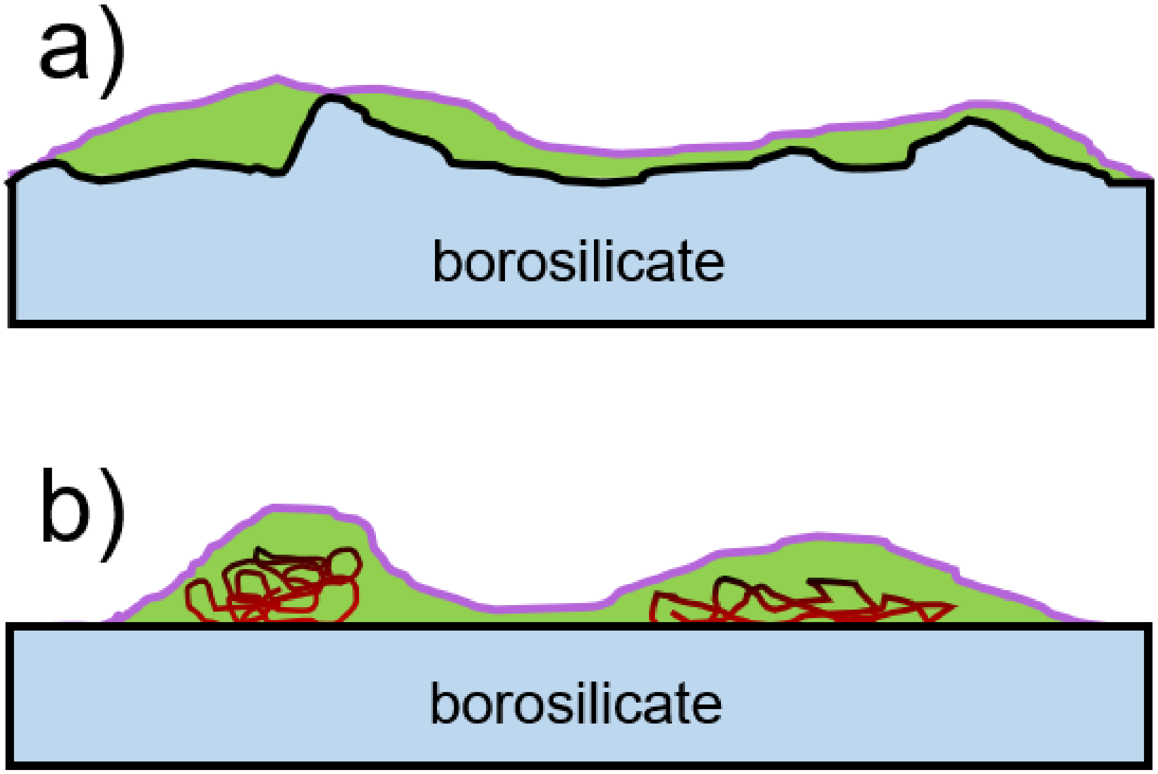

Figure 3.17: Schematic of fluorescence mapping of surface topography. (a) Nitride membrane is fully depressed over a rough surface. Regions ‘tented’ by the nitride have a higher concentration of fluorescein which can be imaged. (b) Along similar lines, with a sufficiently smooth surface, large macromolecules can be pressed against the surface and mapped without being stained themselves.

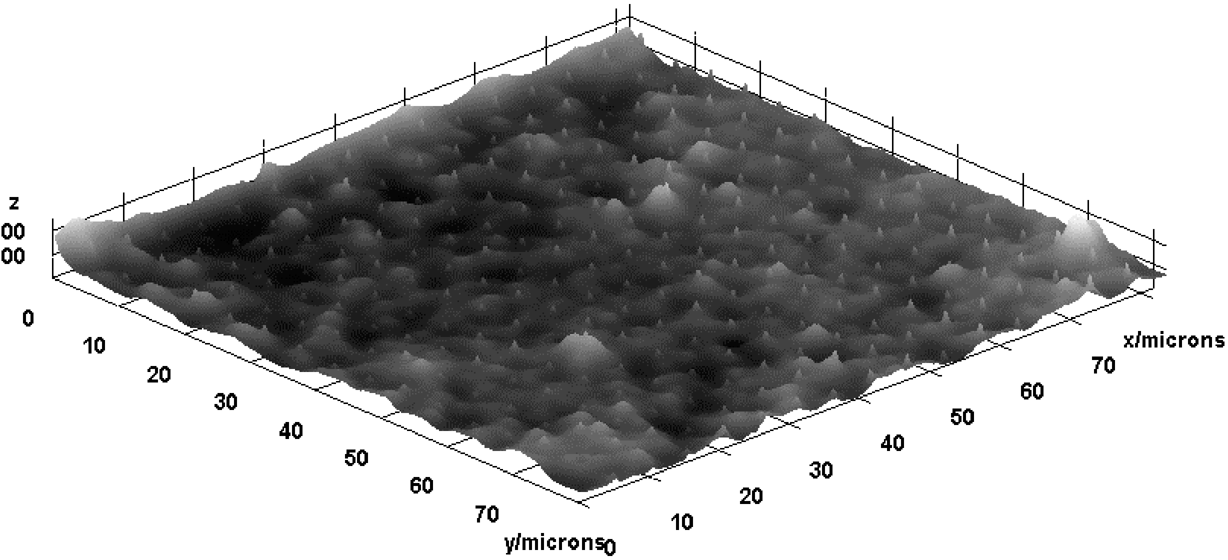

Figure 3.18: 3D plot of fluorescence mapping data. Regular array is an array of 300 nm pit features with 5 μm spacing superimposed on surface roughness. Pneumatic pressure (3000 mbar) was applied to 50 nm nitride lid for everal minutes and the captured video was averaged to produce an image.

rescence to feature depth, surface roughness can be mapped quantitatively in a sealed device which would otherwise only be possible by cracking the device and performing atomic force microscopy (AFM). As seen in figure 3.16, macromolecules can be trapped directly between the substrate and lid. Future work will explore imaging unstained, trapped macromolecules in fluorescent buffer (figure 3.17(b)). This would parallel imaging techniques like cryo-SEM by restraining molecules of interest against the substrate and mapping them. Exploratory work will be performed using silica beads of known dimension to create tent-like defects. Different fluorescent buffers (such as Cy5) will be tested. New fabrication processes will be developed to produce flat trapping surfaces, minimizing the aforementioned etch defects.

Chapter 4

Trapping of Multiple Molecules in Pneumatically Actuated Cavity Devices

A distinct advantage of active confinement is the ability to confine multiple molecules into a single feature which is otherwise impossible in static devices [28]. As a first application, our pneumatically actuated trapping device is used to confine and study two DNA molecules. The device has cavity features 2 µm wide and 200 nm deep. The dimensions, while not exact, are on the same order of the E. coli cell which is a biological environment where we see multiple DNA chains interacting, especially when infected by the lambda phage. Using only a single trapping region, we are able to study the dynamics of single and two-chain trapping. Single trapped molecules are strongly confined vertically but only weakly confined laterally which results in a slightly increased gyration radius and reduced diffusion. When *two chains* are confined together, the lateral confinement is no longer weak. The conformation and dynamics of the molcules are strongly influenced by their interaction. Specifically, identical chains with a coil size on the order of the cavity width (48.5 kbp λ-DNA, confined in 2 µm wide, 200 nm deep cavities) segregate in the cavities and have a conformation altered by the presence of the second chain. Dynamically, the chains undergo Brownian rotation about the cavity center and have drastically altered diffusional relaxation times. As mentioned previously, this study is only possible in an active confinement system with embedded nanocavity (0D) features. In addition, the behaviour of a small plasmid molecule trapped with a larger coil is explored (6.9 kbp plasmid with λ-DNA is in 2 µm wide, 200 nm deep cavities). While the plasmid can diffuse across the λ-DNA coil, the plasmid has a weak interaction effect on the spatial organization of the λ-DNA. The results of this study are currently in review in the journal *Soft Matter*.

4.1 Experimental Procedure

The studied polymer constructs are λ-DNA (48.5 kbp, linear topology), stained with YOYO-1, and λ-DNA or pCMV-CLuc 2 Control Plasmid DNA (6.9 kbp), stained with YOYO-3. The device is prepared and mounted as described in section 3.3. A background image of the nanocavities is captured for both YOYO-1 and YOYO-3 channels. Analyte containing buffer is then introduced in the loading reservoirs and pumped to the nanocavity array. Nitrogen pressure is manually increased to push DNA to the membrane region. Once a large number of molecules have been pumped to the cavity array and are beneath the flexible membrane, the transport pressure is released and the molecules are brought to a halt . The membrane pressure is ramped to 3000 mbar over a time range of 10-100 s. If two molecules are trapped in a single cavity, a video is captured. The differentially stained molecules are imaged together by a rotating filter turret which gives a time resolution of 0.84 fps, or a single molecule out of the pair can be imaged in a single channel at 23.49 fps. After recording, the membrane pressure is released and channel pressure is increased to bring fresh unbleached DNA into the field of view. The experimental procedure is then repeated to ensure sufficient statistics.

4.2 Results and Analysis

4.2.1 Fluorescent microscopy

For each DNA population sample, 10-15 videos are captured, each containing 100 frames. For each video only the regions corresponding to the cavities where DNA chains are confined are selected. To reduce the influence of the background, background intensity (without DNA present) is averaged over 100 frames and subtracted from each video. Figure 4.1 shows a time-series of single-molecule (figure 4.1(a-b)) and two-molecule (figure 4.1(c-d)) dynamics in a single cavity. For each DNA population sample 15 videos are captured. Comparing figure 4.1(a) and figure 4.1(c), we can observe qualitatively that confinement of more than one chain has a strong effect on the molecule conformation, positioning and dynamics. In the case of single molecule (λ-DNA) confinement, the molecule remains preferentially in the cavity center; in the case of confinement of two molecules of identical size (two λ-DNA's) the molecules segregate and the center of the molecule coils are displaced from the cavity center. The two molecules appear to undergo a Brownian 'rotation' about the cavity center. In contrast to the two λ-DNA molecules, which show clear segregation, the plasmid appears to mix partially with the λ-DNA coil, with some frames indicating overlap of the plasmid and λ-DNA (figure 4.1(d)).

4.2.2 DNA Position Analysis

In order to quantify the above observations, image analysis is used to track the center-positions of the cavity confined molecules. The center-position of λ-DNA is obtained by performing a weighted average of position coordinates over the single-molecule fluorescence distribution in the cavity

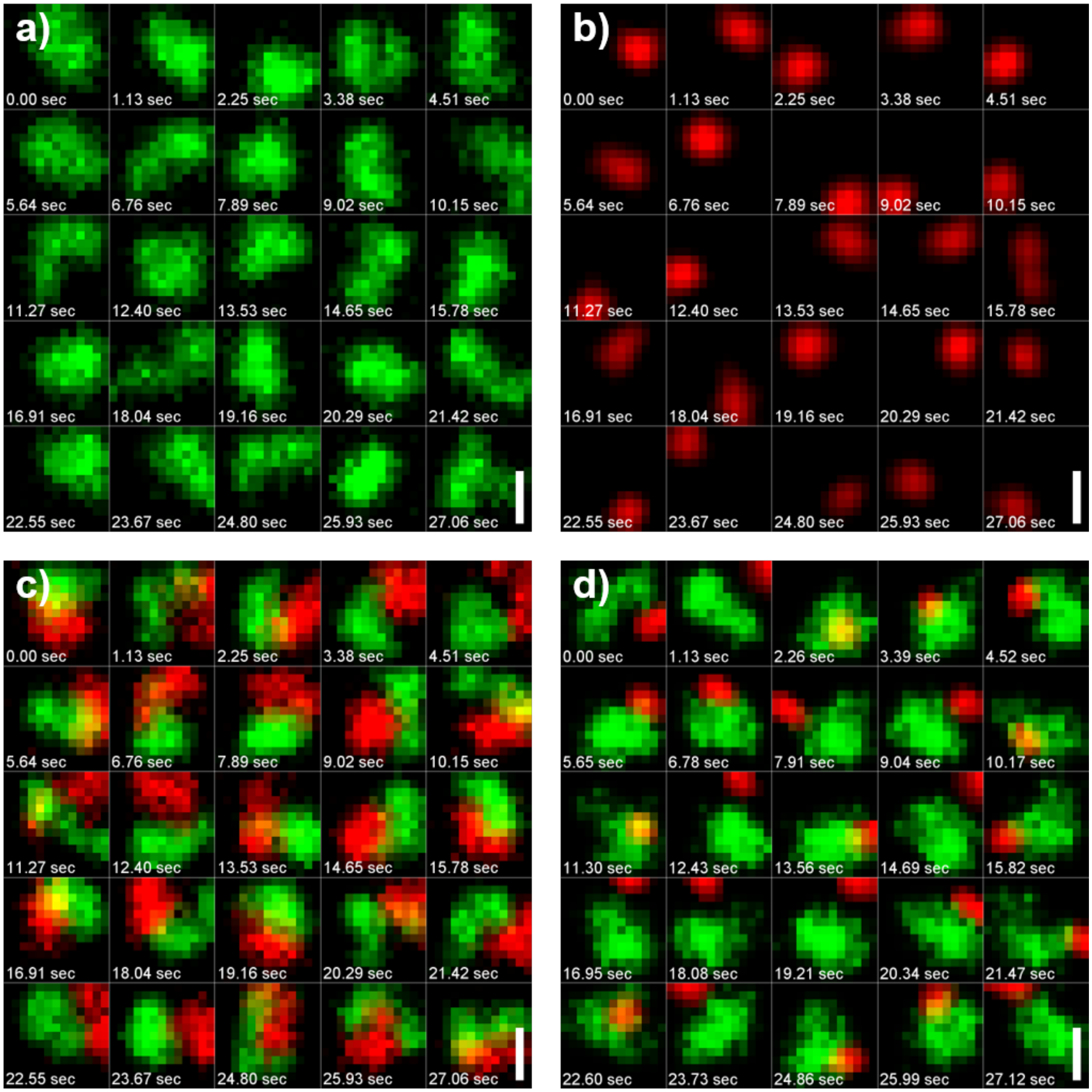

Figure 4.1: Fluorescence videomicroscopy frames of cavity confined DNA for cavities with lateral dimension of 2×2 µm^2. (a) Single λ-DNA trapped in a cavity. (b) Single plasmid trapped in a cavity (c) Two differentially stained λ-DNA molecules in a nanocavity. (d) A λ-DNA (green) and plasmid molecule (red) confined in a cavity. The green color indicates DNA stained with YOYO-1 while the red color indicates DNA stained with YOYO-3. Scale bar is 1 µm.

[12]:

$$\mathbf{r}_{CM}\left(t\right)=\frac{\int\mathbf{r}\cdot I\left(\mathbf{r},t\right)\mathrm{d}^{2}\,\mathbf{r}}{\int I\left(\mathbf{r},t\right)\mathrm{d}^{2}\,\mathbf{r}}. \tag{4.1}$$

The quantity $\mathbf{r}(t)$ is the position vector; the integral is taken over a ROI that corresponds to the cavity. The quantity $I(\mathbf{r},t)$ represents the intensity at position $\mathbf{r}$. To reduce the influence of background fluctuations on the position detection, we apply a Gaussian filter to the image prior to using Eq. 4.1. The plasmid, due to its circular supercoiled topology and smaller size [24, 35], has a more compact fluorescence distribution that corresponds to a diffraction-limited spot. We find that the plasmid center position can be efficiently tracked using the ImageJ Mosaic Particle Tracking plugin.

Figure 4.2(a) shows the distribution of molecule center-positions for a single λ-DNA molecule trapped in a cavity. As the λ DNA coil and cavity have similar dimensions, chain-wall interactions are quite strong and the λ-DNA is excluded from the cavity corners and periphery, giving rise to a center-position distribution tightly localized in the cavity middle. Figure 4.3(a) shows the position distribution for a single plasmid. As the plasmid has a much smaller gyration radius than the λ-DNA, the excluded region is smaller, and the plasmid can explore a greater portion of the cavity. In fact, we observe that the distribution is spatially uniform and follows the square cavity shape.

Figure 4.2(b) shows the position distribution of two λ-DNA molecules. When the second chain is present, due to excluded volume interactions between the coils, the center-position of the chains are forced to explore a greater portion of the cavity, creating a broader position distribution (see Fig. 4.2(c)). In addition, we find that the center position distribution for the YOYO-3 labeled chain is slightly more concentrated in the cavity center than the distribution for the YOYO-1 labeled chain (see Fig. 4.2(d)). This effect might arise from how the different stains alter the chain contour, stiffness and self-interactions. YOYO-1, for example, increases the contour length of DNA [29] and there are likely differences in intercalated length between the two stains. A molecule confined in a cavity will have its coil sized fixed by the cavity confinement, but a longer contour length will decrease the chain's entropic elasticity. Possibly, when the stains alter the contour length differentially, the slightly longer and more easily deformed chain is pushed to the cavity periphery as the chain closer to the periphery is required to deform more to adopt a greater circumferential extent and conform to the square cavity geometry.

Figure 4.3(b) shows the position distribution of λ-DNA and the plasmid when they are trapped together. We observe that the position distribution of the plasmid DNA is not altered by the presence of λ-DNA (Figure 4.3(c)), but that the position distribution of λ-DNA is less concentrated in the cavity center (Figure 4.3(d)). The plasmid, with its supercoiled circular topology, will have a compact anistropic structure and act–very crudely speaking–like an elongated pancake [24, 35]. This structure, once aligned with the cavity surfaces, might penetrate the λ-DNA structure relatively easily by passing through the depletion region of lowered DNA concentration near the cavity walls [46]. This effect, which is consistent with Fig. 4.1(d), would then explain why the 2D plasmid position distribution is not altered by the λ-DNA. We argue that the shifting of the λ-DNA position distribution might be explained by a depletion interaction induced by the plasmid [19]; by getting closer to the cavity edges, the λ-DNA frees up more volume for the plasmid conferring greater translational entropy.

4.2.3 DNA diffusion analysis for single chain trapping

The dynamics of a single DNA molecule confined within a cavity can be modeled as the free Brownian diffusion of a particle within an infinite square well potential [30]. The molecule's mean-square displacement along x given by:

$$MSD(\delta t) = \frac{1}{T}\int_0^T \left[x(t+\delta t) - x(t)\right]^2 dt \tag{4.2}$$

Since our device is symmetric in the x and y directions, with the coordinate system aligned with the cavity dimensions, the mean-square displacement is the same along the x and y axis and we average results obtained for x and y. The mean-square displacement can be obtained by solving the diffusion equation for a particle in a square box, leading to:

$$MSD(\delta t) = \frac{L^2}{6} - \frac{16L^2}{\pi^4}\sum_{n=1,3,5\cdots}^{\infty}\frac{1}{n^4}\exp\left[-D\left(\frac{n\pi}{L}\right)^2\delta t\right] \tag{4.3}$$

where L is the box width [30]. As the molecules have a finite size, a zone of excluded-volume will exist about the cavity boundary and the L values extracted will be smaller than the true lateral cavity dimensions. We show the experimental MSD with theoretical fit according to Eq. 4.3 in Fig. 4.4. Both the diffusion constant D and box width L are fitted.

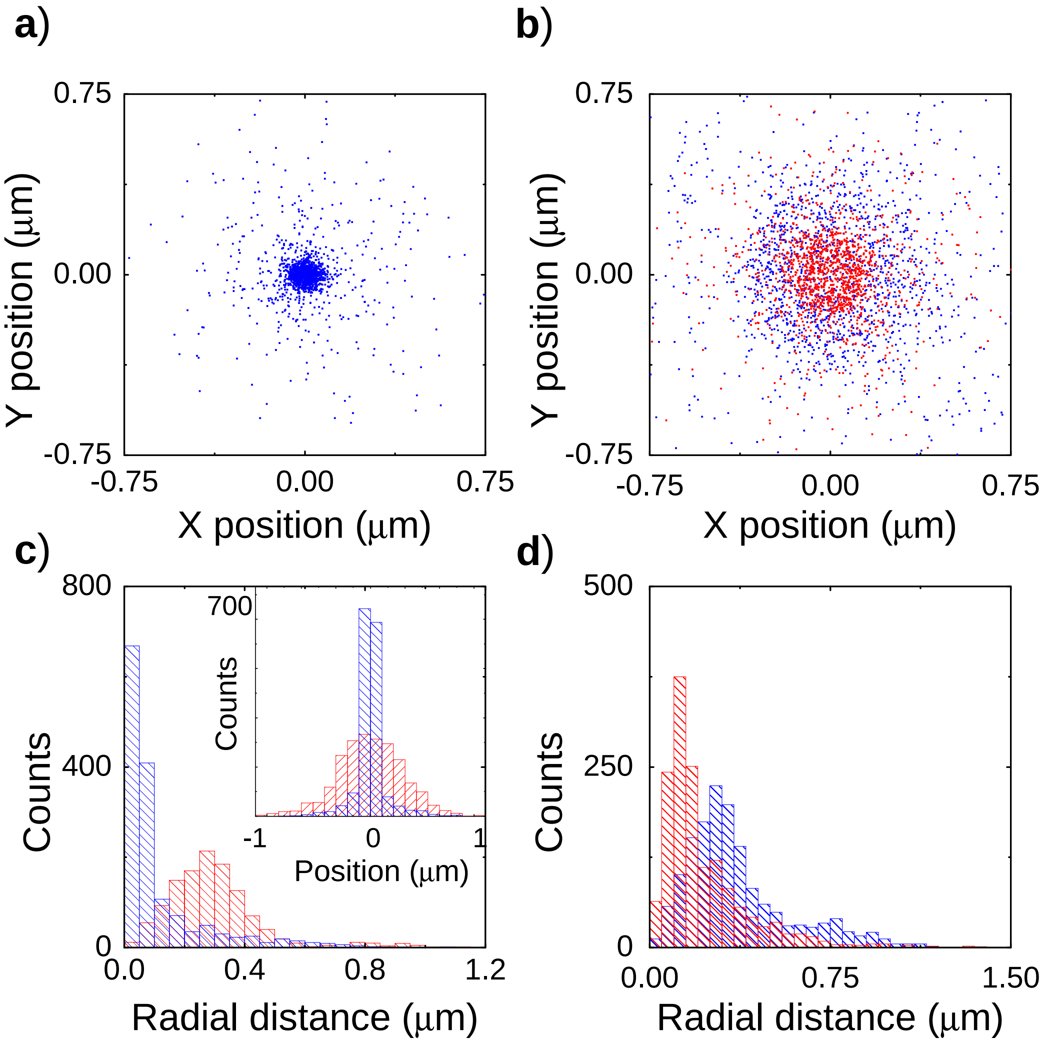

Figure 4.2: Center position analysis for λ-DNA. (a) Position distribution for a single λ-DNA trapped in the cavity. (b) Position distribution for two λ-DNA molecules in the cavity. Blue squares indicate YOYO-1 stained chain; red squares indicate YOYO-3 stained chain. (c) Radial distance histogram of λ-DNA chain. Blue shaded columns indicate distribution of single λ-DNA trapped in cavity. Red shaded columns indicate distribution of λ-DNA in cavity while the second λ-DNA is present. The inset shows for the same quantities the horizontal projection of the distribution along the cavity width. (d) Histogram of radial distance for λ-DNA in presence of second λ-DNA. Red shaded columns indicate YOYO-3 stained chains; blue shaded columns indicate YOYO-1 stained chain.

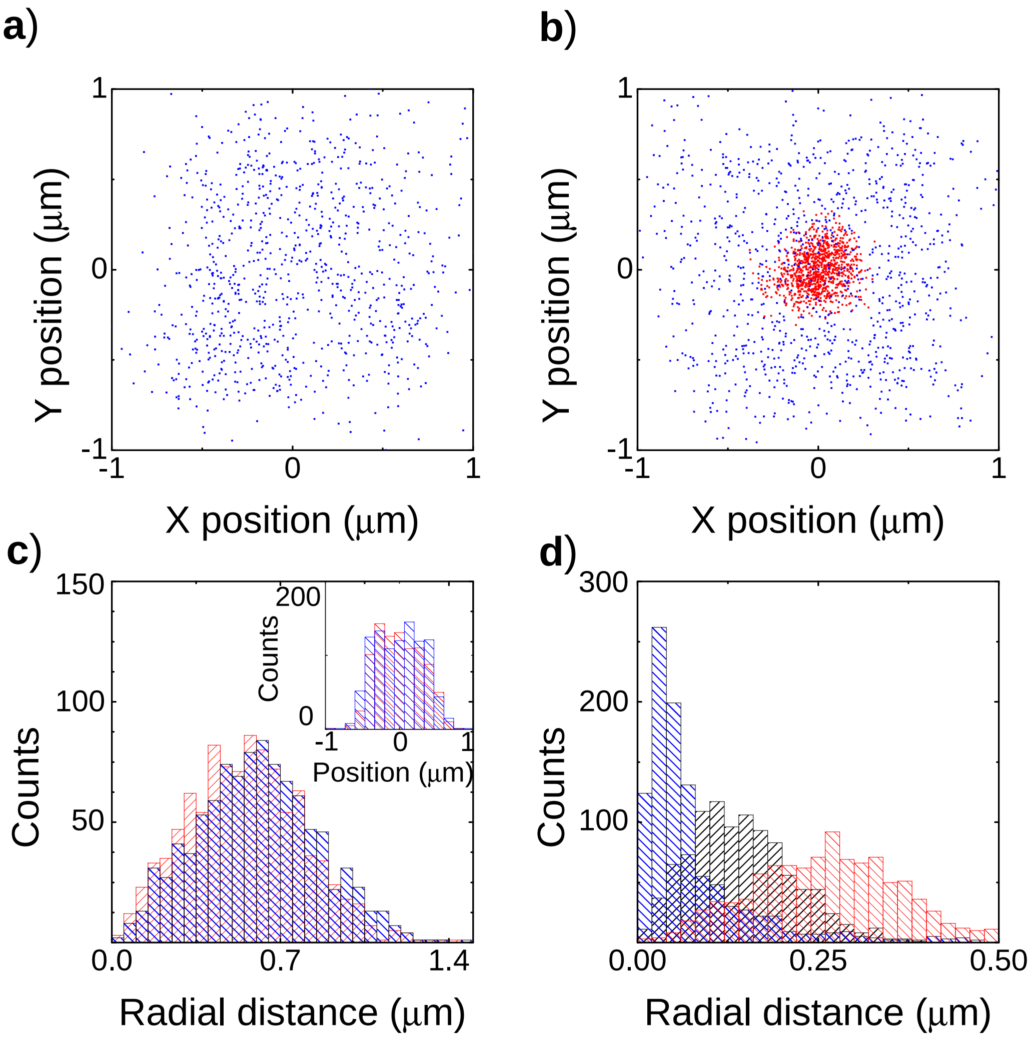

Figure 4.3: Center position analysis for plasmid DNA. (a) Position distribution for a single plasmid trapped in the cavity. (b) Position distribution for a plasmid trapped with λ-DNA in the cavity. Blue squares show plasmid positions; red squares show λ-DNA positions. (c) Radial position distribution of plasmid. The blue shaded columns show the distribution for single plasmid; red columns show the plasmid distribution when a λ-DNA is also present. The inset shows for the same quantities the horizontal projection of the distribution along the cavity width. (d) Histogram of radial distance of λ-DNA. The blue shaded columns indicate the distance distribution for single λ-DNA trapping. Black shaded columns indicate the distribution of λ when the plasmid is also present. The red shaded columns indicate the distribution when two λ-DNA molecules are trapped.

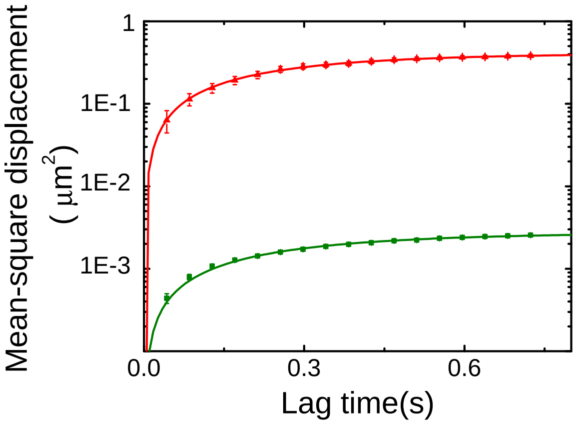

Figure 4.4: Mean-square displacement for single λ-DNA trapping (green triangles) and single plasmid trapping (red squares). The solid curve is the fitted diffusion model.

The DNA diffusion constants obtained are $D_\lambda = 0.055 \pm 0.003\mu\text{m}\,\text{s}^{-2}$ (for λ-DNA) and $D_\text{p} = 0.68 \pm 0.02\mu\text{m}\,\text{s}^{-2}$ (for plasmid). In bulk, $D_{\text{bulk},\lambda} = 0.47 \pm 0.03\mu\text{m}\,\text{s}^{-2}$ [50] and in a 200 nm nanoslit $D_{\text{slit},\lambda} = 0.1\mu\text{m}^2\,\text{s}^{-1}$ [51, 6], so that cavity confinement creates a two-fold reduction with respect to the slit and a factor of ten with respect to bulk. For a 6.5 kpb plasmid the bulk diffusion constant $D_{\text{bulk, p}} = 2.89\mu\text{m}^2\,\text{s}^{-1}$ [54]; cavity confinement thus leads to a 4-fold reduction with respect to bulk. The extracted confinement dimension L of λ-DNA is $0.13 \pm 0.002\mu\text{m}$ while the confinement dimension of the plasmid is $1.57 \pm 0.01\mu\text{m}$. The radius of gyration for λ-DNA confined in a 200 nm slit is: $r_{g,\lambda} = 0.91\mu\text{m}$.[34]. Using $2r_g$ as an estimate of the molecule coil extent, we estimate that the confinement dimension $L \approx d - 2r_g$ where $d = 2\mu\text{m}$ is the cavity width . The resulting value $L_\lambda \approx 0.2\mu\text{m}$ is quite comparable to our measurement. To estimate the extent of the plasmid, we use measurements for the ColE$_1$ plasmid, which is of comparable size (6.65 kbp). Voordouw*et al*[54] report that for ColE$_1$ light scattering measurments give $r_g^\text{p} = 104\text{nm}$ so that $L_\text{p} \approx 1.79\mu\text{m}$. This is the right magnitude but larger than then the L_p value we measure, a difference which might arise from plasmid anisotropy and our lower ionic strength.

4.2.4 Position auto-correlation calculation

We investigate the position auto-correlation of the λ-DNA and plasmid molecule for both single molecule and two-molecule trapping (see Fig. 4.5). The position auto-correlation function is defined as:

$$C_{auto}\left(\delta t\right) = \left\langle x\left(t+\delta t\right) x\left(t\right)\right\rangle_t \tag{4.4}$$

where x represents position along either the $x-$ or $y-$ direction with the origin located at the cavity center. The angle bracket indicates a time-average, corresponding to averaging over the entire video length; δt is the correlation lag time. Considering the square symmetry of the cavity, we average the position auto-correlations for the $x-$ and $y-$ directions.

Figure 4.5(a,b) shows the autocorrelation functions for single and two-particle trapping; these are well-descibed by a single exponential function. We define the decorrelation time as the time needed for the correlation function to decay to e^{-1} of its maximum value. The decorrelation time for λ-DNA trapped in a cavity, if no other molecules are present, is 0.25 ± 0.01s; the decorrelation time for λ-DNA, trapped in the presence of a plasmid, is 0.29 ± 0.01s and the decorrelation time for λ DNA trapped in the presence of a second λ-DNA molecule is 2.00 ± 0.1s. The decorrelation time clearly increases with the presence of additional molecules, and in the case of λ-DNA increases by almost an order of magnitude. The decorrelation time for a plasmid, if no other molecule is trapped, is 0.31 ± 0.01s; in the presence of a λ-DNA molecule the decorrelation time is 0.39 ± 0.01s. Qualitatively, we believe that the increasing decorrelation times for two-molecule trapping arise as the second molecule transiently confines the first molecule creating a caging effect. Caging leads to a lower effective diffusion constant for the molecules that then increases the overall decorrelation time.

We also investigate the position cross-correlation between the YOYO-1 stained λ-DNA chain and the YOYO-3 stained λ-DNA chain (Figure 4.5 (c)). The cross-correlation is defined as

$$C_{cross}\left(\delta t\right) = \left\langle x_{\text{yoyo-1}}\left(t+\delta t\right) x_{\text{yoyo-3}}\left(t\right)\right\rangle_t \tag{4.5}$$

where $x_{\text{yoyo-1}}$ and $x_{\text{yoyo-3}}$ represent respectively the position of the YOYO-1 stained chain and the YOYO-3 stained chain at time t along the $x-$ or $y-$ direction. Again, we average the cross-correlation function over x and y directions. The cross-correlation function is negative, indicating

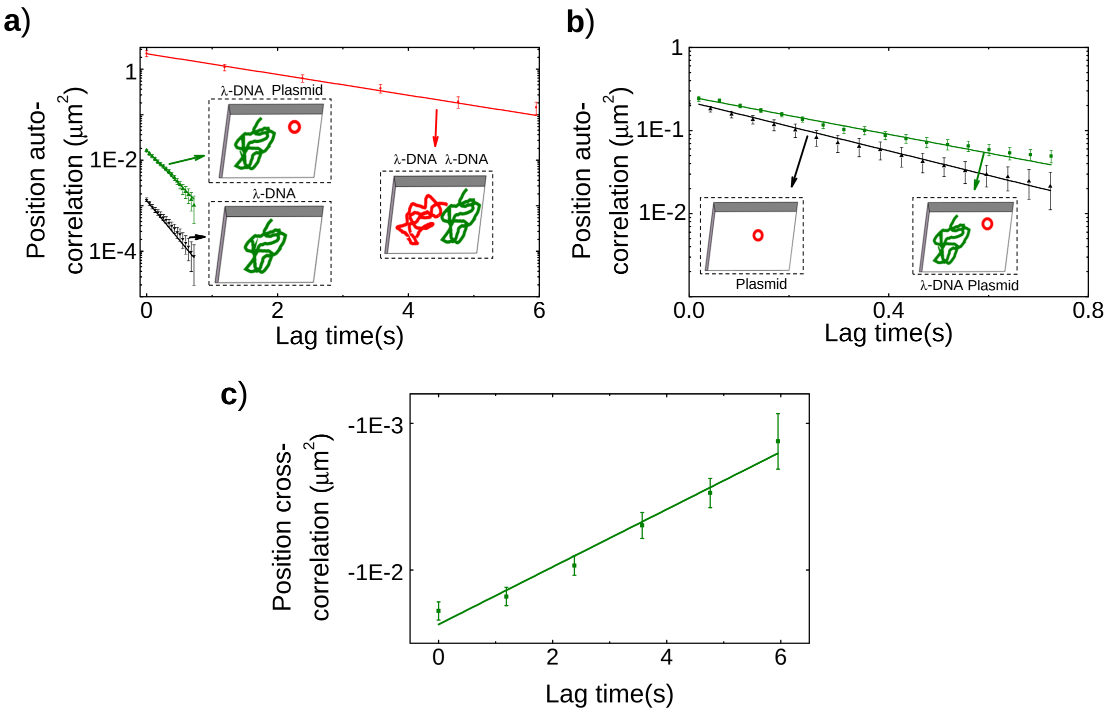

Figure 4.5: Position auto-correlation as a function of lag time on a log-linear scale with an exponential fit. (a) Position auto-correlation function for λ-DNA. Red squares indicate the correlation function measured for a λ-DNA molecule trapped in a cavity when there is a second λ-DNA molecule trapped in the same cavity. Green upper triangles indicate the correlation function obtained for λ-DNA when there is a plasmid molecule also trapped in the cavity with the λ-DNA. Black lower triangles indicate the correlation function measured for a λ-DNA molecule trapped in a cavity when there are no other molecules present. (b) Auto-correlation function for plasmid DNA. Green squares indicate the position correlation function of the plasmid in the presence of a λ-DNA molecule trapped in the same cavity as the plasmid. Black upper triangles indicate the position autocorrelation function for the plasmid with no other molecules present. (c) Position cross correlation for trapping of a YOYO-1 stained λ-DNA and a YOYO-3 stained λ-DNA. Exponential fits are shown as bold curves in the same color as the data points. Error bars correspond to standard error arising from measurements over an ensemble of 10 different molecules undergoing equivalent dynamics.

anti-correlation arising from the strong segregation between the molecules. The decorrelation time of the cross-correlation is 2.8 ± 0.3s, comparable in order of magnitude to the autocorrelation decay time; we hypothesize it is longer than the autocorrelation decay time as the cross-correlation function decorrelates over the time-scale required for *both* chains to loose their initial joint conformation.

4.2.5 Intensity cross-correlation function

As a final measure of the two-chain dynamics, for the case of two λ-DNA molecules we investigate the cross-correlation of the intensity across the cavity. In particular, we compute the intensity cross-correlation function $\langle \delta I_{\text{yoyo-1}}(x, y, t)\delta I_{\text{yoyo-3}}(x, y, t+\delta)\rangle$, where δI gives the fluctuation away from the average intensity at position (x, y) inside the cavity. Figure 4.6(a-c) shows the intensity cross-correlation for three different times. We find that there is a strong anti-correlated annular well for short times, consistent with the organized rotation of the segregated conformations observed in Fig. 4.1c. The 'hill' of slightly reduced anti-correlation in the cavity center corresponds to configurations where the molecules have drifted to the center and partially mixed, leading to a slight breaking of the organized rotational dynamics and a reduction in anti-correlation. We also compute the cross-correlation function averaged over the entire cavity region (Fig. 4.6(d)). The averaged cross-correlation is described well by a single exponential decay and has a decorrelation time of 4.2 ± 0.4s. This value is comparable in magnitude but slightly larger than the position cross-correlation decay time. We speculate that the position cross-correlation decay time is lower because of the greater confinement of the molecule center positions relative to a particular individual segment or portion of the molecule. The greater confinement of the molecule centers implies that the center positions have to migrate over a smaller distance to swap positions compared with the distance an individual segment needs to traverse to return to a particular location of the cavity.

4.3 Conclusions

The molecular organization and dynamics are strongly affected by whether more than one molecule is captured. Two confined λ-DNA molecules with a coil extent on order of the cavity width exist in a highly partitioned state and appear to undergo a Brownian rotation about the cavity center.

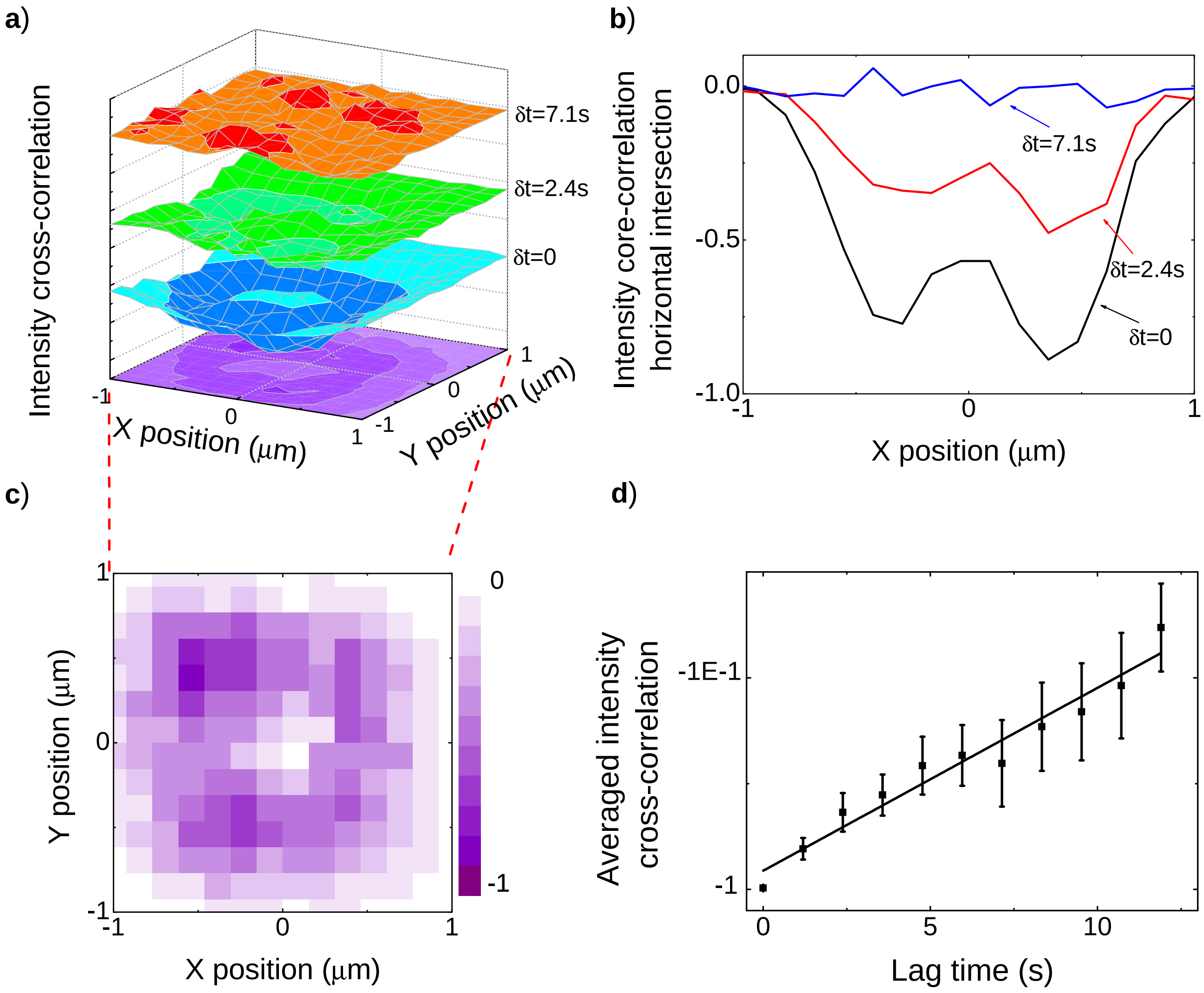

Figure 4.6: Intensity Cross-Correlation Function. (a) Surface plot for normalized intensity cross-correlation for different lag times. Orange surface represents cross-correlation function at $\delta t = 7.1s$, green surface represents cross-correlation function at $\delta t = 2.4s$ and blue surface represents cross-correlation function at $\delta t = 0$. (b) Intensity cross-correlation function from (a) taken along a slice along the x-axis for $y = 0$. (c) Intensity cross-correlation for $\delta t = 0$. (d) Intensity cross-correlation function averaged across cavity verses lag time. The correlation function is fitted with an exponential function that is shown as a black solid curve.

Even the presence of a small plasmid molecule can alter the λ-DNA state, tending to pull it away from the cavity center. Confinement of more than one molecule has additional non-trivial effects on dynamics, tending to increase overall relaxation times for confined molecular diffusion.

Chapter 5

Conclusion

We designed and fabricated a pneumatically-actuated membrane device to dynamically confine multiple DNA chains into nanoscale pit features. The active trapping mechanism is a nanoscale nitride lid that deflects under pneumatic pressure. Significant fabrication challenges were overcome to produce working devices with an acceptable yield. To illustrate the power of this technology, single λ-DNA and plasmid DNA were studied in nanoscale pits. In addition, two λ-DNA and λ-DNA/plasmid DNA systems were studied. While we do not see evidence of segregation of plasmids and λ-DNA, possibly this effect requires higher chain concentration and/or presence of chain condensing agents, like molecular crowders [27, 16], which we plan to explore in future experiments. Our observation, however, that the presence of a single small compact molecule can impact the behaviour of a larger coil in confinement is intriguing. For example, might we detect differences between linearized and circular form plasmids? How does this effect scale with plasmid size and plasmid number? In addition, we show subtle differences due to chemical stains (e.g. YOYO-1 versus YOYO-3) can be detected via two-molecule measurements of the chain position distributions. Possibly, this effect could extend to other types of molecular labeling or protein-interactions. Overall, our results suggest that measurements of the physical interactions of multiple confined macromolecules might convey information beyond that of a purely single molecule experiment. From a theoretical point of view, Monte Carlo and Brownian dynamics simulations of multiple chain confinement might clarify the underlying mechanisms responsible for our observations. Experiments performed with precisely defined nanofluidic systems consisting of a known number of interacting polymers and colloids might help validate/calibrate existing simulation approaches.

Using very similar devices we can explore how the properties of the organized multiple molecule states might vary as a function of the molecule size ratio, molecule number and cavity geometry. Distinct dynamical regimes might exist for two, three or multiple molecule states as a function of cavity dimensions and size ratio. These experiments are an easy extension of our current work. Varying device trapping geometry is as simple as modifying an e-beam mask and performing our fabrication process again. Varying the molecules and stains is also easy.

With our current iteration of devices, we have not calibrated the pneumatic pressure sufficiently to confine molecules without fully sealing the trapping cavities. After implementing this, a series of experiments can be performed by varying the gap above trapping features. Escape from our traps will then be possible upon application of a sufficient driving force to overcome the free energy differential. Our system would then enable exploration of how the presence of multiple chains affects escape kinetics. In addition, a similar experiment can be performed to investigate how the vertical dimension effects molecule partitioning. In particular, does chain mixing occur as bulk conditions are approached?

A challenge with active confinement devices is always loading efficiency. The CLiC technology used electrophoresis to pull the DNA into the confined slit as the lid was depressed [1]. We plan to integrate our devices with nanopores centered over each trapping feature. By applying an alternating current, DNA will be trapped at the pores by the dielectrophoretic force. The membrane can then be depressed and the molecules released into the trapping features. This is particularly interesting when trying to highly confine DNA in small cavities. In biological systems, viral capsids contain highly confined DNA chains which are ejected forcefully into their target host cells. Replicating that magnitude of confinement can help us understand why we see knotting in viral DNA, how that DNA is ejected from its shell and how it interacts in the confined volume of the cell with other chains [3].

Future experiments will also include cellular work with E. coli. Devices will be fabricated to study E. coli replication when ‘squeezed’ under the pneumatic lid. Other experiments could allow two-color staining and mixing of E. coli genomes, all within a single microfluidic device. Multiple membranes can be used to trap, lyse and stain in multiple regions giving unprecidented control over these cellular experiments.

In addition to two-molecule confinement experiments, preliminary work has been done to develop a new imaging method using fluorescent buffer. This promises to be a potentially powerful technique with applications in surface characterization as well as macromolecular study. Once the fluorescent intensity of buffer dyes has been calibrated with height, this technique can characterize surface roughness inside sealed nanofluidic devices. New dyes will be tested and the fabrication will be modified to produce very smooth substrates. In addition, we plan to study mapping of macromolecules compressed between the substrate and the nitride lid. This technique would be a fluorescent equivalent to cryo-SEM. It could allow the characterization of unstained macromolecules, proteins and other biological complexes.

Each of the previous actuated micro/nanofluidic devices developed since 2000 have exposed more about the nature of biological polymers and these confined environments. We hope to push similar progress in the field with the developement of this new technology, even more so because of its ease of operation and powerful customizability. With future work, the device can be extended further. An isotropic etch profile will allow full channel sealing similar to that of the Quake valve and a PDMS interfacial layer will increase the density of individually actuatable membranes which will result in a highly integrated and multiplexable nanofluidic platform.

References

[1] Mohammed Jalal Ahamed et al. “Continuous Confinement Fluidics: Getting Lots of Molecules into Small Spaces with High Fidelity”. In: *Macromolecules* 49.7 (Mar. 2016), pp. 2853–2859. DOI: `10.1021/acs.macromol.5b02617`.

[2] Ismail Emre Araci and Stephen R. Quake. “Microfluidic very large scale integration (mVLSI) with integrated micromechanical valves”. In: *Lab on a Chip* 12.16 (2012), p. 2803. DOI: `10.1039/c2lc40258k`.

[3] J. Arsuaga et al. “Knotting probability of DNA molecules confined in restricted volumes: DNA knotting in phage capsids”. In: *Proceedings of the National Academy of Sciences* 99.8 (Apr. 2002), pp. 5373–5377. DOI: `10.1073/pnas.032095099`.

[4] Anthony K. Au et al. “3D-Printed Microfluidics”. In: *Angewandte Chemie International Edition* 55.12 (Feb. 2016), pp. 3862–3881. DOI: `10.1002/anie.201504382`.

[5] *AZ® 9200 Photoresist: high-resolution thick resist.* URL: `https://www.microchemicals.com/micro/az_9200.pdf` (visited on 07/28/2018).

[6] Anthony Balducci et al. “Double-Stranded DNA Diffusion in Slitlike Nanochannels”. In: *Macromolecules* 39.18 (Sept. 2006), pp. 6273–6281. DOI: `10.1021/ma061047t`.

[7] Daniel J. Berard et al. “Convex lens-induced nanoscale templating”. In: *Proceedings of the National Academy of Sciences* 111.37 (Aug. 2014), pp. 13295–13300. DOI: `10.1073/pnas.1321089111`.

[8] Daniel J. Berard et al. “Formatting and ligating biopolymers using adjustable nanoconfinement”. In: *Applied Physics Letters* 109.3 (July 2016), p. 033702. DOI: `10.1063/1.4958196`.

[9] Daniel Berard et al. “Precision platform for convex lens-induced confinement microscopy”. In: *Review of Scientific Instruments* 84.10 (Oct. 2013), p. 103704. DOI: `10.1063/1.4822276`.

[10] S. S. Bhavikatti. *Theory of Plates and Shells*. New Age International, Dec. 11, 2011. ISBN: 9788122434927.

[11] J T Del Bonis-O’Donnell, W Reisner, and D Stein. “Pressure-driven DNA transport across an artificial nanotopography”. In: *New Journal of Physics* 11.7 (July 2009), p. 075032. DOI: `10.1088/1367-2630/11/7/075032`.

[12] Douwe Jan Bonthuis et al. “Conformation and Dynamics of DNA Confined in Slitlike Nanofluidic Channels”. In: *Physical Review Letters* 101.10 (Sept. 2008). DOI: `10.1103/physrevlett.101.108303`.

[13] *BOROFLOAT® 33 – General Information*. URL: `https://www.us.schott.com/d/borofloat/fac81f3e-5e04-4fc5-a039-dced3533c8e9/1.2/borofloat33_gen_usa_web.pdf` (visited on 07/01/2018).

[14] *BOROFLOAT® The world's first floated borosilicate glass – Made in Germany with IQ*. URL: `https://www.us.schott.com/d/borofloat/23052e97-2e03-43e9-996b-267978964942/1.2/borofloat33_broschure_us_web_ds.pdf` (visited on 07/01/2018).

[15] *Brewer Science® ProTEK® PSB. Photosensitive Alkaline-Resistant Coating*. 2009. URL: `https://www.mri.psu.edu/sites/default/files/file_attach/BrewerScience_ProTek.pdf` (visited on 08/03/2018).

[16] Yuhao Chen et al. “Polymer segregation under confinement: Influences of macromolecular crowding and the interaction between the polymer and crowders”. In: *The Journal of Chemical Physics* 143.13 (Oct. 2015), p. 134904. DOI: `10.1063/1.4932370`.

[17] Hou-Pu Chou, Marc A. Unger, and Stephen R. Quake. “A Microfabricated Rotary Pump”. In: *Biomedical Microdevices* 3.4 (2001), pp. 323–330. DOI: `10.1023/a:1012412916446`.

[18] E. Paul DeGarmo. *Materials and Processes in Manufacturing*. 9th ed. Wiley, 2003.

[19] Masao Doi. *Soft Matter Physics*. Oxford University Press, June 2013. DOI: `10.1093/acprof:oso/9780199652952.001.0001`.

[20] *DSM Somos® Watershed® XC 11122*. URL: `https://www.dsm.com/content/dam/dsm/somos/en_US/documents/Brand-Status-Sell-Sheets/English-Letter/Somos%20WaterShed%20XC%2011122%20SS-PDS%20Letter.pdf` (visited on 07/31/2018).

[21] Sami Franssila. *Introduction to Microfabrication*. John Wiley and Sons Ltd, Sept. 17, 2010. 534 pp. ISBN: 0470749830. URL: `https://www.ebook.de/de/product/10358471/sami_franssila_introduction_to_microfabrication.html`.

[22] Abhijat Goyal, Vincent Hood, and Srinivas Tadigadapa. "High speed anisotropic etching of Pyrex® for microsystems applications". In: *Journal of Non-Crystalline Solids* 352.6-7 (May 2006), pp. 657–663. DOI: `10.1016/j.jnoncrysol.2005.11.063`.

[23] Gil Henkin et al. "Manipulating and Visualizing Molecular Interactions in Customized Nanoscale Spaces". In: *Analytical Chemistry* 88.22 (Oct. 2016), pp. 11100–11107. DOI: `10.1021/acs.analchem.6b03149`.

[24] N. Patrick Higgins and Alexander V. Vologodskii. "Topological Behavior of Plasmid DNA". In: *Plasmids: Biology and Impact in Biotechnology and Discovery*. American Society of Microbiology, 2015, pp. 105–131. DOI: `10.1128/microbiolspec.plas-0036-2014`.

[25] Jong Wook Hong et al. "A nanoliter-scale nucleic acid processor with parallel architecture". In: *Nature Biotechnology* 22.4 (Mar. 2004), pp. 435–439. DOI: `10.1038/nbt951`.

[26] Daniel Kim et al. "Giant Acceleration of DNA Diffusion in an Array of Entropic Barriers". In: *Physical Review Letters* 118.4 (Jan. 2017). DOI: `10.1103/physrevlett.118.048002`.

[27] Juin Kim et al. "A polymer in a crowded and confined space: effects of crowder size and poly-dispersity". In: *Soft Matter* 11.10 (2015), pp. 1877–1888. DOI: `10.1039/c4sm02198c`.

[28] Alexander R. Klotz et al. "Measuring the Confinement Free Energy and Effective Width of Single Polymer Chains via Single-Molecule Tetris". In: *Macromolecules* 48.14 (July 2015), pp. 5028–5033. DOI: `10.1021/acs.macromol.5b00977`.

[29] Binu Kundukad, Jie Yan, and Patrick S. Doyle. "Effect of YOYO-1 on the mechanical properties of DNA". In: *Soft Matter* 10.48 (2014), pp. 9721–9728. DOI: `10.1039/c4sm02025a`.

[30] A. Kusumi, Y. Sako, and M. Yamamoto. “Confined lateral diffusion of membrane receptors as studied by single particle tracking (nanovid microscopy). Effects of calcium-induced differentiation in cultured epithelial cells”. In: *Biophysical Journal* 65.5 (Nov. 1993), pp. 2021–2040. DOI: `10.1016/s0006-3495(93)81253-0`.

[31] Yuan-Sheng Lee, Nirveek Bhattacharjee, and Albert Folch. “3D-printed Quake-style microvalves and micropumps”. In: *Lab on a Chip* 18.8 (2018), pp. 1207–1214. DOI: `10.1039/c8lc00001h`.

[32] Sabrina R. Leslie, Alexander P. Fields, and Adam E. Cohen. “Convex Lens-Induced Confinement for Imaging Single Molecules”. In: *Analytical Chemistry* 82.14 (July 2010), pp. 6224–6229. DOI: `10.1021/ac101041s`.

[33] Xinghua Li, Takashi Abe, and Masayoshi Esashi. “Deep reactive ion etching of Pyrex glass using SF6 plasma”. In: *Sensors and Actuators A: Physical* 87.3 (Jan. 2001), pp. 139–145. DOI: `10.1016/s0924-4247(00)00482-9`.

[34] Po-Keng Lin et al. “Static conformation and dynamics of single DNA molecules confined in nanoslits”. In: *Physical Review E* 76.1 (July 2007). DOI: `10.1103/physreve.76.011806`.

[35] Y. L. Lyubchenko and L. S. Shlyakhtenko. “Visualization of supercoiled DNA with atomic force microscopy in situ”. In: *Proceedings of the National Academy of Sciences* 94.2 (Jan. 1997), pp. 496–501. DOI: `10.1073/pnas.94.2.496`.

[36] Sara Mahshid et al. “Development of a platform for single cell genomics using convex lens-induced confinement”. In: *Lab on a Chip* 15.14 (2015), pp. 3013–3020. DOI: `10.1039/c5lc00492f`.

[37] J.T. Mannion et al. “Conformational Analysis of Single DNA Molecules Undergoing Entropically Induced Motion in Nanochannels”. In: *Biophysical Journal* 90.12 (June 2006), pp. 4538–4545. DOI: `10.1529/biophysj.105.074732`.

[38] Pan Mao and Jongyoon Han. “Fabrication and characterization of 20 nm planar nanofluidic channels by glass–glass and glass–silicon bonding”. In: *Lab on a Chip* 5.8 (2005), p. 837. DOI: `10.1039/b502809d`.

[39] Morten Bo Mikkelsen et al. “Pressure-Driven DNA in Nanogroove Arrays: Complex Dynamics Leads to Length- and Topology-Dependent Separation”. In: *Nano Letters* 11.4 (Apr. 2011), pp. 1598–1602. DOI: `10.1021/nl1044764`.

[40] Samuel Million-Weaver and Manel Camps. “Mechanisms of plasmid segregation: Have multicopy plasmids been overlooked?” In: *Plasmid* 75 (Sept. 2014), pp. 27–36. DOI: `10.1016/j.plasmid.2014.07.002`.

[41] W. Reisner et al. “Single-molecule denaturation mapping of DNA in nanofluidic channels”. In: *Proceedings of the National Academy of Sciences* 107.30 (July 2010), pp. 13294–13299. DOI: `10.1073/pnas.1007081107`.

[42] Walter Reisner, Jonas N Pedersen, and Robert H Austin. “DNA confinement in nanochannels: physics and biological applications”. In: *Reports on Progress in Physics* 75.10 (Sept. 2012), p. 106601. DOI: `10.1088/0034-4885/75/10/106601`.

[43] Walter Reisner et al. “Statics and Dynamics of Single DNA Molecules Confined in Nanochannels”. In: *Physical Review Letters* 94.19 (May 2005). DOI: `10.1103/physrevlett.94.196101`.

[44] R. Reyes-Lamothe et al. “High-copy bacterial plasmids diffuse in the nucleoid-free space, replicate stochastically and are randomly partitioned at cell division”. In: *Nucleic Acids Research* 42.2 (Oct. 2013), pp. 1042–1051. DOI: `10.1093/nar/gkt918`.

[45] Kenneth G. Romanchuk. “Fluorescein. Physicochemical factors affecting its fluorescence”. In: *Survey of Ophthalmology* 26.5 (Mar. 1982), pp. 269–283. DOI: `10.1016/0039-6257(82)90163-1`.

[46] Takahiro Sakaue. “Semiflexible Polymer Confined in Closed Spaces”. In: *Macromolecules* 40.14 (July 2007), pp. 5206–5211. DOI: `10.1021/ma070594r`.

[47] Julian Sheats et al. “Measurements of DNA barcode label separations in nanochannels from time-series data”. In: *Biomicrofluidics* 9.6 (Nov. 2015), p. 064119. DOI: `10.1063/1.4938732`.

[48] *Shipley Microposit® S1800® Series Photo Resists*. URL: `http://www.nanophys.kth.se/nanophys/facilities/nfl/resists/S1813/s1800seriesDataSheet.pdf` (visited on 07/28/2018).

[49] Min Ju Shon and Adam E. Cohen. “Mass Action at the Single-Molecule Level”. In: *Journal of the American Chemical Society* 134.35 (Aug. 2012), pp. 14618–14623. DOI: `10.1021/ja3062425`.

[50] Douglas E. Smith, Thomas T. Perkins, and Steven Chu. “Dynamical Scaling of DNA Diffusion Coefficients”. In: *Macromolecules* 29.4 (Jan. 1996), pp. 1372–1373. DOI: `10.1021/ma951455p`.

[51] Elizabeth A. Strychalski, Stephen L. Levy, and Harold G. Craighead. “Diffusion of DNA in Nanoslits”. In: *Macromolecules* 41.20 (Oct. 2008), pp. 7716–7721. DOI: `10.1021/ma801313w`.

[52] M. A. Unger. “Monolithic Microfabricated Valves and Pumps by Multilayer Soft Lithography”. In: *Science* 288.5463 (Apr. 2000), pp. 113–116. DOI: `10.1126/science.288.5463.113`.

[53] Christian L. Vestergaard et al. “Transition state theory demonstrated at the micron scale with out-of-equilibrium transport in a confined environment”. In: *Nature Communications* 7 (Jan. 2016), p. 10227. DOI: `10.1038/ncomms10227`.

[54] G. Voordouw et al. “Isolation and physical studies of the intact supercoiled”. In: *Biophysical Chemistry* 8.2 (May 1978), pp. 171–189. DOI: `10.1016/0301-4622(78)80008-8`.

[55] Yong Wang, Paul Penkul, and Joshua N. Milstein. “Quantitative Localization Microscopy Reveals a Novel Organization of a High-Copy Number Plasmid”. In: *Biophysical Journal* 111.3 (Aug. 2016), pp. 467–479. DOI: `10.1016/j.bpj.2016.06.033`.

[56] Xian-Ping Wu, Quin-Hai Wu, and Wen H. Ko. “A study on deep etching of silicon using ethylene-diamine-pyrocatechol-water”. In: *Sensors and Actuators* 9.4 (July 1986), pp. 333–343. DOI: `10.1016/0250-6874(86)80065-8`.

[57] Feiqiao Brian Yu et al. “Long-term microfluidic tracking of coccoid cyanobacterial cells reveals robust control of division timing”. In: *BMC Biology* 15.1 (Feb. 2017). DOI: `10.1186/s12915-016-0344-4`.

[58] *ZEONREX® Electronic Chemicals: ZEP520A*. URL: `http://www.nanophys.kth.se/nanophys/facilities/nfl/resists/zep520a-7-2.pdf` (visited on 08/01/2018).

[59] Chenchen Zhang, Gokhan Hatipoglu, and Srinivas Tadigadapa. “High-Speed Ultrasmooth Etching of Fused Silica Substrates in SF6, NF3, and H2O-Based Inductively Coupled Plasma Process”. In: *Journal of Microelectromechanical Systems* 24.4 (Aug. 2015), pp. 922–930. DOI: `10.1109/jmems.2014.2359292`.